Earth-Science Reviews 260 (2025) 104987

Contents lists available at ScienceDirect

Earth-Science Reviews

journal homepage: www.elsevier.com/locate/earscirev

Reassessing metamorphic core complexes in the North American Cordillera

Andrew V. Zuza [a,b,*], Gilby Jepson [c], Wenrong Cao [b,d]

[a] Nevada Bureau of Mines and Geology, University of Nevada, Reno, NV 89557, United States
[b] Nevada Geosciences, University of Nevada, Reno, NV 89557, United States
[c] School of Geosciences, University of Oklahoma, Norman, OK 73019, United States
[d] Department of Geological Sciences and Engineering, University of Nevada, Reno, NV 89557, United States

ARTICLE INFO

Keywords:
Metamorphic core complex
North American Cordillera
Gneiss dome
Rayleigh-Taylor instability
Crustal flow
Slab rollback
Regional extension

ABSTRACT

Continental metamorphic core complexes (MCCs) are widely distributed on Earth, primarily exposed at convergent plate margins. These structural systems involve the exhumation of metamorphosed, commonly migmatitic, middle-lower crust rocks along high-strain mylonitic shear zones to the brittle upper crust. However, the extent to which the brittle faults, ductile shear zones, and syn-kinematic igneous rocks are genetically and kinematically related within MCCs remains inadequately understood. To address this, we synthesize structural, geochronological, thermochronological, sedimentological, and petrological observations from MCCs distributed across the strike-length of the North American Cordillera. We show that Paleogene ductile MCC exhumation tracked via medium-to-high temperature thermochronology (i.e., biotite and muscovite $^{40}Ar/^{39}Ar$ dates) and cross-cutting relationships youngs toward the central Cordillera latitudes (~37°N), whereas predominately Miocene brittle faulting and syn-kinematic basin formation youngs northward from the south. Ductile MCC exhumation age trends parallel magmatic sweeps associated with rollback of the Farallon slab, whereas brittle extensional faulting trends correlate with the northward migration of the Mendocino triple junction and the initiation of Basin and Range extension. In light of these observations, we argue that MCCs in the North American Cordillera were not the result of a single phase of extension, but rather reflect two decoupled stages including an early phase of buoyant diapirism followed by a later phase of lithospheric extension. The diapirism ocurred as a Rayleigh-Taylor instability due to crustal melting driven by asthenospheric influx during slab rollback and coupled magmatism. Later, lithospheric extension was caused by regional gravitational relaxation due to change of plate boundary kinematics. This synthesis demonstrates the complexities of MCC generation and highlights the need for better dating constraints for both brittle and ductile structures to make improved interpretations of MCCs globally.

1. Introduction

Continental metamorphic core complexes (MCCs) exhume metamorphosed, commonly migmatitic, middle-lower crust rocks along high-strain mylonitic shear zones (e.g., Davis and Coney, 1979; Whitney et al., 2013) (Fig. 1). MCCs are one of a several processes that vertically advect mass and heat in the lithosphere, which can impact rheology, crustal differentiation, growth of the continental lithosphere, and planetary cooling (Rudnick and Fountain, 1995; Petford et al., 2000; Lenardic et al., 2000; Beaumont et al., 2001; Vanderhaeghe, 2012; Moore and Webb, 2013; Rubin et al., 2017; Zuza et al., 2019). The hallmark characteristic of an MCC is the significant strain, metamorphic, and thermal gradient observed across the internal infrastructure rocks versus the overlying suprastructure rocks (e.g., Armstrong and Hansen, 1966) (Fig. 1). MCCs are generally interpreted to have formed as a result from high-magnitude regional extension, hanging wall removal due to normal faulting, and isostatic rebound of the footwall rocks with possible decompression melting (e.g., Wernicke, 1981; Davis, 1983; Rey et al., 2009a, 2009b). Diverse MCC or MCC-like systems are widely distributed around the world but are most often associated with convergent plate boundaries, such as subduction zones, that have experienced syn- or post-subduction extension (Fig. 2).

MCCs involve normal-sense juxtaposition of hotter, structurally deeper, and higher metamorphic grade lower-plate rocks beneath colder, structurally shallower, and lower metamorphic grade rocks (e.g., Lister and Snoke, 1984; Whitney et al., 2013; Lister and Davis, 1989;

* Corresponding author at: Nevada Bureau of Mines and Geology, University of Nevada, Reno, NV 89557, United States.
E-mail address: azuza@unr.edu (A.V. Zuza).

https://doi.org/10.1016/j.earscirev.2024.104987
Received 20 December 2023; Received in revised form 4 November 2024; Accepted 6 November 2024
Available online 12 November 2024

Fossen and Cavalcante, 2017). Over decades of research, our understanding of the formational and driving mechanisms of MCCs has changed dramatically. Past interpretations of MCC generation span from vertical buoyant ascent of the lower-plate rocks following plutonism and/or partial melting (Eskola, 1948; Armstrong and Hansen, 1966; Armstrong, 1968; Levy et al., 2023), horizontally driven high-magnitude regional extension and footwall rebound (e.g., Crittenden et al., 1980; Wernicke, 1981; Wernicke and Axen, 1988; Lister and Davis, 1989), or some combination therein (Rey et al., 2009b; Deng et al., 2020) (Fig. 3). In this review, we evaluate the geometric and kinematic features of MCCs to better interpret their generation and provide suggestions toward a unifying model of their genesis.

MCC systems have been documented globally, including in North America, east Asia, and the Aegean region of Europe (Fig. 2). MCCs in these settings formed along subduction-zone convergent plate boundaries during broadly similar tectonic events with a preceding phase of migrating magmatism caused by slab flattening and steepening followed by MCC formation (e.g., Armstrong and Ward, 1991; Wang et al., 2011; Li and Li, 2007; Jolivet and Brun, 2010; Jolivet et al., 2013; Ji et al., 2018; Rabillard et al., 2018; Wu et al., 2019; Zuza and Cao, 2023) (Fig. 2). Herein, we focus on MCCs in the North American Cordillera, where seminal research in the 1970s and 1980s greatly improved our understanding of MCC evolution and more broadly of continental tectonics and intracontinental extension (e.g., Anderson et al., 1972; Coney, 1974, 1980; Crittenden et al., 1980; Lister and Davis, 1989) (Fig. 2B).

We pose two guiding questions to organize this review:

First, to what extent are the various structural features of an MCC kinematically and dynamically linked? There are numerous features associated with MCCs (Fig. 1), such as a metamorphosed, commonly migmatitic lower plate, pre−/syn-kinematic intrusions, mylonitic shear zone, brittle normal faults that may have initiated at low angles, and high-angle normal faults. There is a spectrum of possibilities, where these features are all kinematically and temporally related or they may be distinct and unrelated elements that are exhumed to coexist today at the Earth's surface.

Second, what primarily drives MCC generation? End-member driving mechanisms can be distilled into those that act horizontally versus those driven by vertical forces. One perspective is that horizontal crustal extension driven by plate-boundary conditions leads to hanging wall removal and isostatic rebound of the lower plate rocks (e.g., Wernicke, 1981; Wernicke and Axen, 1988) (Fig. 3A). On the other hand, vertical motions of hot, partially melted buoyant rock, like an ascending pluton, can form diapiric gneiss domes with little or no aid from horizontal lithospheric stretching (Eskola, 1948; Yin, 2004) (Fig. 3B). Between these end members exists a continuum of scenarios where different drivers influence MCC evolution globally, potentially varying in time and space.

2. Characteristics of metamorphic core complexes

2.1. Features of a metamorphic core complex and related structures

Coney (1980) coined the term "metamorphic core complex" in a synthesis volume edited by Crittenden et al. (1980), modifying a reference from Wheeler (1966) to a "metamorphic core zone" from his study of the Canadian MCCs. More recently, Whitney et al. (2013, p. 273) offered a relatively succinct definition of an MCC as "domal or arched geologic structure composed of ductilely deformed rocks and associated intrusions underlying a ductile-to-brittle high-strain zone that experienced tens of kilometers of normal-sense displacement in response to lithospheric extension." Several systems discussed in the literature are similar to an MCC, including migmatite-cored MCCs, gneiss domes, and detachment-fault systems. The addition of the prefix "migmatite-cored" to describe MCCs has been used to describe systems where the lower plate involved voluminous syn-kinematic partial melts and migmatite generation, which would have reduced the bulk viscosity and density to drive crustal flow and buoyant rise of the lower-plate rocks (Rey et al., 2009a, 2009b; Whitney et al., 2013; Deng et al., 2020; Jolivet et al., 2021). The term gneiss dome (Eskola, 1948) describes when partial melting and remobilization of the middle-to-lower crust leads to buoyant upwelling or doming, which may take place in extensional, neutral, or contractional tectonic settings (e.g., Teyssier and Whitney, 2002; Yin, 2004; Jessup et al., 2019; Louis-Napoléon et al., 2020, 2024). In recent literature on the North American Cordillera, the term gneiss dome is often used to describe MCC-like structures that formed in the absence of observed regional extension and high-magnitude normal faulting (e.g., Konstantinou et al., 2012, 2013; Zuza et al., 2021). Therefore, a gneiss dome can be considered a sub-category of MCCs if the lower plate is exhumed primarily via partial melting and buoyant diapirism (Fig. 3B), instead of by regional extension, hanging wall removal, and isostatic rebound (Fig. 3A). However, not all gneiss domes are MCCs because a gneiss dome without a brittle detachment fault does not constitute an MCC as defined and observed in the North American Cordillera (e.g., Coney, 1980; Whitney et al., 2013).

There are several other mechanisms that can generate gneiss-dome-like or MCC-like structures in a contractional regime, such as folding or duplex development (see review by Yin, 2004). Recent discussions do not tend to favor these interpretations in the context of the North American Cordillera MCCs. However, past workers have invoked crustal duplexing and mid-crustal shearing to interpret Cordillera MCCs, especially in the Canadian Cordillera (e.g., Price, 1981; Armstrong, 1982; Brown et al., 1986; Crowley et al., 2001).

Two other related terms include detachment fault, which is a fault

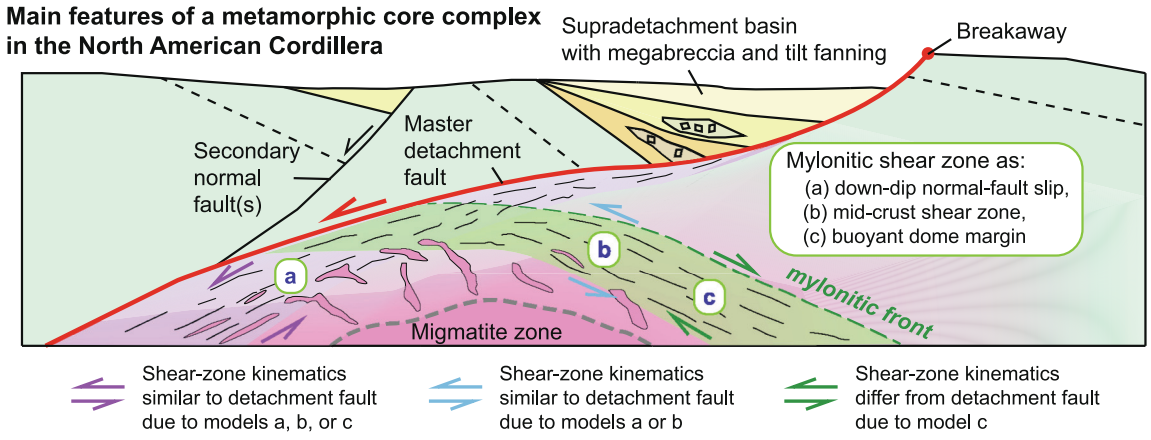

Fig. 1. Common components of a metamorphic core complex within the North American Cordillera. See text for discussion.

structure that forms at a relatively low dip angle but ultimately cuts layering and ramps across stratigraphy, and a décollement, which is primarily used to describe a relatively weak zone in the mechanical stratigraphy or rheological layering that focuses deformation. A detachment-fault system refers to a structural system with a regionally extensive (e.g., mountain range or broad map scale), often low-angle, fault that separates hanging wall rocks from the footwall. Relevant to MCCs, the discussed detachment-fault systems involve normal-sense kinematics, as opposed to a décollement or detachment in a major thrust fault system or a landslide structure where the term detachment was originally coined (e.g., Pierce, 1957, 1975). Detachment normal faults juxtapose younger rocks on older rocks, or lower grade rocks on higher grade rocks. Unlike a complete MCC system, a detachment-fault system may not involve a ductilely deformed lower plate with syn-kinematic intrusions. Herein, we use detachment fault to refer to a brittle, normal fault system that is generally low angle to either the bedding or foliation that it cuts. Unlike a classic décollement structure, a detachment fault cuts across foliation or bedding. There are major brittle detachment (normal) fault systems in North America that are not considered MCCs, such as the Pilot Peak (Miller et al., 1987), Grant Range (Long and Walker, 2015), or Mormon Mountains (e.g., Wernicke et al., 1985) detachment fault systems.

There are four primary components to a typical Cordilleran MCC system (Fig. 1): (1) a metamorphic/crystalline core, (2) a mylonitic shear zone, (3) a major normal-fault (usually low-angle or detachment) fault system, and (4) a supradetachment basin. The lower plate or footwall of the MCC system consists of a moderate-to-high-grade metamorphic and/or crystalline core that may be voluminously intruded by plutons that are pre-, syn-, or post-kinematic with respect to overall MCC evolution (Fig. 1). A mylonitic shear zone is developed within the structurally higher or mantling positions of this lower plate, which may be overprinted by chloritic alteration and brittle brecciation.

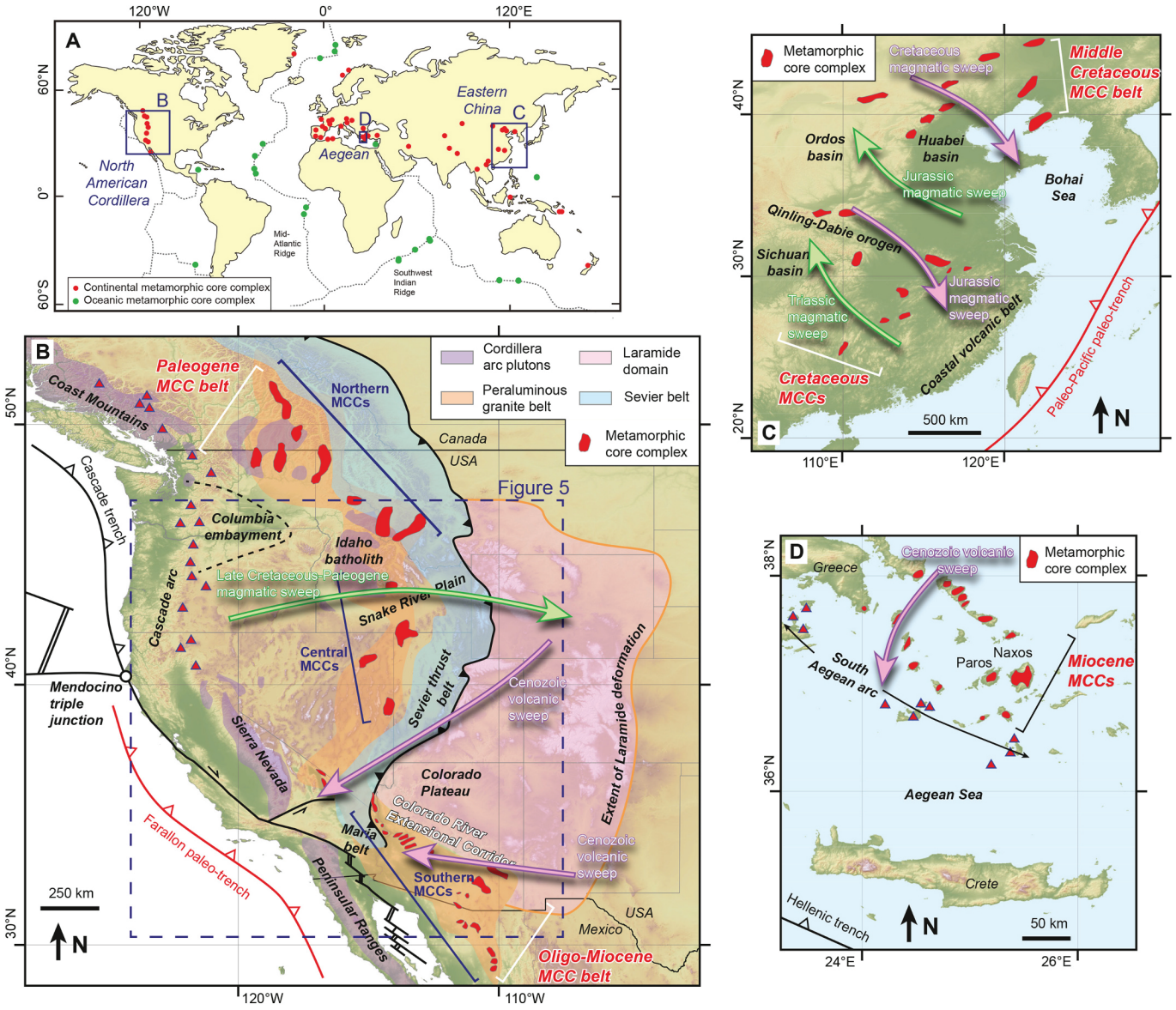

Fig. 2. Maps of metamorphic core complexes (MCCs) on Earth. (A) Global map of MCCs, modified from Whitney et al. (2013). (B) Tectonic map of the North American Cordillera, showing how the belt of MCCs relates to other major elements within the Cordillera. Figure adapted from Yonkee and Weil (2015) and Chapman et al. (2021). (C) Tectonic map of eastern China showing MCCs and their relationship to the Paleo-Pacific paleo-trench and migrating Mesozoic magmatic sweeps in southern and northern China. MCC locations from Wang et al. (2011) and Ji et al. (2018) and magmatic trends from Li and Li (2007) and Wu et al. (2019). (D) Tectonic map of the Aegean showing the relationship between MCCs, subduction, and the southward magmatic sweep. Compiled from Jolivet and Brun (2010), Jolivet et al. (2013) and Rabillard et al. (2018).

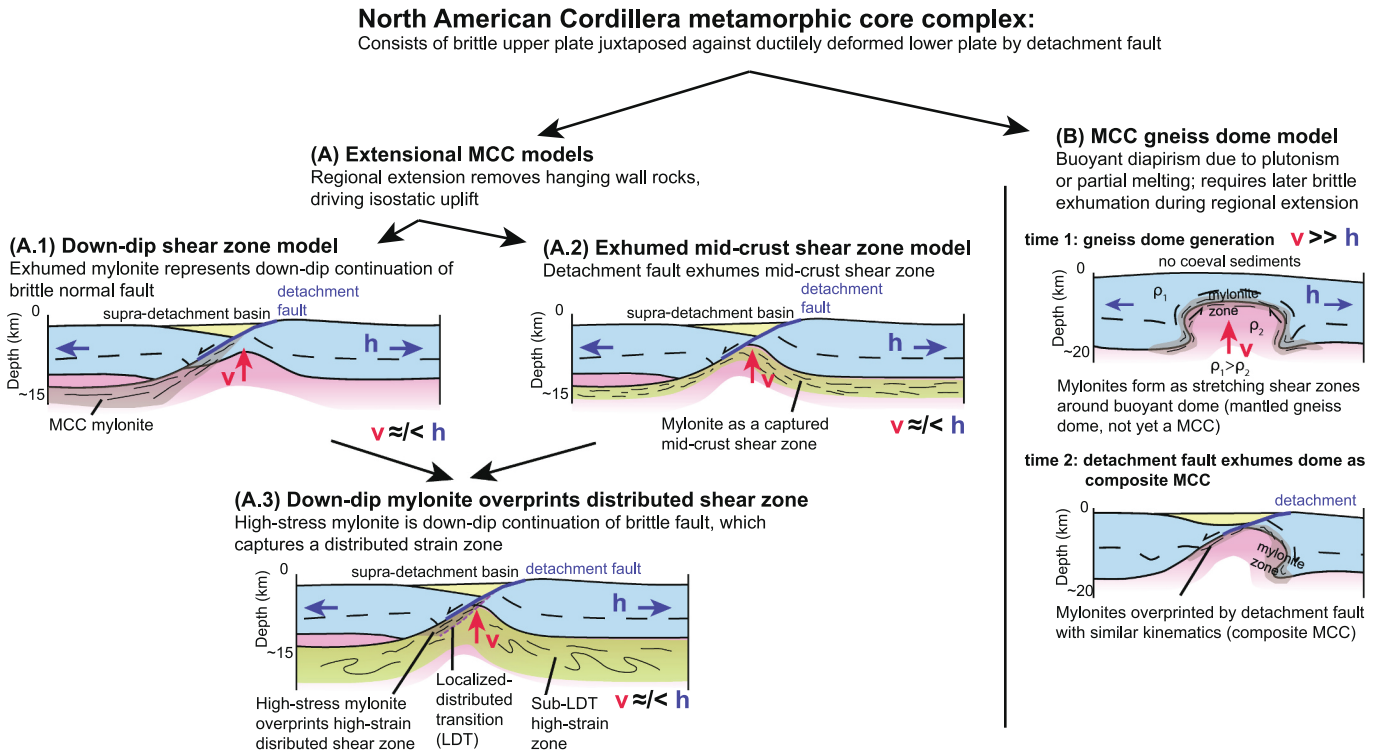

Fig. 3. Comparison of models for North American Cordillera metamorphic core complex (MCC) formation, comparing vertical lower-plate advection (v) versus horizontal stretching (h). (A) Regional extension may drive normal-faulting, hanging wall removal, and isostatic rebound. The mylonitic shear zone may represent the down-dip continuation of the brittle normal fault (A.1) or a captured mid-crust shear zone (A.2). A hybrid model considers how high-stress mylonites related to the detachment fault overprint and exhume a more distributed ductile shear zone (A.3) (e.g., Cooper et al., 2017). (B) Heating and partial melting of the middle-to-lower crust may drive buoyant doming. ρ_1 and ρ_2 are the density of the upper and lower crust, respectively. To be consistent with the observed North American MCCs, the buoyant gneiss dome are later exhumed by a normal-fault system.

The mylonitic shear zones are observed to have thicknesses from 10s to 1000s of m. The mylonites show high-stress, low-temperature (300–500 °C) fabrics that correlate with their small recrystallized grain size (e.g., Behr and Platt, 2011; Platt et al., 2015; Cooper et al., 2017). Depending on exposure level, it may be possible to observe the top and bottom of the mylonitic shear zone. When exposed, the structurally highest "top" of the mylonitic shear zone is referred to as the mylonitic front (e.g., Davis et al., 1980; Davis, 1988) (Fig. 1). Structurally beneath the mylonitic shear zone, strain may be diffusely distributed or dissipate—referred to as a the localized-distributed transition (LDT) (Cooper et al., 2017)—where the rocks show a coarser grainsize, migmatitic textures, and/or voluminous syn-kinematic plutons (e.g., Strickland et al., 2011; MacCready et al., 1997) (Fig. 1).

Structurally above the mylonitic shear zone is a brittle normal-fault system, which is commonly low-angle to the regional foliation, that separates the lower plate from an overlying low-grade to unmetamorphosed upper plate. The brittle normal fault commonly involves brecciation, cataclasis, and chloritic alteration, especially in the footwall rocks (e.g., Sibson, 1977; Davis, 1987, 2013; Lister and Davis, 1989). Brittle normal faulting in an MCC system may form a syn-kinematic basin within the hanging wall (Fig. 1). This basin will form above the detachment fault and is referred to as a supradetachment basin (e.g., Yin and Dunn, 1992; Dorsey and Becker, 1995; Friedmann and Burbank, 1995; Prior et al., 2018). These syn-kinematic basins are commonly filled with (mega-)breccia, conglomerates, and interbedded volcanic deposits. Because the basins form during progressive fault slip, they exhibit growth strata, tilt-fanning relationships where the dips of the strata vary within the sedimentary thickness (e.g., Dickinson, 1991; Gans and Bohrson, 1998; Satarugsa and Johnson, 2000; Faulds et al., 2001; Cheng et al., 2023). Lacustrine siliciclastic or carbonate deposits reflect the generation of closed basins during fault slip in adjacent mountain ranges. Changes in clast compositions track footwall exhumation, with undeformed, supracrustal cobbles in the lower stratigraphic units transitioning mylonitic/plutonic cobbles as the core of the MCCs are progressively denuded (e.g., Miller and John, 1988, 1999; McGrew and Snoke, 2015). When possible, absolute ages from volcanic or detrital units within the supradetachment basins can provide relatively tight timing constraints on the age of brittle fault slip (e.g., Gans and Bohrson, 1998; Faulds et al., 2002; Zuza et al., 2021).

2.2. *End-member drivers for MCC development in the North American Cordillera*

Driving mechanisms for North American MCC formation discussed in the literature can be divided into two broad categories: (1) regional extension and coupled footwall exhumation and (2) buoyant gneiss-dome diapirism that is impacted by later extension (Fig. 3). The first category can be further subdivided. One model envisions that the mylonitic shear zones represent the down-dip continuation of a brittle detachment fault (i.e., "down-dip shear zone" model; Fig. 3A.1) (e.g., Wernicke, 1981; Wernicke and Axen, 1988). An alternative extensional model suggests that brittle normal faulting captures and exhumes a preexisting mid-crust mylonitic shear zone (i.e., "exhumed mid-crust shear zone" model; Fig. 3A.2) (Davis, 1988; Singleton and Mosher, 2012). In the down-dip normal fault shear zone model, regional stretching of the crust is accommodated by normal faults that remove a significant mass of hanging wall rocks (Fig. 3A.1). The removal of the hanging wall overburden results in isostatic rebound of the footwall (Wernicke and Axen, 1988). The magnitude of isostatic rebound depends on the rates of extension versus competing supradetachment sedimentation and the strength parameters of the lower crust (e.g., rigidity or viscosity) (e.g., Issler et al., 1989). During footwall rebound,

vertical rock advection can result in decompression partial melting, which can further enhance footwall rebound due to the reduced density and viscosity. This model predicts bulk crustal extension strain rates that are comparable to footwall exhumation strain rates (Fig. 3A.1). Normal faulting may involve low-angle detachment slip that links into a deeper mylonitic shear zone (Wernicke, 1981), a high-angle master normal fault that gets rotated during isostatic footwall uplift as a rolling hinge (Buck, 1988; Wernicke and Axen, 1988), or a series of high-angle normal faults that together rotate to lower angles as dominos or bookshelf fault systems (e.g., Proffett Jr, 1977; Favorito and Seedorff, 2021).

In the mid-crust shear-zone model, MCCs form as a composite system, where a brittle-normal fault captures a sub-horizontal mid-crust shear zone that is accommodating regional extension (e.g., Davis, 1988) (Fig. 3A.2). This model was developed based on the recognition of a mylonitic front in the Whipple Mountains located underneath, and dipping away from, the detachment fault (e.g., Fig. 1). The recognition that observed mylonitic shear zones are not uniquely spatially associated with brittle detachment faults, which has also been observed in Buckskin-Rawhide (Singleton and Mosher, 2012) and Ruby Mountains (e.g., Colgan et al., 2010), suggests that detachment faults were not intrinsically linked or coupled with the exhumed mylonitic shear zones. Mylonitic shearing predates detachment-fault slip, which is evidence that a younger detachment fault captured an older, but kinematically similar, mid-crust shear zone.

Cooper et al. (2017) provided an updated interpretation that combined aspects of the above two models. They suggest that the mid-crust experiences distributed, high-strain deformation beneath the LDT, and this high-strain zone is overprinted and exhumed by a major normal-fault system that includes a brittle detachment fault and coupled high-stress mylonitic shear zone. Therefore, the high-stress mylonites represent the down-dip component of the brittle detachment fault, similar to the down-dip shear zone model, that captures a preexisting high-strain distributed shear zone in the middle-to-lower crust, broadly similar to the mid-crust shear zone model (Fig. 3A.3). The mylonitic front is the top of the LDT in this model.

Alternatively, the gneiss dome models suggest that vertical buoyant doming of the middle-to-lower crust generated a domal architecture that was subsequently captured by later normal faulting (i.e., "buoyant doming" model; Fig. 3B). This process is driven by buoyancy forces, where lower density conditions in the middle-to-lower crust causes doming relative to the denser upper crust. The density of the middle-to-lower crust can be reduced by plutonism and partial melting caused by crustal thickening, flux melting, or increased mantle heat flux (e.g., Houseman et al., 1981; Thompson and Connolly, 1995; Vanderhaeghe, 2009). Buoyant doming could occur in neutral, compressional, or extensional tectonic regimes, and is analogous to processes of pluton ascent and emplacement (e.g., Sylvester et al., 1978; Burov et al., 2003; He et al., 2009; Paterson and Fowler, 1993). Potential caveats to this model is the space issue where domal upwelling must be balanced by equivalent downwelling or crustal stretching (e.g., Dixon, 1975) or the efficacy of moderate-degree partial melting (<30 % melt) and buoyancy to exhume mid-crust rocks (e.g., Rey et al., 2009a, 2009b). Buoyancy-driven MCCs can have exhumation rates greater than or equal to bulk extension rates (Fig. 3B). A buoyant dome will stall in the middle crust as it cools (time 1 in Fig. 3B), much like an emplaced pluton, so this model requires exhumation to the surface via a later phase of faulting (time 2 in Fig. 3B) to form a composite MCC. In the North American Cordillera, this later phase of exhumation can be facilitated by brittle normal faulting, but in other tectonic settings exhumation may occur due to shortening and coupled erosion (e.g., Yin, 2004).

Distinguishing MCC generation models can be accomplished by resolving the geometric and kinematic relationships between the detachment fault and mylonitic shear zone. Ideally, timing constraints for either structure can be determined via cross-cutting relationships, thermochronology, petrochronology, syn-kinematic basin records, or regional inference. For the ductile mylonitic shear zone, it is important to assess the existence of single vs multiple phases of deformation, the consistency of kinematics across the structure, and the temperatures of deformation.

A particularly diagnostic feature may be the structural relationships between the brittle detachment fault and mylonitic shear zone (Fig. 4). The classic historical recognition of the mylonitic front in the Whipple Mountains dipping away from the detachment challenged the earlier notion that the mylonite was the down-dip continuation of a kinematically linked detachment fault (Davis et al., 1980; Davis, 1988) (cf. Fig. 3A.1). This observation led to the reevaluation of the Whipple detachment fault as capturing a mid-crust shear zone (Davis, 1988) (Fig. 3A.2). Similar observations have been made in other North American MCC systems (e.g., Reynolds and Lister, 1990; Singleton and Mosher, 2012).

In the present-day surface exposure, the brittle detachment fault may be restricted to one side of the ductile lower plate (Fig. 4A) or it may fully encircle the lower plate (Fig. 4B) due to isostatic upwarp (Wernicke and Axen, 1988). If the detachment fault fully encircles the lower plate as a window, there must be a fault breakaway located up-dip of the normal fault (Fig. 4B). If the mylonitic shear zone is simply the exhumed down-dip component of the detachment fault, there should not be an observed mylonitic front (i.e., the structural top of the mylonite) (Fig. 4C). Depending on erosional level, the base of the mylonite may be observed as a complete- or half-window. If the detachment fault captures a mid-crust shear zone, it is possible to observe the top of the shear zone, the mylonitic front (Fig. 4D). Lastly, detachment-fault capture of a gneiss dome can result in complex 3D patterns, where the top or bottom of the mylonitic shear zone is observed (Fig. 4E). Uniquely, this model could result in opposing shear kinematics (scenario j in Fig. 4E). In this review, while describing each MCC system, we attempt categorize the map relationships in each MCC between detachment fault and mylonitic shear zone based on the criteria in Fig. 4.

In the North American Cordillera, these different models make specific predictions for the relationships between MCC development and (1) plate-boundary conditions, specifically the transition from convergent to transform plate boundaries, (2) the timing of achieving peak-crustal thickness and subsequent relaxation of gravitational potential energy (GPE), and (3) spatial and temporal trends of volcanism and magmatism. For example, the down-dip normal fault and exhumed mid-crust shear zone models predict that MCC generation should initiate when body forces (e.g., GPE) and plate-boundary conditions are conducive to regional extension. Lithospheric extension may be caused by a combination and competition between gravitational collapse of overthickened crust and changes in plate-boundary conditions (Dewey, 1988; Jones et al., 1998; Sonder and Jones, 1999; Rey et al., 2001; Vanderhaeghe and Duchêne, 2010). Relevant to the North American Cordillera, extensional MCC development would be expected to initiate following one of several possible geodynamic events: (1) after the attainment of peak crustal thickness in the Late Cretaceous (e.g., DeCelles, 2004; Chapman et al., 2015), (2) during Paleogene rollback following the Laramide flat-slab event (e.g., Cassel et al., 2018), or (3) during the Oligocene-Miocene migration of the Farallon-Resurrection-Kula, Mendocino, and Rivera triple junctions to generate a free lateral boundary condition for the crust to extend (e.g., Ingersoll, 1982; Colgan and Henry, 2009).

The buoyant dome model predicts that magmatism, crustal heating, and partial melting drives MCC formation, and therefore there should be parallel trends between magmatism and MCC generation. The down-dip normal fault and exhumed mid-crust shear zone models do not specifically require magmatism, but elevated crustal temperatures due to magmatism could weaken the lithosphere to drive enhanced extension and MCC generation (e.g., Gans et al., 1989; Gans and Bohrson, 1998; Zuza et al., 2019).

The lithospheric extension models predict Moho relief that is not observed, which has been explained via lower-crustal flow or decoupled upper crust-lower crust stretching (e.g., Gans, 1987; McCarthy et al.,

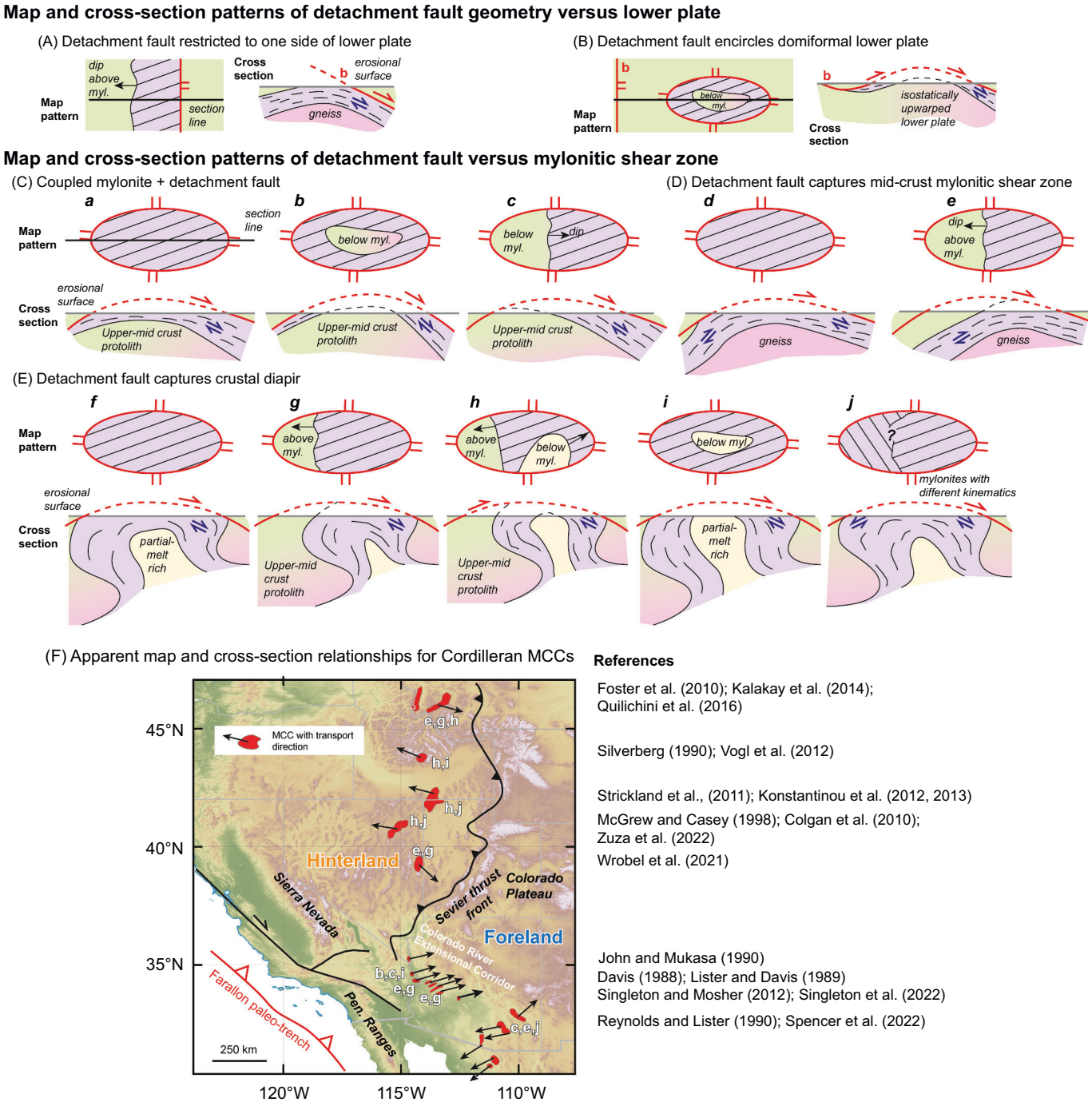

Fig. 4. Map and cross-section patterns for detachment fault geometries compared to the mylonitic lower plate. The detachment fault may (A) be restricted to one side of the lower plate or (B) encircle the entire lower plate as the footwall isostatically rebounds following progressive hanging wall removal. Either scenario may occur regardless of the formation mechanism of a metamorphic core complex. Breakaway (b) is labelled. (C-E) Sketches of possible variations of the map patterns and cross-section relationships between the detachment fault (red) and mylonitic shear zone (purple), as implied for (A) the mylonite zone representing the downdip continuation of the detachment fault, (B) the detachment fault capturing a mid-crust mylonitic shear zone, and (C) the detachment fault capturing a crustal diapir. For all cases in C-E, for simplicity the detachment fault is shown encircling the lower plate (panel B), but the same relationships could occur if the detachment -fault is restricted to just one side of the lower plate (panel A). In panels A-E, the detachment-fault transport direction is east, to the right, in all sketches. (F) Map of metamorphic core complexes in the North American Cordillera with interpreted detachment-mylonite relationships lettered from panels C-E, based on the provided references in the right-hand column. (For interpretation of the references to colour in this figure legend, the reader is referred to the web version of this article.)

1991; Buck, 1991; Say and Zuza, 2021). Conversely, the buoyant doming model does not predict significant Moho displacement or discrete offsets. In this sense, all MCC models predict some mid-lower crustal mobility, either directly within a crustal diapir or indirectly to smooth out expected Moho topography.

3. Metamorphic core complexes in the North American Cordillera

The belt of MCCs in the North American Cordillera stretch from Canada to Mexico (Fig. 2B and 5). They are commonly divided into (1) the northern belt, from the first MCC north of the Snake River Plain (i.e.,

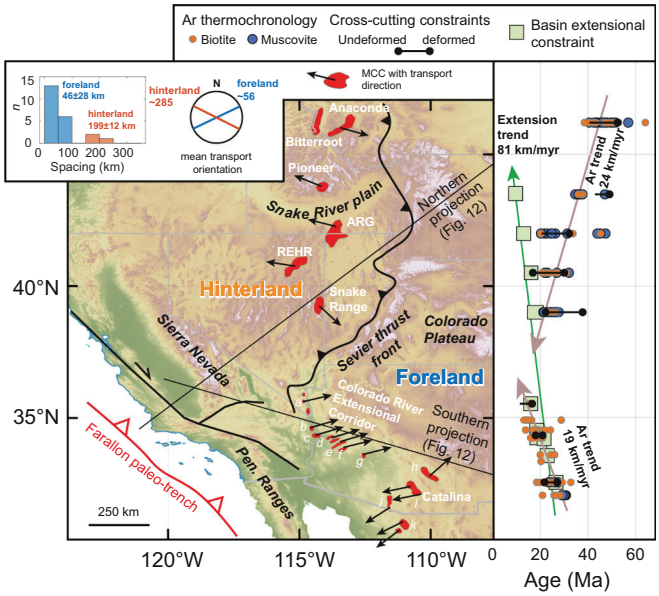

Fig. 5. Metamorphic core complexes (MCCs) in the hinterland and foreland of the Sevier thrust front in the North American Cordillera. Figure modified from Zuza and Cao (2023). Foreland MCCs: a—Dupont Mountain fault; b—Sacramento and Chemehuevi; c—Whipple Mountains; d—Buckskin-Rawhide; e—Harcuvar; f—Harquahala; g—South Mountain; h—Pinaleño; i—Catalina-Rincon; j—Coyote; k—Magdalena. The right panel shows timing constraints vs longitude compiled for each MCC, including biotite and muscovite $^{40}Ar/^{39}Ar$ dates, timing constraints for ductile shearing based on cross-cutting relationships, and ages for syn-kinematic basin deposits (note basin-age uncertainty is smaller than symbol size). See text for discussion and references.

the Pioneer MCC) to the Shuswap complex in British Columbia, (2) the central belt from northern Snake Range to the Albion-Raft River-Grouse Creek, and (3) the southern belt from southern Nevada through Arizona to northern Sonora (Fig. 2B). This three-way division is based on distinct timing constraints, extension magnitudes, and relative involvement of partial melting (e.g., Whitney et al., 2013).

In this study, we divide the MCCs between the north and the south based on a pronounced metamorphic core complex dichotomy with distinct (1) timing trends, (2) map-view spacing patterns, and (3) structural positions relative to the hinterland of the Cordilleran orogen (e.g., Zuza and Cao, 2023) (Fig. 5). Namely, those located in the north between Las Vegas, Nevada and British Columbia, Canada are relatively larger, spaced ~200 km apart, and show age trends that broadly young toward the south from the Paleocene to the Oligocene. These MCCs are located west of the Sevier fold-thrust front, and therefore would have formed in the hinterland of the Cordilleran orogen. We refer to these MCCs as hinterland MCCs. In the simplest configuration, hinterland MCCs formed in a thickened orogenic plateau that is referred to as the Nevadaplano (e.g., DeCelles, 2004). Conversely, in the south, MCCs stretch across the Colorado River Extensional Corridor (CREC) from southern Nevada to northern Sonora, with closer spacing (~50 km), and broadly west-northwest-younging age trends. These MCCs are located east of—that is, forward of—the main fold-thrust front of the Sevier and Maria thrust belts, and therefore we refer to these MCCs as foreland MCCs (e.g., Zuza and Cao, 2023) (Fig. 2B).

Our synthesis spans from the Bitterroot-Anaconda MCC in the north to the MCCs in southern Arizona in the south (Fig. 5). We limit the spatial extent of our analysis to this region for several reasons. First, MCCs to the south into Mexico (Fig. 2B) are less well studied, which makes along-strike comparisons more challenging. Second, our chosen spatial extent overlaps regions impacted by well-constrained Sevier fold-thrust belt deformation, and the hypothesized flattening of the Farallon slab (i.e., the Laramide) and subsequent slab rollback with associated magmatism, such that MCC evolution can be considered within the context of a reasonably well constrained Cordilleran tectonic history (e.g., Dickinson, 2004; DeCelles, 2004; Yonkee and Weil, 2015; Copeland et al., 2017) (Fig. 2B). The geology of southwestern Canada is complicated by terrane collisions and potential lateral terrane translations (e.g., Irving et al., 1985; Cowan et al., 1997; Krijgsman and Tauxe, 2006; Rusmore et al., 2013; Tikoff et al., 2023). Third, we aim to compare MCC generation to the evolution of a coupled diachronous set of migrating triple-junction systems—the Mendocino and Rivera triple junctions (Atwater, 1970)—whereas the analysis of the northern MCCs is further obscured by the debated slab window or tear between the Resurrection and Farallon plates (e.g., Thorkelson and Taylor, 1989; Breitsprecher et al., 2003; Madsen et al., 2006; Schmandt and Humphreys, 2011; Schmandt and Humphreys, 2011).

Although we do not incorporate data from the northern MCC belt (Fig. 2B) of southwestern Canada and the northwestern USA into this synthesis, here we briefly summarize their geology to provide a cursory comparison with the MCCs to the south. The northernmost MCCs are commonly described as migmatite-cored MCCs or gneiss domes, including the Okanogan-Kettle gneiss domes (Washington state, USA) and the Shuswap MCC (British Columbia, Canada) (e.g., Kruckenberg et al., 2008; Vanderhaeghe, 1999; Vanderhaeghe et al., 2003). The lower-plate rocks of these domes consist of significant volumes of migmatite that record protracted partial melting from ca. 60–50 Ma (Kruckenberg et al., 2008; Gordon et al., 2008). The domes are defined by outward dipping foliations, and the mylonitic shear zones that mantle the domes yield dome-up kinematics (e.g., Kruckenberg et al., 2008). In summary, the northernmost MCCs display structural and metamorphic features that are most consistent with a gneiss dome origin for their formation (Whitney et al., 2004), which provides useful context in which to interpret MCCs located further to the south.

Below we review the main metamorphic, igneous, and structural characteristics of the central and southern MCCs (Fig. 5). We link these descriptions to recreated geologic map (Fig. 6) and cross section (Fig. 7) sketches available in the literature.

3.1. *Bitterroot and Anaconda MCCs*

The north-trending Bitterroot MCC and northeast-trending Anaconda MCC are located at the same ~46°N latitude, ≤100 km apart (Fig. 5). The Bitterroot MCC is located along the eastern extent of the Late Cretaceous Idaho batholith. The lower-plate rocks consist of predominately Idaho batholith rocks, with some magmatic state fabrics observed (LaTour and Barnett, 1987; Quilichini et al., 2016). Intruded metasedimentary rocks in the lower plate experienced peak metamorphic conditions of 6.5–7.5 kbar and 600–750 °C at ca. 65–53 Ma (Foster et al., 2001). Upper plate rocks consist of the metasedimentary Sapphire block, which was translated eastward along an east-dipping ~0.5–1-km-thick mylonitic shear zone (e.g., Quilichini et al., 2016).

The Anaconda MCC (Fig. 5) is located to the east of the Bitterroot MCC. The lower plate consists of Late Cretaceous to Eocene granitic plutons intruding metamorphosed Mesoproterozoic Belt supergroup and Paleozoic rocks (Fig. 7A) that record peak pressures of 4.6–6 kbar in the Late Cretaceous (Grice, 2006; Haney, 2008; Kalakay et al., 2014). These lower plate rocks are commonly deformed in nappe-like fold structures, such as the Lake of the Isle shear zone. On the eastern flank of the Anaconda Range is a mylonitic shear zone that is 300–500 m thick, which records top-east-southeast shear (Kalakay et al., 2014; Foster et al., 2007, 2010). The overlying top-southeast Anaconda detachment separates the footwall from hanging-wall rocks. The hanging wall consists of conglomerates, breccias, megabreccias, and sandstones unconformably overlying lava flows, tuffs, and volcaniclastic units of the (ca. 54–48 Ma) Lowland Creek Volcanics (Howlett et al., 2021). The central part of the range consists of attenuated Proterozoic-Paleozoic stratigraphy that may reflect Cretaceous or Eocene shear zones (e.g., Grice,

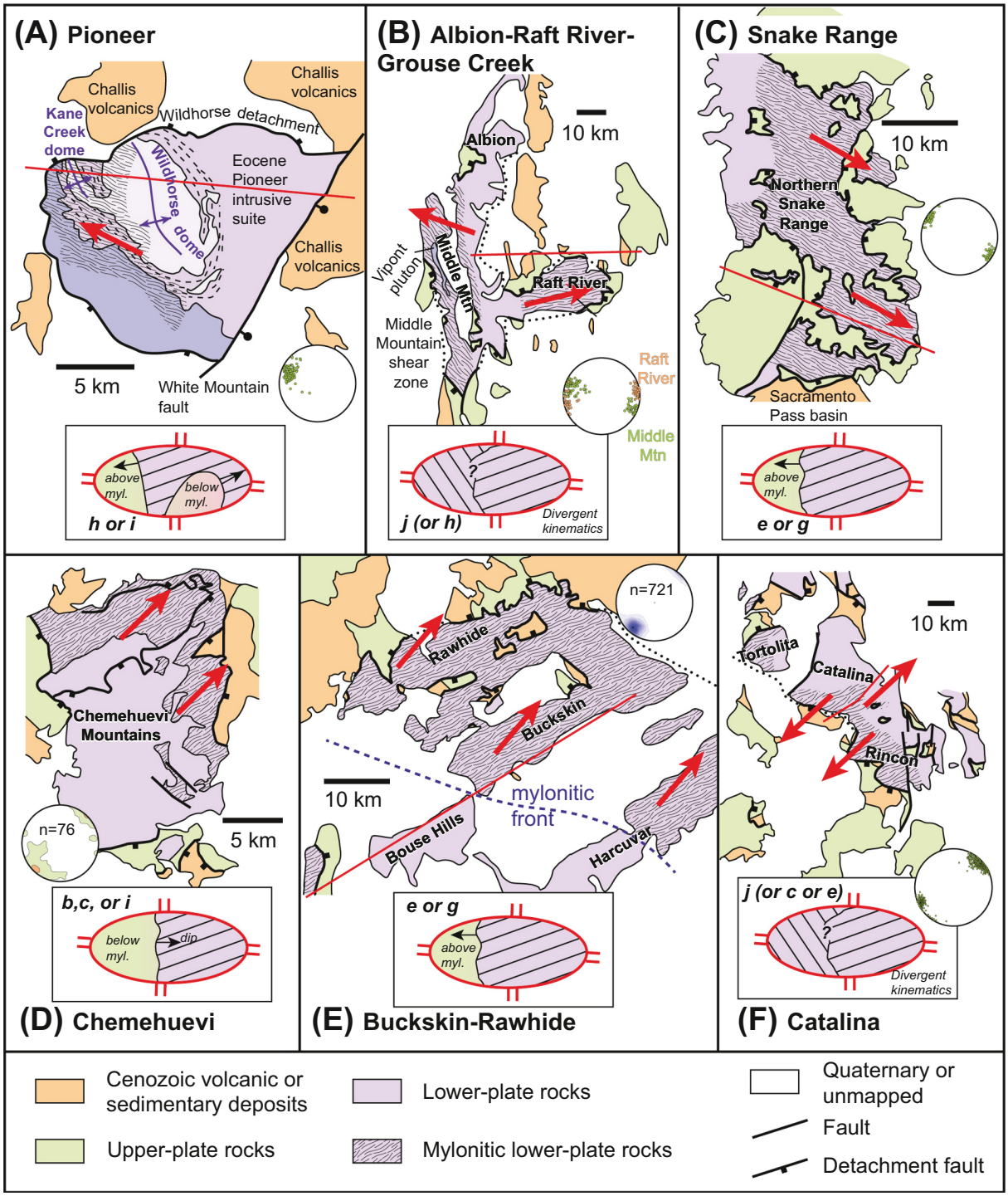

Fig. 6. Sketch geologic maps from several metamorphic core complexes highlighting the relationships between the lower-plate rocks and the detachment fault. Red arrow is dominant shear sense within lower-plate shear-zone rocks. Red line shows approximate location of cross sections in Fig. 7. Inset stereonets show orientations of stretching lineations. In each panel we highlight diagrammatic sketches of our interpreted mylonite vs detachment-fault relationships, in the same style and lettering as Fig. 4A-E. Maps and representative lineation plots redrafted from the following sources: (A) map and lineations from Vogl et al. (2012); (B) map from Konstantinou et al. (2012), lineations from Saltzer and Hodges (1988) and Wells (1991); (C) map from Hoiland et al. (2022), lineations from Blackford et al. (2022); (D) map from LaForge et al. (2017), contoured lineations from John and Mukasa (1990); (E) map from Singleton et al. (2022), contoured lineations from Singleton and Mosher (2012); (F) map from Davis et al. (2019), lineations from Spencer et al. (2022). (For interpretation of the references to colour in this figure legend, the reader is referred to the web version of this article.)

2006; Foster et al., 2010; Kalakay et al., 2014). These ductile fabrics are deformed by the brittle Hidden Lake fault zone in the western part of the Anaconda range (O'Neill et al., 2004) (Fig. 7A). This relationship suggests that the western flank of the Anaconda range is either at a structural position above the Eocene mylonitic MCC shear zone or alternatively that the MCC mylonites are spatially restricted to the east beneath the Anaconda detachment fault.

Both the Bitterroot and Anaconda MCCs have the detachment fault

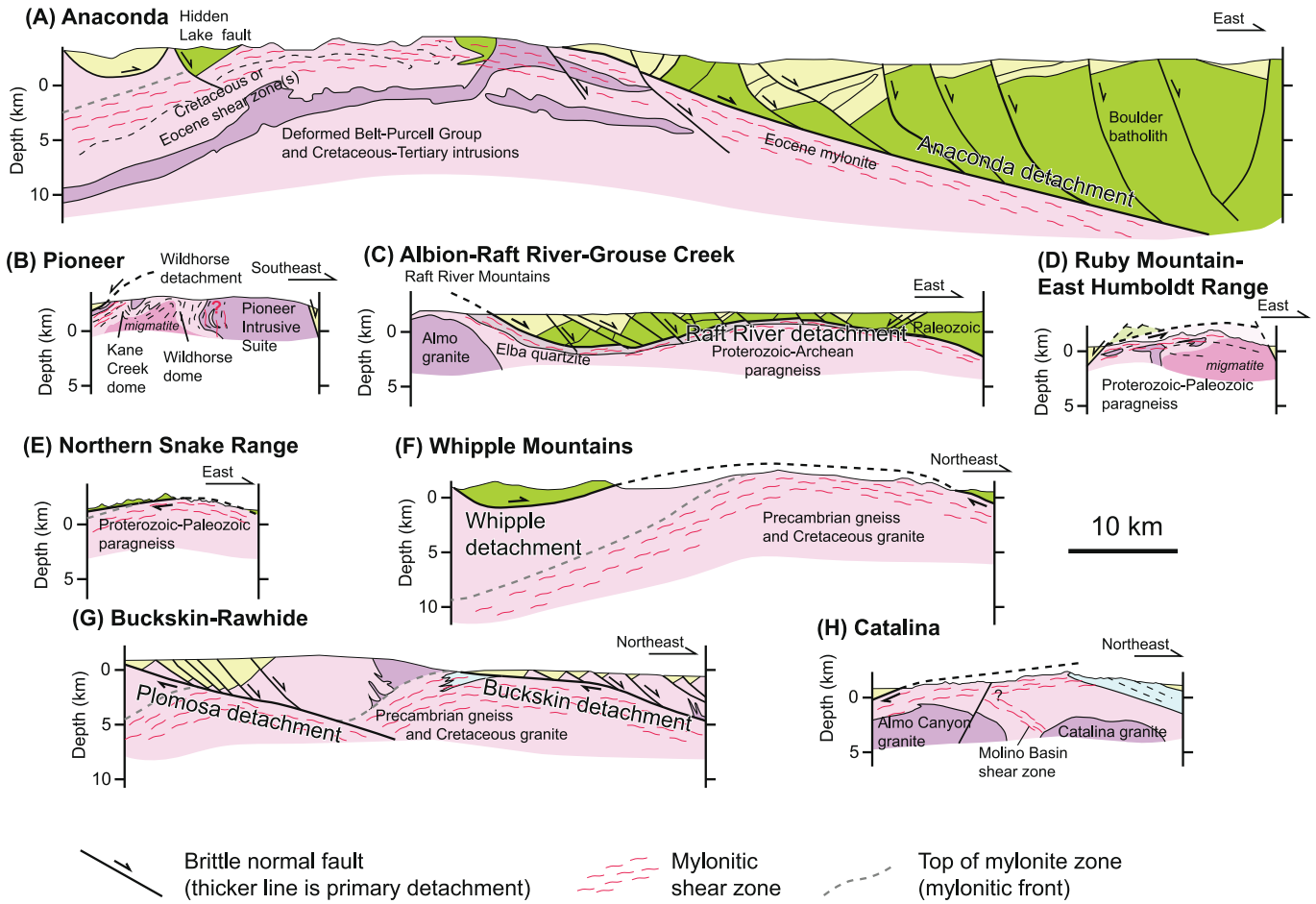

Fig. 7. Example cross sections at the same scales through representative metamorphic core complexes (MCC) within the North American Cordillera, arranged from north to south. Redrafted in the same style as the original references, with colors reflecting the lower (pink, purple) and upper (green, yellow) plates. The (A) Anaconda MCC (Foster et al., 2010), (B) Pioneer MCC (McFadden et al., 2015), (C) Raft River Mountains of the Albion-Raft River-Grouse Creek MCC (Konstantinou et al., 2012); (D) Ruby Mountain-East Humboldt Range MCC (Levy et al., 2023), (E) northern Snake Range MCC (Miller et al., 1999), (F) Whipple Mountains (from Platt et al., 2015, based in part on Davis, 1988), (G) Buckskin-Rawhide MCC (Singleton et al., 2014), and (H) Catalina MCC (Davis et al., 2019). (For interpretation of the references to colour in this figure legend, the reader is referred to the web version of this article.)

primarily exposed on the eastern flank of the lower plate (Fig. 4A), although some maps show the detachment encircling the lower plate (O'Neill et al., 2004) (e.g., Fig. 4B). The relationship between detachment fault and mylonitic shear zone may be consistent with scenarios e, g, and h in Fig. 4 because of the observations of a mylonitic front, with rock structurally above the mylonitic shear zone but below the detachment fault, and lower-plate rocks below the shear zone.

3.2. Pioneer MCC

The Pioneer MCC is located along the southeastern extent of the Late Cretaceous Idaho batholith in Idaho (Fig. 5). The lower plate consists of Proterozoic gneiss, and Paleozoic quartzite, marble, and metapelite (e.g., Dover, 1981, 1983; Link et al., 2007, 2010; Vogl et al., 2012). Peak metamorphic conditions were attained at ~4 kbar and 750 °C (Silverberg, 1990) in the Cretaceous (Vogl et al., 2012). The Precambrian rocks form two elongate NW-trending domes (i.e., the Wildhorse and Kane Creek domes) (e.g., Dover, 1983; Vogl et al., 2012). This domal geometry includes steep foliations along its flanks, including locally overturned limbs (McFadden et al., 2015) (Figs. 6A and 7B). The elongate domes are tilted eastward, evidenced by the overturning of the eastern dome limb, which is away from the interpreted top-northwest detachment-fault system observed predominately on the northwestern flank of the Pioneer MCC (Fig. 7B). Stretching lineations that are best developed in the Paleozoic rocks trend northwest, mostly parallel to anisotropy of magnetic susceptibility (AMS) observations in the footwall rocks (e.g., Wust, 1986; Vogl et al., 2012; McFadden et al., 2015). AMS magnetic lineations from the central Wildhorse dome trend north (Vogl et al., 2012).

The lower plate rocks were intruded by the ca. 49 Ma Pioneer Intrusive Suite (Silverberg, 1990; Vogl et al., 2012) and subsequently penetratively deformed by top-WNW shear that occurred during or after the emplacement of ca. 49 Ma granite (Vogl et al., 2012) (Fig. 6A). The shear distribution and kinematics in the southeastern parts of the Pioneer MCC are unknown, as most detailed structural mapping is in the northwest part of the MCC (e.g., Wust, 1986). Variable kinematics at differing structural levels imply vertical crustal decoupling within the Wildhorse dome. For example, at structural levels beneath the primary mylonitic shear zone with NW-trending lineations there are top-SSW shear zones along the flanks of the lower plate (Silverberg, 1990) and N-S trending AMS lineations within the core of the lower plate (e.g., Vogl et al., 2012). The primary detachment fault is known as the Wildhorse detachment, and its hanging wall includes the Eocene (ca. 50–45 Ma) Challis volcanic sequence (Figs. 6A and 7B). The detachment fault and related brittle structures overprint mylonitic shear zones. Vogl et al. (2012) noted that ductile fabrics are associated with the Wildhorse detachment in the northwest part of the Pioneer MCC, but in the southwest, ductile fabrics are not observed beneath the Wildhorse detachment.

The Wildhorse detachment wraps around more than half of the lower

plate but is truncated by the White Mountain fault in the southeastern extent of the Pioneer MCC (e.g., McFadden et al., 2015) (Fig. 6A). The relationship between detachment fault and mylonitic shear zone is consistent with scenarios h and i in Fig. 4 because of the observations of the structural dome beneath the mylonitic shear zone and the lack of deformation beneath some of the Wildhorse detachment in the southwest, potentially suggesting a structural position between the detachment and the mylonitic shear zone (Fig. 6A).

3.3. Albion-Raft River-Grouse Creek MCC

The Albion-Raft River-Grouse Creek (ARG) MCC of northwest Utah and southern Idaho (Fig. 5) exposes Archean-Proterozoic orthogneiss and paragneiss overlain by Proterozoic-Paleozoic quartzite and metapelites (Compton et al., 1977; Stewart, 1980; Wells et al., 1998). The lower plate rocks experienced Cretaceous burial and metamorphism to peak conditions of 7 kbar and 550–600 °C (Wells et al., 2012; Kelly et al., 2015). Scarcely preserved ductile Cretaceous fabrics with north-trending lineations and top-north shear kinematics have been dated to Late Cretaceous via in-situ $^{40}Ar/^{39}Ar$ analyses (Wells et al., 1997, 2008). The ARG preserves Eocene–Oligocene and Miocene magmatism. The Oligocene igneous rocks are isotopically more evolved than the Eocene rocks, suggesting progressive incorporation of crustal materials into the melts (Strickland et al., 2011; Konstantinou et al., 2013). Miocene volcanism is associated with the Snake River Plain volcanic province (e.g., Perkins et al., 1995).

There are two main shear zones in the ARG: the Middle Mountain shear zone in the west that displays WNW lineations and top-WNW kinematics and the Raft River shear zone in the east (Fig. 7C) with *E*-trending lineations and top-east kinematics (Fig. 6B). Overall, the ARG shear zones involve severe attenuation of well-constrained Proterozoic-Paleozoic stratigraphy, suggesting >80 % vertical attenuation (Fig. 8) (e.g., Wells, 1997). The Elba Quartzite was thinned from ~450 m thick to <20 m thick in this shear zone (Armstrong, 1968; Compton, 1972; Compton et al., 1977; Wells et al., 2000).

Above the mylonitic shear zones are the west-directed Middle Mountain and east-directed Raft River detachment faults, in the western and eastern ARG respectively. The Middle Mountain detachment bounds the western flank of the Albion and Grouse Creek Mountains, whereas the Raft River detachment fault encircles the Raft River Mountains (Fig. 6B). Traditional interpretations suggest these detachment faults are kinematically related to their underlying mylonitic shear zones (e.g., Wells, 2001). However, others interpret them to reflect middle Miocene normal faulting that reactivates or deforms the older mylonitic fabrics (e.g., Strickland et al., 2011; Konstantinou et al., 2012). The upper-plate rocks above the detachment faults consist of Proterozoic and Paleozoic metasedimentary rocks and Cenozoic volcanic and sedimentary deposits (e.g., Compton, 1972; Wells, 1997; Konstantinou et al., 2012). The detachment faults place unmetamorphosed middle Proterozoic-Paleozoic rocks and Miocene sediments over metamorphosed Archean-Proterozoic rocks that were deformed at temperatures of 400–500 °C (e.g., Wells, 2001) (Fig. 6B).

The relationship between detachment fault and mylonitic shear zone is consistent with scenarios h and j in Fig. 4 because of observations of (1) locally exposed windows below the Cenozoic mylonitic shear zones and (2) two shear zones of differing kinematics (i.e., the top west Middle Mountain and top-east Raft River shear zones) that may either reflect differently rooted extensional shear zones or differing flanks of a buoyant dome (Fig. 6B).

3.4. Ruby Mountains-East Humboldt Range MCC

The Ruby Mountain-East Humboldt Range (REHR) MCC (Fig. 9A) is in northeast Nevada (Fig. 5). The lower-plate core of the REHR consists of Proterozoic-Paleozoic paragneiss pervasively intruded (>2/3 by volume in most places) by deformed Late Cretaceous, Eocene, and Oligocene intrusions (Fig. 9A) (e.g., Howard et al., 2011; Snoke et al., 2024). The structurally deepest rocks are exhumed in the northern Ruby Mountains and East Humboldt Range, where rocks are migmatitic, pervasively intruded by leucogranites, and folded into large north-trending recumbent isoclinal fold nappes (e.g., Howard, 1980; Snoke, 1980; Snoke et al., 1990; MacCready et al., 1997) (Fig. 9A). *P-T-t* estimates from the lower-plate rocks suggest exhumation from depths >30 km, whereas *P-T* estimates from the mylonitic shear zone suggest exhumation from depths of ~12 km (Hurlow et al., 1991; Hodges et al., 1992; McGrew et al., 2000; Hallett and Spear, 2014, 2015; Zuza et al., 2020, Zuza et al., 2022b,c).

The East Humboldt Range is mostly composed of a ~1-km-thick sub-horizontal-to-gently-west-dipping mylonitic shear zone (Fig. 7C) with consistent WNW-trending lineations (Fig. 9A). Shear kinematics are mostly top-WNW, with the exception of structurally deep exposures in the East Humboldt Range that display top-east kinematics (McGrew and Casey, 1998; Zuza et al., 2022b). The shear zone developed in heavily intruded Proterozoic through mid-Paleozoic rocks, which are severely attenuated, suggesting >80 % vertical shortening (Fig. 8) (e.g., Zuza et al., 2022b, 2024). The voluminous Late Cretaceous-Cenozoic

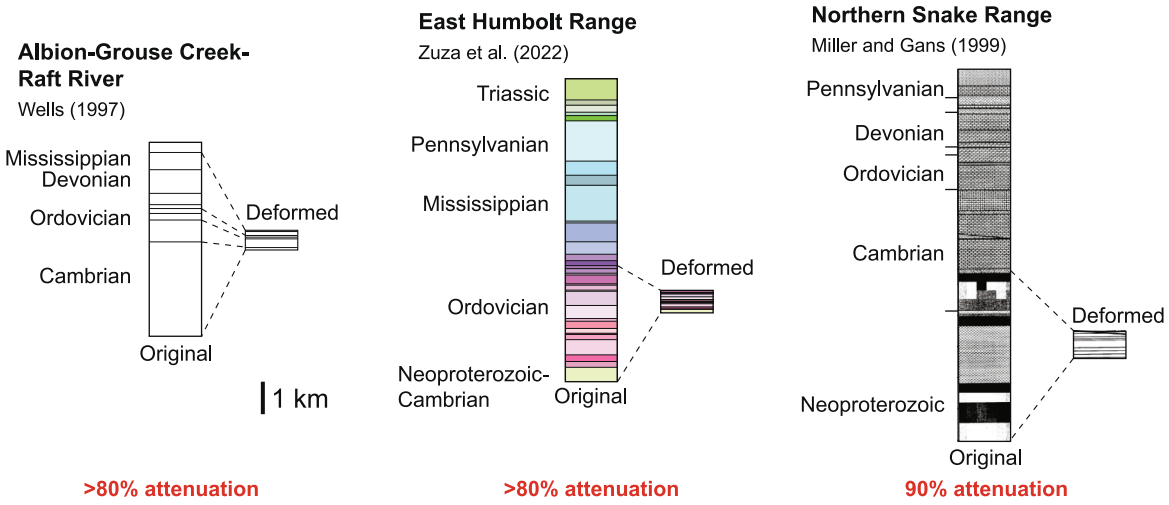

Fig. 8. Example records of attenuation in three metamorphic core complexes. In each example, the left stratigraphic column represents the stratigraphic thickness of undeformed stratigraphy and the right stratigraphic column shows the observed structural thickness of the same strata in the mylonitic lower plate. Each column is drafted in the same style and colour scheme as the original reference.

(A) Geologic map of the Ruby Mountains-East Humboldt Range

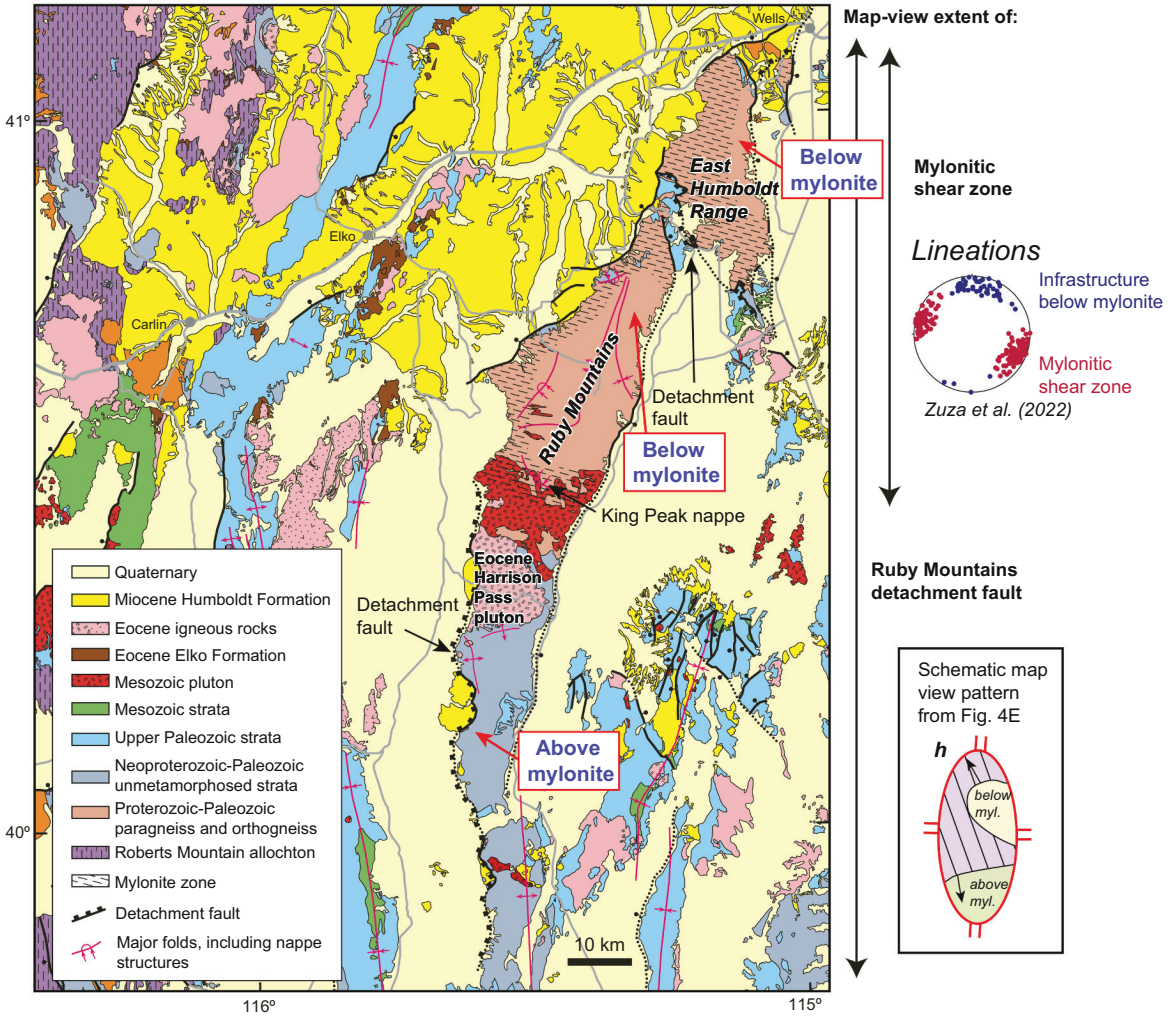

(B) Sketch of primary structures in the Whipple Mountains

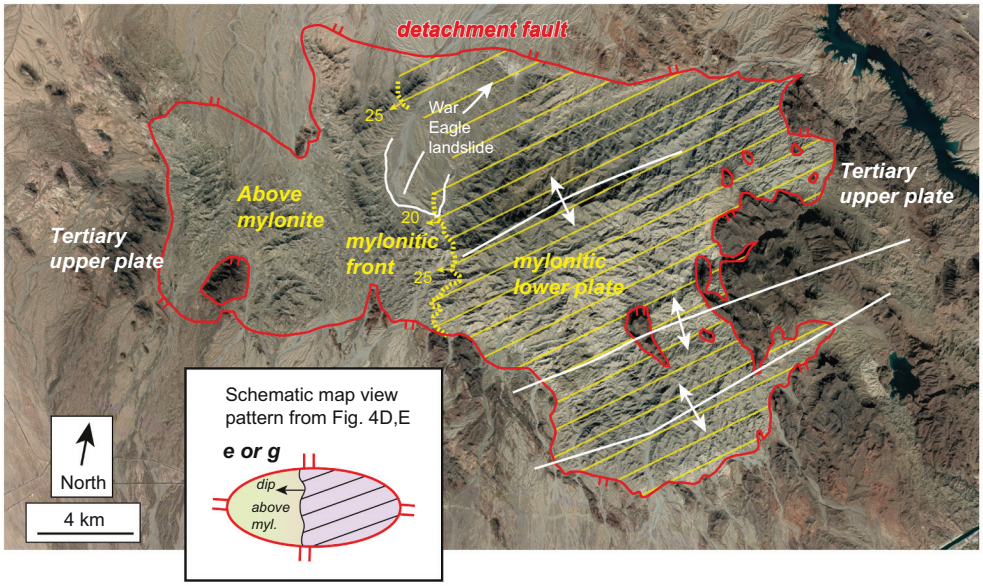

(caption on next page)

Fig. 9. Two examples of the relationships between the mapped detachment fault trace and mylonitic shear zones, including (A) the Ruby Mountain-East Humboldt Range (REHR) (map from Colgan et al., 2010) and (B) Whipple Mountains (map based on Gans and Gentry, 2016, redrafted over a Google Earth image). Insets show diagrammatic sketches of mylonite vs detachment-fault relationships, in the same style and lettering as Fig. 4A-E. In the REHR, the detachment fault is observed stretching the north-south length of the Ruby Mountains-East Humboldt Range, whereas the mylonitic shear zone is only observed in the northern half of this system. Additionally, structural relationships suggest that the rocks in the eastern East Humboldt Range are structurally below the mylonitic shear zones, whereas rocks in the central-southern Ruby Mountains are above or laterally apart from the mylonitic shear zone (e.g., Colgan et al., 2010). In the Whipple Mountains, the mapped detachment fault encircles the lower plate rocks. Mylonitic rocks are restricted to the eastern lower plate. There is a distinctive mylonitic front that dips west, which implies that the western lower plate rocks are structurally above the mylonitic shear zone (e.g., Davis, 1988).

intrusions make this attenuation estimate a minimum constraint. Late Cretaceous leucogranites represent a pronounced phase of anatexis, which was remelted during substantial Eocene-Oligocene plutonism (e.g., Howard et al., 2011; Snoke et al., 2024). Ductile fabrics from below the primary mylonitic shear zones exhibit north-trending lineations, which may have formed in the Late Cretaceous (e.g., McGrew et al., 2000) or Cenozoic (MacCready et al., 1997).

The mylonitic shear zone in the REHR has a complex geometry, potentially influenced by later tilting by middle-Miocene normal faulting, which provides important relationships for the REHR genesis. The

Fig. 10. Field photographs from the East Humboldt Range showing the strain gradient between upper plate and lower plate rocks, separated by the detachment fault (from Zuza et al., 2022b, 2024). (A) Upper plate Mississippian Diamond Peak Formation includes unstrained chert and quartzite clasts, and (B) the Pennsylvanian Ely Formation rocks show undeformed fossil corals. (C) In the lower plate, the Diamond Peak Formation shows extreme attenuation, with the chert and quartzite clasts stretched into colored laminations. Also note that there is limited stratigraphic omission with Mississippian Diamond Peak rocks above and below the detachment fault.

eastern flank of the East Humboldt Range exposes rocks below the mylonitic shear zone, which preserve top-to-the-east kinematics (McGrew and Casey, 1998; McGrew, 2018; Zuza et al., 2022b) (Figs. 7D and 9A). To the south in the central Ruby Mountains, the exposed bedrock occupies a structural position that is also beneath the mylonitic shear zone. MacCready et al. (1997) documented an important transition from WNW-stretching lineations in the mylonite to N-trending lineations below the mylonites. In this area below the mylonitic shear zone, N-trending mostly inward-facing recumbent isoclinal fold nappes are observed (i.e., the King Peak nappe) (Howard, 1980; Snoke, 1980; Snoke et al., 1990; MacCready et al., 1997) (Fig. 9A). There is a rather abrupt transition from high-grade metamorphic rocks in the northern Ruby Mountains to unmetamorphosed and unstrained Paleozoic stratigraphy in the southern Ruby Mountains (e.g., Howard et al., 1979; Colgan et al., 2010).

The upper-plate rocks of the REHR consist of middle-upper Paleozoic and Cenozoic rocks that are in detachment-fault contact with the lower-plate mylonites (Fig. 9A). Unstrained Mississippian Diamond Peak Formation and Pennsylvanian Ely Limestone are placed atop highly stretched Mississippian Diamond Peak formation in the southwest East Humboldt Range (Fig. 10) (Hurlow, 1987; Zuza et al., 2022b; Zuza and Dee, 2023). This paradoxical relationship suggests minimal stratigraphic omission across this detachment fault, despite the presence of a major strain gradient across this fault structure (Fig. 10). The map trace of the detachment fault mostly encircles the East Humboldt Range and it is cut by younger high-angle normal faults (Fig. 9A). The detachment trace extends southward to the Ruby Mountains over a distance of ~150 km (e.g., Colgan et al., 2010), and for most of this strike length, the footwall rocks are not mylonitic nor metamorphosed (Fig. 9A). The relationship between detachment fault and mylonitic shear zone is mostly consistent with scenario h in Fig. 4 because of observations of structural positions above and below the mylonitic shear zone (Fig. 9A). However, the observed top-east shear kinematics along the eastern flank of the East Humboldt Range could provide evidence for scenario j (Fig. 4).

3.5. Northern Snake Range MCC

The lower plate of the northern Snake Range MCC (Figs. 6C and 7E) consists of ductiley deformed and strongly attenuated Neoproterozoic-Cambrian quartzite, schist, and marble with Mesozoic granites and Cenozoic dikes/sills (Fig. 8) (e.g., Miller et al., 1983; Miller and Gans, 1999; Lee et al., 1987, 2017). The lower plate is less pervasively intruded by Cenozoic plutons than the ARG and REHR. These rocks were impacted by Mesozoic metamorphism and deformation, with peak *P-T* conditions of ~8 kbar and 650 °C (Lewis et al., 1999; Cooper et al., 2010) attained in the Late Cretaceous (e.g., Miller and Gans, 1989). There is ongoing discussion whether these high pressures reflect deep burial or non-lithostatic conditions (e.g. Miller et al., 1983; Hoiland et al., 2022; Zuza et al., 2022c; Long et al., 2024). In some drainages there are exposures of isoclinal recumbent folds, such as deep within Smith Creek, but these structures are generally less widespread and well exposed when compared with the REHR.

Penetrative Cenozoic ductile deformation is characterized by subhorizontal mylonitic foliations and WNW-trending stretching lineations are observed across much of the northern Snake Range (Fig. 6C). Shear kinematics are consistently top-east-southeast, although Cooper et al. (2010) documented rare top-west shear kinematics in the Marble Wash drainage of the northern Snake Range, which overprint the more pervasive top-east shear kinematics. Above the mylonitic shear zone is the brittle northern Snake Range detachment fault. Its hanging wall consists of brittlely deformed Cambrian through Permian passive margin sedimentary rocks overlain by Cenozoic volcanic and sedimentary deposits (e.g., Miller et al., 1983). The detachment encircles the lower plate rocks (Fig. 6C), including the Schell Creek and Duck Creek ranges to the west (Long et al., 2022). The western northern Snake Range footwall exposes rocks structurally above the mylonitic shear zone but below the detachment fault (e.g., Cooper et al., 2017; Wrobel et al., 2021) (Fig. 6C), which is consistent with scenario e or g in Fig. 4.

3.6. Colorado River Extension Corridor

The CREC stretches south from Las Vegas, Nevada, into eastern California and toward Phoenix, Arizona (Fig. 5). This highly extended region bounds the southwestern transition zone between the Colorado Plateau to the northeast and the Basin and Range province to the southwest (e.g., Kapp et al., 2023). Many of the foreland MCCs are located within this extensional zone and to the southeast. Here, the MCCs are more closely spaced together and show overlapping igneous and kinematics histories.

Immediately south of Las Vegas, Nevada, is a north-trending belt of back-rotated normal-fault systems (Gans and Bohrson, 1998; Faulds et al., 2001, 2002) in the CREC that are generally considered different than traditional MCCs, mostly due to the lack of a thick, lineated mylonitic shear zone. This corridor exhumes Proterozoic gneiss, Late Cretaceous two-mica granite, and mid-Miocene plutons in the footwall of major detachment faults (e.g., Faulds et al., 2001; Bachl et al., 2001; Kapp et al., 2002; Zuza et al., 2019; Zuza et al., 2022a). The CREC experienced some of the youngest onset of mid-Miocene volcanism and rapid extension in the broader belt of Cordilleran MCCs. Moving southeast across Arizona, initial volcanism and extension becomes older in age.

Just west-northwest of Parker, CA, are the Chemehuevi and Whipple Mountains MCCs (Fig. 5). The Chemehuevi MCC consists of a northeast-directed series of detachment faults that juxtapose Oligocene-Miocene volcanic and sedimentary rocks over lower plate rocks consisting of mostly Proterozoic gneiss and Cretaceous granite (e.g., Howard and John, 1987; John and Foster, 1993) (Fig. 6D). These detachment faults mostly encircle the lower plate. Cenozoic slip on these individual faults is up to ~20 km in the down-dip direction (John, 1987). The Chemehuevi MCC is interpreted to exhume primarily Cretaceous deformational fabrics associated with intra-arc magmatism and shortening (e.g., John, 1982, 1987; John and Mukasa, 1990). Cretaceous fabrics are locally overprinted by Miocene brittle and locally shear fabrics (e.g., John and Mukasa, 1990; LaForge et al., 2017). The distribution of Cretaceous versus Cenozoic fabrics is not well characterized, which makes interpretation of the structural relationship between Cenozoic shear zones and detachment faults inadequately resolved. The exposure of fabrics beneath a Cenozoic shear zone (Fig. 6D) implies a structural relationship of b, c, or i in Fig. 4.

The Whipple Mountains MCC is a classic site for the study of MCCs and detachment faults (e.g., Davis et al., 1980, 1982, 1986; Davis, 1988; Davis and Lister, 1988; Davis and Anderson, 1991) (Figs. 7F and 9B). Here, the Whipple detachment fault juxtaposes upper-plate Cenozoic volcanic rocks against lower plate rocks consisting of Proterozoic gneiss, granites, and sills, with sparse Cretaceous and Miocene intrusions (Fig. 9B). The detachment fault encircles the range, such that the middle is a window of lower-plate rocks (e.g., Gans and Gentry, 2016) (Fig. 9B). The mylonitic shear zone is thought to be thick (>1-km thick), as its base is not exposed in the high-relief core of the range. Behr and Platt (2011) documented a clear trend of higher stress mylonites at structurally higher positions, and lower stress mylonites at depth, which is consistent with a temperature dependent strength within the mylonitic shear zone. Most of this shear zone is thought to be Oligocene-Miocene in age based on deformed synkinematic sills (Wright et al., 1986; Foster and John, 1999), although there is evidence that there are older Late Cretaceous-early Cenozoic fabrics (e.g., Jaramillo et al., 2022) similar to nearby MCCs (e.g., John and Mukasa, 1990; Wong et al., 2023). Mineral stretching lineations trend northeast across the mountain range, and shear kinematics are consistently top-to-the-northeast. As previously discussed, the top of the mylonitic shear zone (i.e., the mylonitic front) is exposed in the Whipple Mountains (Davis, 1988). This geometric

observation requires that rocks to the west of the mylonitic front were located above the mylonitic shear zone but below the detachment fault. The structural configuration of the Whipple Mountain MCC is consistent with scenario e or potentially g in Fig. 4.

To the southeast of the Whipple Mountains, across the Colorado River in Arizona, are a series of northeast-trending ranges spaced at ~20 km known as the Buckskin-Rawhide (Fig. 6E), Harcuvar, and Harquahala Mountains (Fig. 5). Each of these ranges consists of a late

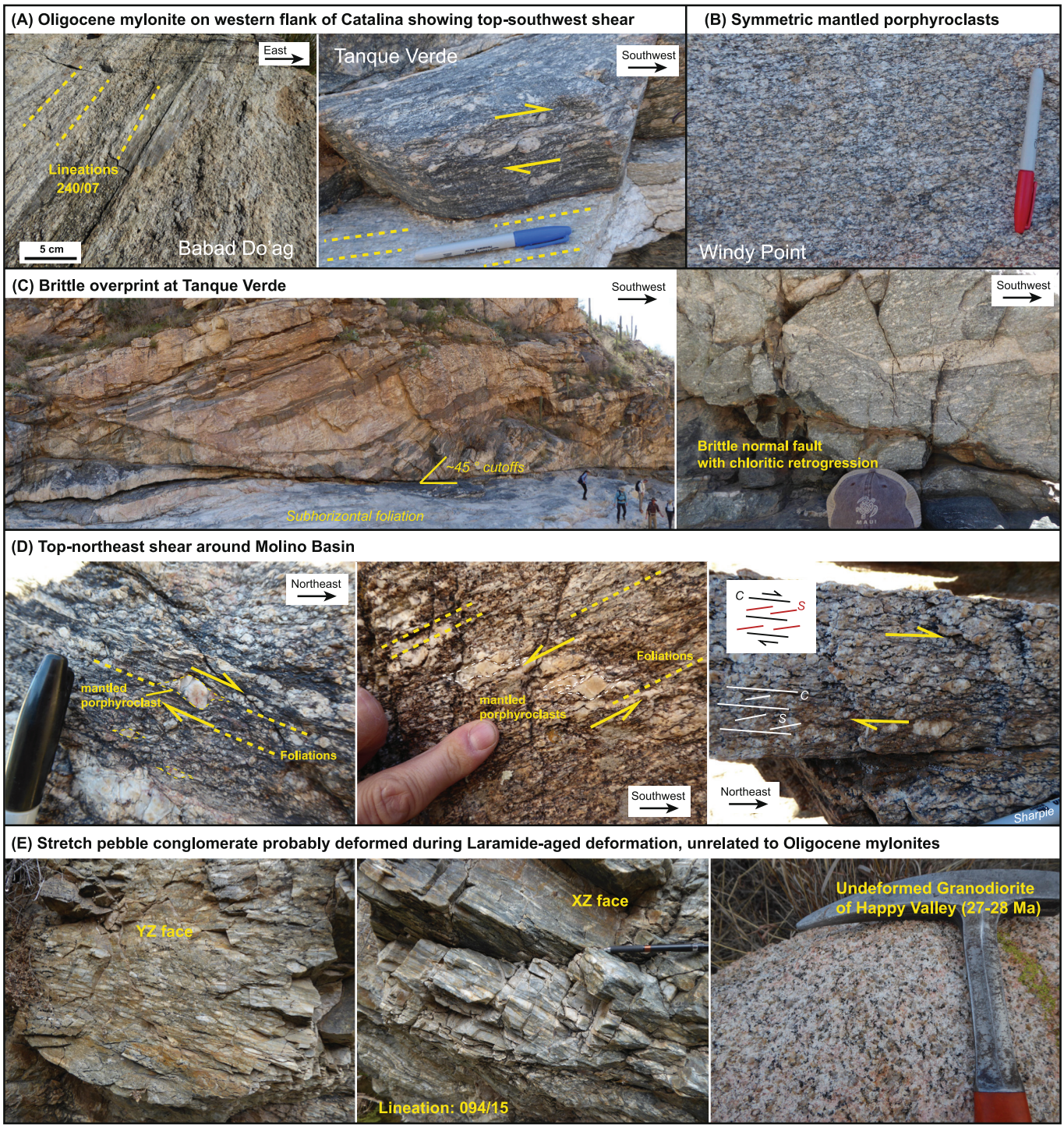

Fig. 11. Field photographs from the Catalina MCC in southeastern Arizona. (A) Strongly lineated mylonitic rocks show top-southwest kinematic indicators along much of the southwestern flank of the Catalina MCC. (B) Some parts of the shear zone are much less strongly lineated and foliated, displaying weak shear indicators. In this area, many of the mantled porphyroclasts are symmetric, but a small percentage of them reveal top-southwest shear sense, similar to the primary mylonitic shear zones as in A. (C) Exposure showing brittle normal faults overprinting and soling into the existing mylonitic shear zone. In this photograph, the mylonitic shear zones and brittle faults both display top-southwest shear sense. Rocks commonly display chlorite retrogression. (D) In some locations across the Catalina MCC, the shear sense switches to top-northeast, as documented in the Molino Basin shear zone (e.g., Spencer et al., 2022). (E) Stretched conglomerate clasts deformed in probable Laramide-aged deformation event, as evidenced by cross-cutting, undeformed Oligocene granite. Photographs from the Happy Valley area, east of the Rincon Mountains.

Oligocene-early Miocene mylonitic shear zones and brittle detachment faults that accommodate primarily northeast-directed shear (Fig. 7G). These ranges may be corrugations of the same detachment fault surface that is estimated to have accommodated ~60–70 km of northeast-directed slip (Spencer and Reynolds, 1991). The Plomosa detachment fault is a secondary detachment fault located to the southwest, and structurally beneath the Buckskin detachment (Strickland et al., 2018) (Fig. 7G). Lower plate rocks consist of Proterozoic orthogneiss and Mesozoic plutons, whereas the upper plate is predominately Paleozoic-Mesozoic metasedimentary rocks and Miocene volcanic and sedimentary rocks (e.g., Spencer and Reynolds, 1989; Singleton and Mosher, 2012).

There are two mylonitic fronts recognized in this region, which have been used to support a model of detachment-fault capture of a mid-crust shear zone (e.g., Singleton and Mosher, 2012; Singleton et al., 2022) (Fig. 7G). One mylonitic front is inferred within the Buckskin detachment-fault footwall between the Buckskin Mountains and the undeformed Bouse Hills to the southwest (e.g., Singleton and Mosher, 2012) (Fig. 6E), whereas a second is in the Plomosa detachment footwall in the Plomosa Mountains (Strickland et al., 2018). Both mylonitic fronts dip away from the northeast dip of the detachment faults (Fig. 7G). These structural geometries are consistent with scenario e and possibly scenario g in Fig. 4.

3.7. Catalina MCC

The Catalina MCC northeast of Tucson, Arizona (Fig. 5) involves an Oligocene-Miocene low-angle detachment fault that exhumed lower-plate igneous and metamorphic rocks from ~10 km depth beneath Paleozoic sedimentary and metasedimentary upper-plate rocks (Fig. 6F) (Keith et al., 1980; Davis, 1987; Dickinson, 1991; Dickinson et al., 2002; Spencer et al., 2019). The lower-plate of the Catalina MCC consists of Proterozoic schists, metasedimentary rocks, and granites which were intruded by Late Cretaceous-Early Paleogene granitoids associated with the flattened Farallon slab during the Laramide orogeny (e.g., Fornash et al., 2013; Davis et al., 2023).

Shear fabrics across the Catalina MCC are highly variable. Along the western flank of the Santa Catalina and Rincon Mountains, foliations dip southwest with down-dip lineations (Figs. 6F and 11A). Mylonitic shear zones are strongly developed with top-southwest asymmetric shear sense, such as observed at the classic Babad Go'ad (Fig. 11A) and Tanque Verde Falls localities (e.g., Davis et al., 2019). These ductile shear fabrics are cut by brittle detachment fault structures, which is well displayed within the Tanque Verde Falls canyon (Fig. 11C) (e.g., Davis, 2013). Here, there is a cataclastic overprint with chloritic retrogression (Fig. 11C). The observation that the brittle faults parallel the mylonitic fabrics suggests that mylonitic shear fabrics were favorably reactivated as a brittle fault (Davis, 2013). The Catalina detachment mostly encircles the lower plate (e.g., Davis et al., 2019) (Fig. 6F).

At some locations in the Santa Catalina Mountains at higher elevations but structurally lower positions, primarily flattening fabrics with only minor top-southwest asymmetry are observed (Fig. 11B). When compared with the southwestern flanks of the mountains, the foliation and plunge direction transition to northeast dipping and trending, respectively, near the central part of the range. In one section, shear-sense changes to top-north-northeast. This structure is called the Molino Basin shear zone (e.g., Spencer and Constenius, 2020; Spencer et al., 2022) (Figs. 6F, 7H and 11C), which has variably been interpreted as a conjugate or antithetic shear zone (Reynolds and Lister, 1990) or as a structure to accommodate upward footwall flow (Spencer et al., 2022). Bykerk-Kauffman and Janecke (1987) interpreted top-east Laramide-aged fabrics (ca. 70–50 Ma) in the core of the Santa Catalina Mountains. The opposing shear senses across the Catalina Mountains is consistent with scenario j in Fig. 4, although depending on how one reconstructs the timing and structural relationships between these various shear zones, they may reflect scenarios c or e. Differentiating these scenarios requires systematic evaluation of the interaction between these shear zones.

4. Timing of magmatism, deformation, cooling, and sedimentation within the MCC systems

4.1. Types of constraints

The dating of MCC deformation can be complicated by a complex history of polyphase deformation and magmatism. As will be outlined in Section 4.3, most MCCs experienced nearly overlapping plutonism and deformation (e.g., Gans et al., 1989; Armstrong and Ward, 1991), which makes relationships between in situ conductive cooling and exhumation equivocal. For the most part, it is well understood that most MCCs experienced prograde Jurassic-Cretaceous (−early Cenozoic) metamorphism, followed by Cenozoic retrograde *P-T* paths. However, there is still much uncertainty in the timing of the different components of the MCCs, and here we provide an updated overview of available timing constraints.

To disentangle this history, we separately synthesize the following data types:

(1) Late Cretaceous to early Cenozoic peraluminous plutonism, exposures of which spatially overlap the Cordilleran MCCs (e.g., Miller and Bradfish, 1980; Chapman et al., 2021);
(2) The broad phase of post-Laramide Cenozoic volcanic and coupled plutonic records, which tend to be pre−/syn-kinematic with respect to MCC development;
(3) Cross-cutting structural and igneous relationships;
(4) Muscovite and biotite $^{40}Ar/^{39}Ar$ ages that tracks cooling through ~400 °C to 300 °C, which thus records cooling below the temperatures of quartz crystal-plastic deformation and provides estimates for the late stages of mylonitic shearing;
(5) Low-temperature thermochronology data (<260 °C), mostly from exhumed footwall blocks, that track exhumation through the upper crust; and
(6) The facies, structural attitudes, and ages of adjacent terrestrial basins.

Within this synthesis, we construct thermal history models (QTQt; Gallagher, 2012) for several of the well constrained MCCs. The goal of these models is to allow quantitative comparisons between MCCs along strike as they cool from mid-crust conditions (~500 °C) to the surface.

4.2. Late Cretaceous to early Cenozoic peraluminous plutonism

As summarized in Miller and Bradfish (1980) and more recently in Chapman et al. (2021), there is a belt of peraluminous two-mica granites that stretches from Canada to Mexico, overlapping the belt of Cordilleran MCCs. Many of these peraluminous granites are exposed in the footwall rocks of MCCs as deformed sills, dikes, and stocks (e.g., Lee et al., 2003; Chapman et al., 2023). Ages of the granites span 92 to 42 Ma, with a general trend of younging toward the north and south (Fig. 12A). Specifically, the oldest two-mica granites are found in the REHR and Snake Range (i.e., 92–68 Ma; Lee et al., 2003; Howard et al., 2011; Hallett and Spear, 2014, 2015; Evans et al., 2015; Lee et al., 2017; Snoke et al., 2024). Ages broadly young to the north, such as 83–46 Ma granites documented in the Bitterroot-Anaconda MCCs (e.g., Foster et al., 2001, 2010; Foster and Raza, 2002; Gaschnig et al., 2010, 2011) and 57–46 Ma granites found in the Catalina MCC (e.g., Fornash et al., 2013; Fayon et al., 2000; Ducea et al., 2020) (Fig. 12A). The driver of such widespread partial melting is not clear, and likely reflects combined influence of crustal thickening, increased mantle heatflux, and a hydrated mantle lithosphere following flat-slab subduction (e.g., Houseman et al., 1981; Thompson and Connolly, 1995; Jödicke et al., 2006; Chapman et al., 2021; Segee-Wright et al., 2023). For a more

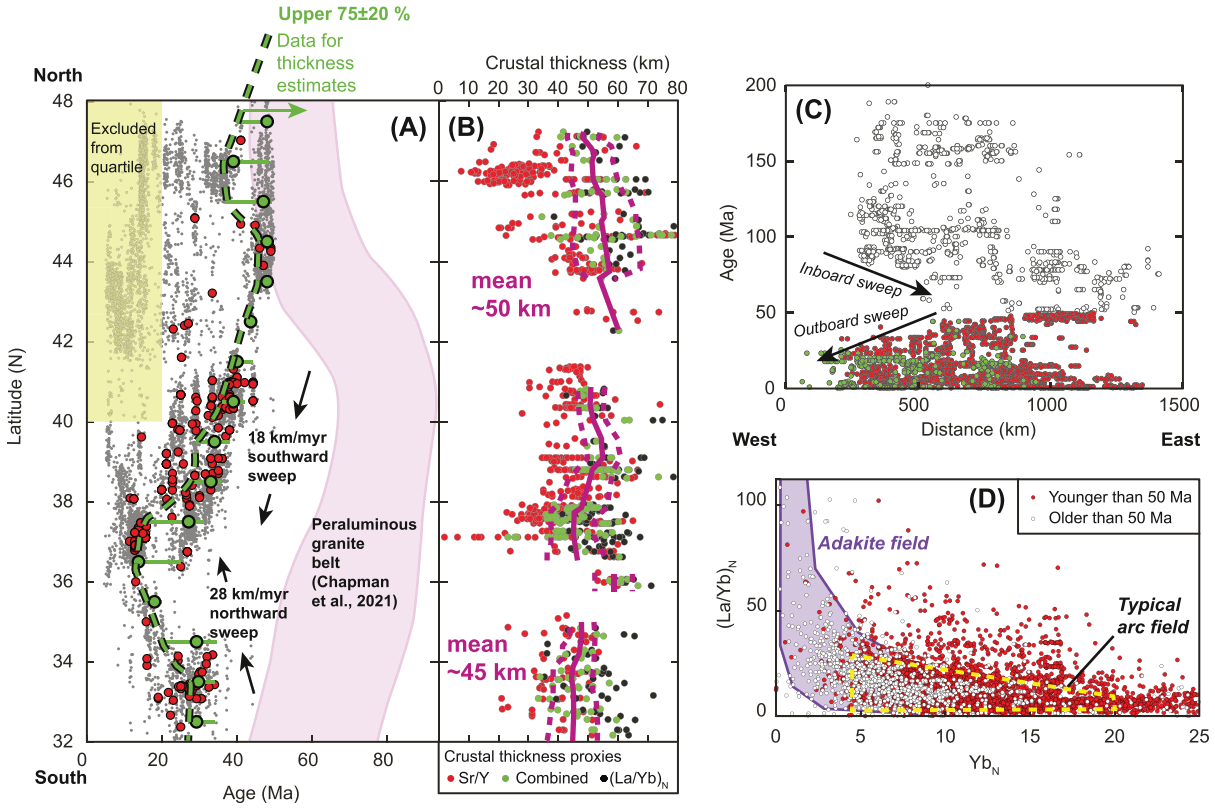

Fig. 12. NAVDAT geochemical data plotted from the North American Cordillera. (A) Plot of age versus latitude for data showing the inward sweep of Farallon slab-rollback volcanism. Only ages <50 Ma were plotted. Red symbols plot potassic rocks. The oldest quartile was calculated for 1° latitude bins (green symbols), which show the overall trends of initial volcanism. Also plotted is the peraluminous granite belt after Chapman et al. (2021). (B) Plot of estimated crustal thickness versus latitude at the time of initial rollback volcanism (only upper quartile data from A), using different trace-element proxies (Sundell et al., 2021). The data broadly shows a similar average crustal thickness of 45–50 km along the north-south strike length of the Cordillera. (C) Plot of age versus west-east distance highlight the eastward and west sweeps in volcanism associated with the flattening and steepening of the Farallon slab. Black points are data >50 Ma projected onto a west-east profile, red points are data <50 Ma in the northern latitudes of the study area projected onto a NE-oriented profile, and green points are data <50 Ma in the southern latitudes projected onto an ENE-oriented profile (see Fig. 5 for profiles). The data <50 Ma was variably projected onto these two profiles due to interpreted differences in how the Farallon slab rolled back (e.g., Humphreys, 1995). (D) Plot showing the more adakitic character of the >50 Ma volcanic rocks compared to the <50 Ma volcanic rocks. Plot from Defant and Drummond (1990). (For interpretation of the references to colour in this figure legend, the reader is referred to the web version of this article.)

complete discussion of this peraluminous belt, we refer the reader to Chapman et al. (2021).

4.3. Pre- and post-Laramide Cenozoic magmatic sweep

Starting ca. 80 Ma, the east-dipping Farallon slab began to flatten, effectively shutting off magmatism along the western margin of North America (e.g., Liu and Currie, 2016; Copeland et al., 2017). This flattening is hypothesized to drive deformation far east into the North American interior as part of the Laramide orogeny (e.g., Bird, 1988; Yonkee and Weil, 2015). Subsequent rollback or slab foundering led to widespread volcanic activity across the western Cordillera. There are obvious age trends with this volcanism that have been used to interpret slab rollback and potential slab tears (e.g., Armstrong and Ward, 1991; Humphreys, 1995; Copeland et al., 2017). In the north, magmatism youngs to the southwest from Idaho latitudes toward southern Nevada, whereas in the south, magmatism youngs to the west-northwest from Sonora to southern Nevada-northern Arizona (Fig. 2B). Rollback magmatism is not obviously associated with regional extension in the backarc as might be expected (e.g., Xu et al., 2021), which is evidenced by Eocene-Oligocene tuffs and lake deposits across Nevada that were not deformed prior to the Miocene (e.g., Smith et al., 2017; Lundstern et al., 2024). In particular, the widespread occurrence of relatively thin Eocene basins across the Cordillera hinterland has been interpreted in the context of dynamic subsidence following slab rollback (Cassel et al., 2018) and/or slab eclogitization and foundering (Li, 2015).

Age and geochemical trends for Mesozoic-Cenozoic magmatism can be compared against the MCC history and precursor tectonics events, such as slab shallowing and rollback. We compiled Mesozoic-Cenozoic igneous data from the NAVDAT database (navdat.org), supplemented with additional data from Arizona from Jepson et al. (2022). Laramide slab flattening is interpreted to have proceeded from west to east, whereas rollback appears to have propagated SW in the north, and WNW in the south, possibly associated with complex slab detachment, tearing, and rollback (e.g., Humphreys, 1995). Therefore, we projected the >50 Ma NAVDAT data onto a west-east profile (black points on Fig. 12C), whereas the <50 Ma data was split: the northern data was projected onto a NE-oriented profile (red points on Fig. 12C) and the southern data was projected on an ESE-oriented profile (green points on Fig. 12C). These variably oriented profiles are shown in Fig. 5. This plot shows the pronounced Late Cretaceous eastward/inboard sweep of magmatism during the flattening of the Farallon slab and cessation of magmatism around the Sierra Nevada longitudes, followed by the early Cenozoic westward sweep that accommodated slab rollback and/or foundering (e.g., Gans et al., 1989; Armstrong and Ward, 1991; Humphreys, 1995; Copeland et al., 2017) (Fig. 12C). The Laramide-aged inboard sweep generated igneous rocks with a more adakitic character (elevated $[La/Yb]_N$ relative to Yb_N; e.g., Defant and Drummond, 1990) than those generated during the westward/outboard sweep (Fig. 12D). Adakites are generally thought to reflect melting of a garnet-bearing thickened lower

crust or even oceanic lithosphere (e.g., Defant and Drummond, 1990; Moyen, 2009). This may suggest that high-pressure, deep melting was common during the shallowing phase Farallon subduction as the hydrated oceanic slab interacted with the thickened Cordillera continental lithosphere. Similar patterns have been observed for the flat-slab subduction process in the western Pacific across eastern Asia (e.g., F. Wu et al., 2019; J. Wu et al., 2022).

A plot of mid-late Cenozoic igneous ages versus latitude shows the broad patterns of silicious Farallon slab rollback associated magmatism. Ages north of latitude 36°N show a southward younging trend of initial magmatism from ca. 45 Ma in the north to ca. 20 Ma in the south (Fig. 12A). Ages south of latitude 36°N show the opposite: northward younging trend of initial magmatism from ca. 35 Ma in the south to ca. 15 Ma in the north. Potassic rocks ($K_2O/Na_2O > 3$) overlap this initial sweep, consistent with high-temperature melting of an enriched mantle source (e.g., Manley et al., 2000).

To quantitatively isolate the magmatism associated with slab rollback, which may have been related with the generation of MCCs (e.g., Gans et al., 1989), we calculated the oldest 75 ± 20 % range of Cenozoic magmatism at binned-latitudes of 1° with 0.25°overlap. The justification of this approach is that we aimed to capture the initial phase of magmatism associated with rollback. We first removed volcanism associated with the Yellowstone hotspot track (Fig. 12A), which contributed a large amount of Miocene datapoints that skewed the percentile calculation. If there is a spread of ages throughout the Cenozoic, our approach isolates the phase associated with rollback. In 1° latitude bins with little data, our approach still captures the earliest phase of rollback magmatism. Visually, this approach satisfactorily demarcates the pulse of magmatism associated with rollback magmatism (Fig. 12A) (e.g., Coney and Reynolds, 1977; Copeland et al., 2017). Through this method we estimate that northern magmatism youngs southward at a rate of ~18 km/Myr, whereas the southern magmatism youngs northward at a rate of ~28 km/Myr (Fig. 12A).

We employed whole-rock geochemical "Mohometry" methods (Luffi and Ducea, 2022), which is based on the idea that crustal thickness may correlate with certain trace-element parameters, using the calibration of Sundell et al. (2021) to estimate the crustal thickness across the Cordillera at the time of the roll-back magmatism. Data was filtered to include only space-time points consistent with rollback magmatism to isolate conditions at a fixed part of the tectonic history, and intermediate geochemical conditions outlined in Profeta et al. (2015) and Luffi and Ducea (2022) (i.e., 55–68 % SiO_2, 0–4 % MgO, and 0.05–0.2 % Rb/Sr). We plotted Sr/Y, $(La/Yb)_N$, and coupled Sr/Y-$(La/Yb)_N$ crustal thickness estimates using the calibration of Sundell et al. (2021). The data broadly overlap over the 40–60 km thickness range for all latitudes. A moving average for the coupled Sr/Y-$(La/Yb)_N$ crustal thickness data results show a broadly flat signal where the pre-Miocene crustal thickness was ~45–50 km thick across the north-south length of Cordillera (Fig. 12B). In detail, the north and central regions have an average thickness of ~50 km, whereas the southern region has an average thickness of ~45 km.

In summary, compiled geochemical data tracks Farallon slab shallowing and rollback from ca. 80 to 20 Ma. The initial shallowing phase has a more adakitic character (higher La/Yb ratios) than the rollback phase, which may reflect enhanced subduction erosion and mantle flow to drive higher pressure melting during slab shallowing. The magmatism data shows the early Cenozoic rollback phase of magmatism that preceded MCC development. Quantitative crustal thickness estimates show moderate thickness across the Cordillera (~50 km) at the time of rollback.

4.4. Thermochronology and cross-cutting relationships

Medium-temperature $^{40}Ar/^{39}Ar$ thermochronology of primarily muscovite and biotite tracks cooling through mid-crust conditions (600–250 °C). The closure temperature of Ar diffusion in muscovite is ~400 °C (Harrison et al., 2009) and in biotite is ~300 °C (Harrison et al., 1985). Therefore, these muscovite and biotite $^{40}Ar/^{39}Ar$ dates may provide a proxy for the most recent stages of mylonitic shearing as the temperature range of these systems brackets the lower range of quartz plasticity (e.g., Sibson, 1977; Stipp et al., 2002). Once the rocks cooled below biotite closure temperatures (~300 °C), the rocks would presumably deform via brittle/friction mechanisms. Many of the MCC mylonites formed at temperatures exceeding 300–400 °C (e.g., Behr and Platt, 2011; Gottardi et al., 2020; Levy et al., 2023), and therefore $^{40}Ar/^{39}Ar$ mica ages track when the MCC rocks cooled below mylonite-generating temperatures.

Low-temperature thermochronology (<250 °C) tracks cooling and exhumation of the upper crust, which can be interpreted to track exhumation associated with brittle faulting or other surface processes. Compiled analyses are zircon fission track (ZFT), zircon (U-Th)/He (ZHe), apatite fission track (AFT), and apatite (U-Th)/He (AHe), which have respective closure temperatures of 210–270 °C (Zaun and Wagner, 1985; Hurford, 1986; Brandon et al., 1998; Bernet and Garver, 2005), 180–200 °C (Reiners et al., 2002, 2004; Wolfe and Stockli, 2010), 60–120 °C (Ketcham et al., 2007), and 55–75 °C (Wolf et al., 1996; Farley, 2000; Flowers et al., 2009). Based on typical geothermal gradients (~20–40 °C/km; Łuszczak et al., 2017), these analyses track cooling through the upper ~10 km of the crust.

4.4.1. Bitterroot and Anaconda MCCs

Mylonitic shearing in the Bitterroot MCC deforms ca. 53–52 Ma granite, and $^{40}Ar/^{39}Ar$ and U-Pb dating suggest that most of the deformation occurred between 50 and 45 Ma (Foster and Mark Fanning, 1997; Foster and Raza, 2002), consistent with *P-T-t* studies that suggest cooling of the mylonite zone to <300 °C from ca. 50 to 40 Ma (e.g., Garmezy, 1983; LaTour and Barnett, 1987; Hyndman and Myers, 1988; Doughty and Sheriff, 1992; House and Hodges, 1994; Foster and Mark Fanning, 1997; Foster et al., 2001). AFT and ZFT traverses across the Bitterroot MCC show temporally and spatially variable cooling. The western part of the Bitterroot Mountains cooled below ~200 °C by ca. 45 Ma, whereas the eastern part experienced later cooling ca. 35–25 Ma (Foster and Raza, 2002). Vertical traverses from this same study show rapid cooling ca. 35–30 Ma (Foster and Raza, 2002).

The hanging wall of the Anaconda MCC involves the 54–58 Ma Lowland Creek volcanics, and the pre−/syn-kinematic 53–45 Ma Challis-Kamloops alkalic intrusions were involved in mylonitic shear zone (e.g., Foster et al., 2010; Howlett et al., 2021). Eocene $^{40}Ar/^{39}Ar$ muscovite and biotite dates further support MCC shearing and exhumation at this time (Foster et al., 2010). Low-temperature thermochronology data is sparser. ZHe ages broadly span 40 to 25 Ma (Howlett et al., 2021). Foster et al. (2010) presented AFT dates, with one sample yielding a ca. 44 Ma age and four samples spatially closer to the detachment fault spanning ca. 27–25 Ma.

4.4.2. Pioneer MCC

In the Pioneer MCC, hornblende and mica $^{40}Ar/^{39}Ar$ dates track 45 to 35 Ma cooling (Silverberg, 1990; Vogl et al., 2012) after the intrusion of the ductilely sheared ca. 49 Ma Pioneer Intrusive Suite. The mylonitic shear zone deforms a ca. 47 Ma dike and is cross-cut by an undeformed-to-minimally deformed ca. 46 Ma dike suggesting that strain may have slowed or ceased by this time (Vogl et al., 2012). However, $^{40}Ar/^{39}Ar$ dates suggest mid-crust cooling continued until ca. 35 Ma (Fig. 5).

An AHe traverse across the Pioneer MCC yields 11–8 Ma ages that correlate with elevation (Vogl et al., 2014). This data suggests rapid cooling from ca. 11 Ma to 8 Ma. West of the Pioneer MCC, Fayon et al. (2017) conducted a systematic ZHe study across the Idaho batholith. This study obtained numerous Late Cretaceous to early-mid Cenozoic ages, which were mostly interpreted to have resulted from conductive cooling of the Late Cretaceous Idaho batholith with possible Eocene Challis reheating and minimal exhumation. Anomalously young 30–20 Ma ZHe ages in the Sawtooth Mountains may reflect a phase of focused

exhumation and possible normal faulting (Fayon et al., 2017).

4.4.3. Albion-Raft River-Grouse Creek MCC

The ARG MCC experienced a complex, spatially varying thermal history. The top-west Middle Mountain shear zone (Fig. 6B) in the western ARG has previously been interpreted to accommodate extensional shearing in the Middle-Late Eocene based on $^{40}Ar/^{39}Ar$ dates (e.g., Wells et al., 2000; Wells, 2001). However, others have suggested that peak metamorphism and ductile shearing was associated with the intrusion of ca. 32–25 Ma plutons (Egger et al., 2003; Strickland et al., 2011). The country rock surrounding the Oligocene plutons shows extreme attenuation and high-grade metamorphism that may be related to the emplacement of the plutons, or could instead reflect exhumation of the coupled ARG MCC system (Todd, 1980; Egger et al., 2003;

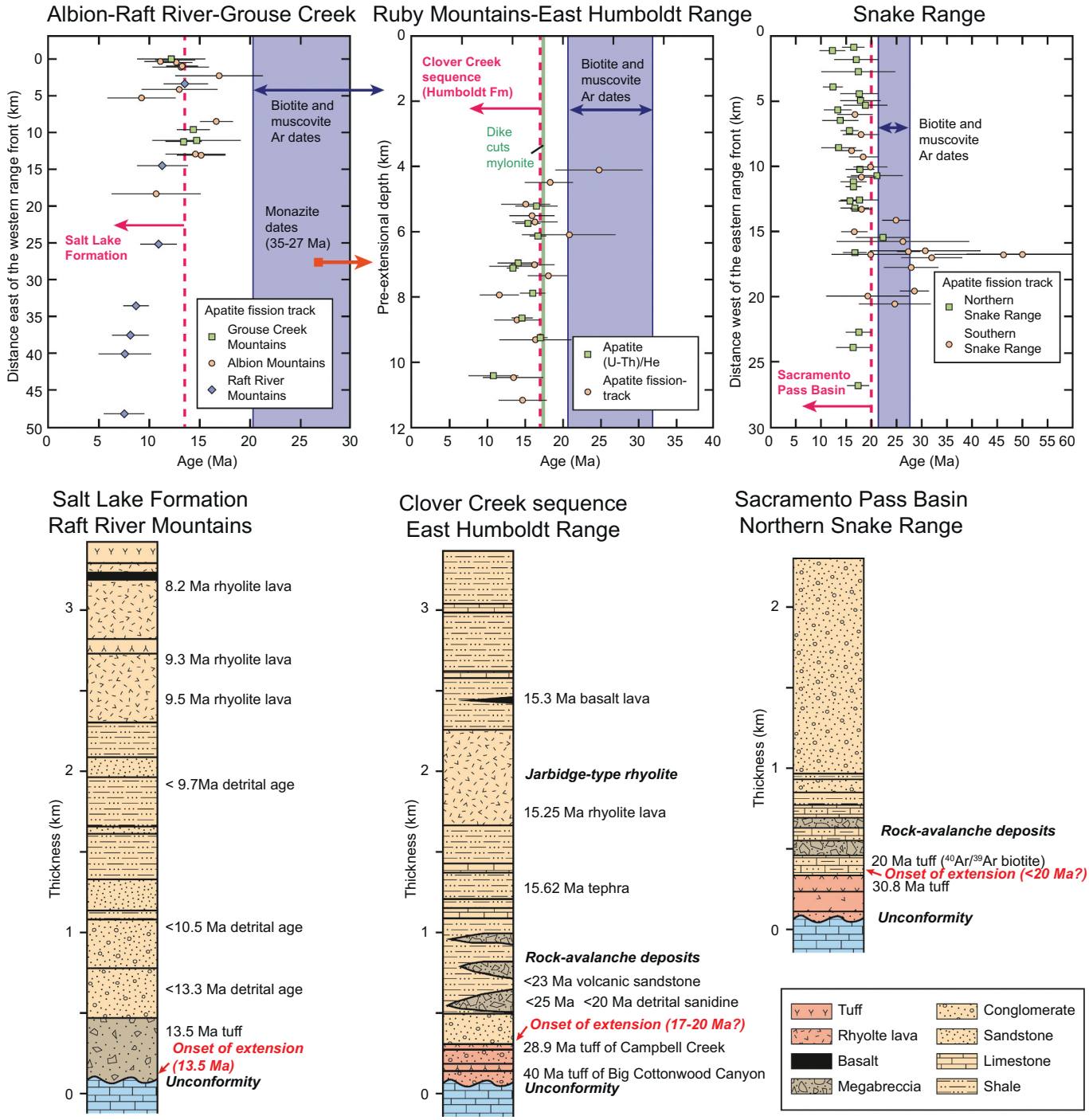

Fig. 13. Compilation of low-temperature thermochronology traverses across select hinterland metamorphic core complexes and stratigraphic columns of Miocene stratigraphy that is interpreted to be syn-kinematic with respect to middle Miocene Basin and Range extension in the region. Marked in red on each stratigraphic column is the stratigraphic position and approximate age of the initiation of extension, which is drafted as a dashed red line of the related thermochronology transects. Thermochronology sources: Egger et al. (2003) (Grouse Creek Mountains); Egger et al. (2003) (Albion Mountains); Wells et al. (2000) (Raft River Mountains); Colgan et al. (2010) (Ruby Mountains); Miller et al. (1999) (Snake Range). Stratigraphy sources: Konstantinou et al. (2012) (Raft River Mountains); Zuza et al. (2021) and Zuza and Dee (2023) (East Humboldt Range); Ruksznis (2015) (Northern Snake Range). (For interpretation of the references to colour in this figure legend, the reader is referred to the web version of this article.)

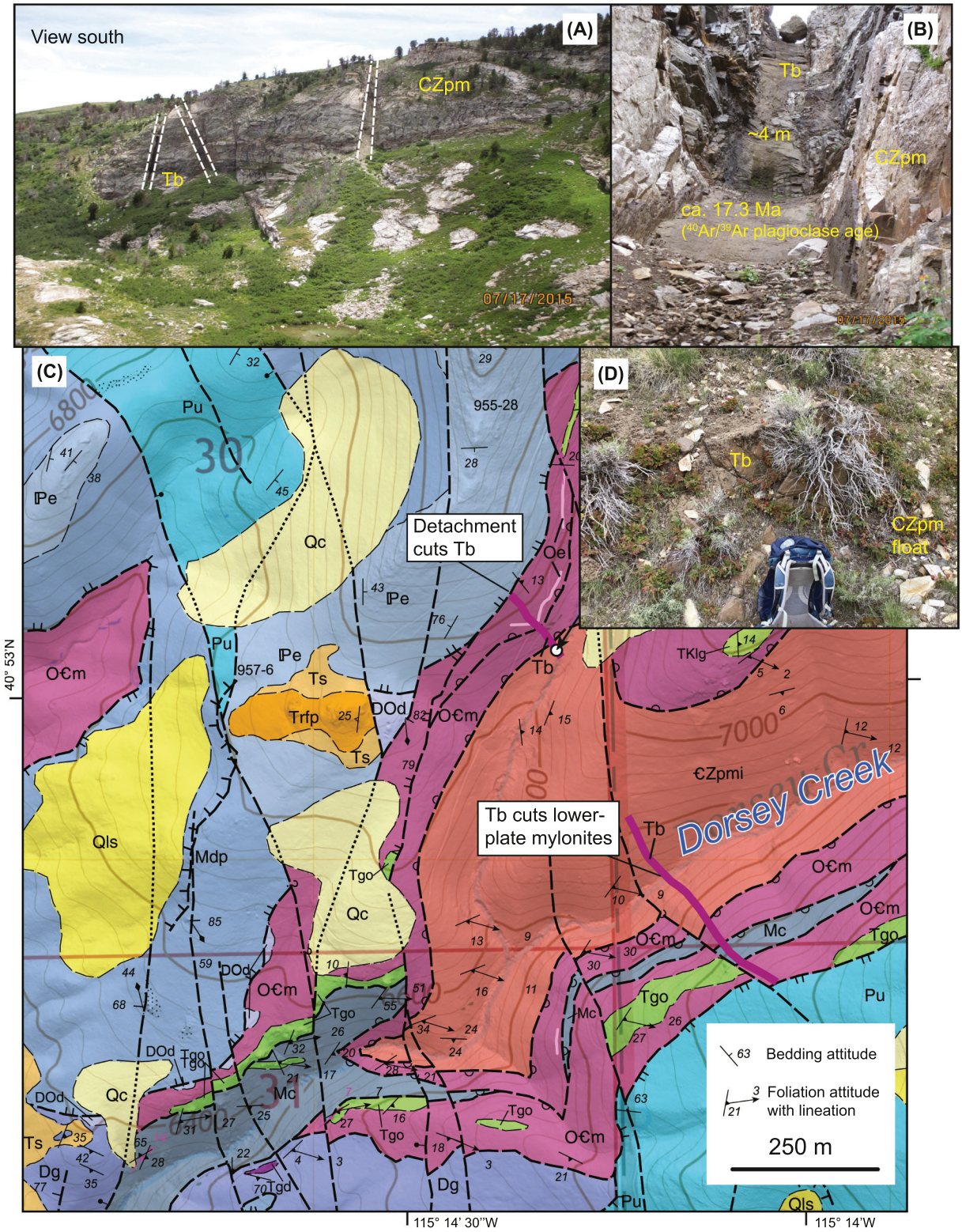

Fig. 14. Cross-cutting time relationships from the East Humboldt Range. (A) The mylonitic shear zone is cut by undeformed subvertical basalt dikes (B), which were dated to ca. 17.3 Ma. The same basalt dikes are cut by the detachment fault, as viewed in (C) geologic mapping from the southwestern East Humboldt Range (Snoke, 1980; Zuza et al., 2021) (Map units in E). (D) Field photograph of the poorly exposed basalt outcrop that intrudes the mylonitic lower plate and is cut by the overlying detachment fault. A sample from this outcrop was dated at ca. 16.9 Ma via matrix $^{40}Ar/^{39}Ar$ dating (Zuza et al., 2022b; Zuza and Dee, 2023). (E) Geologic units in the map in C.

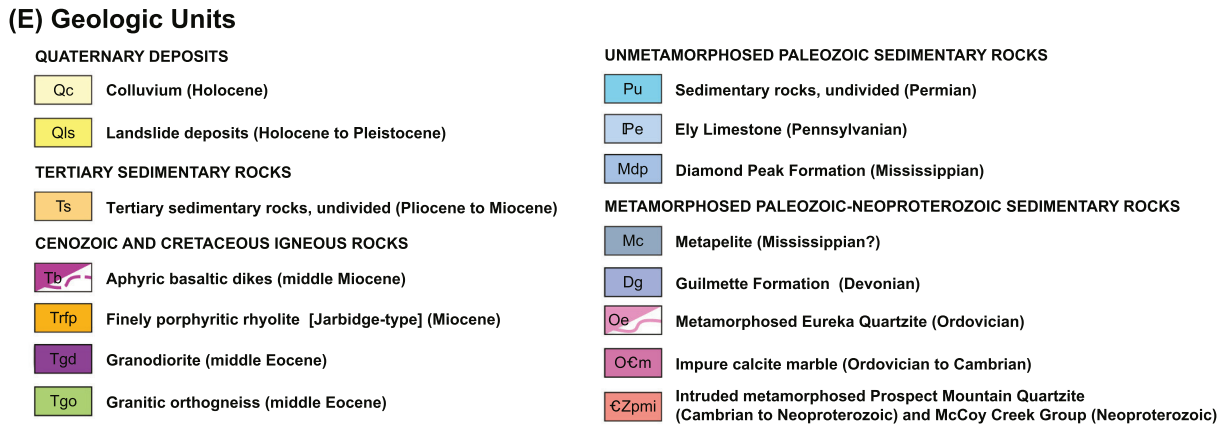

Fig. 14. (*continued*).

Strickland et al., 2011). As an example, high-strain fabrics are spatially associated with the ca. 28 Ma Vipont pluton, and monazite from metamorphic rocks and boudinaged pegmatite yield Th-Pb ages spanning 32 to 27 Ma (Strickland et al., 2011) (Fig. 6B). The top-east Raft River mylonitic shear zone (Fig. 6B) has been interpreted to have been active in the Late Oligocene-early Miocene based on $^{40}Ar/^{39}Ar$ muscovite and biotite dates (e.g., Wells, 1997, 2001; Wells et al., 2000; Gottardi et al., 2015).

There are AFT traverses across the three primary mountain ranges in the ARG. Wells et al. (2000) analyzed samples from the Raft River Mountains and Egger et al. (2003) provided AFT dates from the Grouse Creek and Albion Mountains. All AFT dates are Miocene, and a prominent cluster of ca. 13.4 Ma ages near the range fronts of all the datasets suggests the initiation of significant exhumation at this time (Fig. 13).

4.4.4. Ruby Mountains-East Humboldt Range MCC

Late Cretaceous-Eocene hornblende $^{40}Ar/^{39}Ar$ dates across the REHR track high-temperature cooling during pulses of Late Cretaceous peraluminous plutonism and juvenile Eocene quartz diorite intrusion (e.g., McGrew and Snee, 1994; Zuza et al., 2022b). Oligocene (ca. 31–29 Ma) monzogranite intrusions are deformed by the mylonitic shear zone in the REHR, but at structurally deeper positions remain undeformed, thus demonstrating the syn-kinematic nature of these intrusions (Zuza et al., 2022b). Alternatively, Cooper et al. (2017) interpreted that the undeformed Oligocene granites crosscut older fabrics in the core of the MCC, but get deformed by younger mylonites at structurally higher levels. Of note, MacCready et al. (1997) documented north-trending lineations in Oligocene granites found in the infrastructure core of the Ruby Mountains. Because of the general observation that north-trending lineations are overprinted by WNW-trending lineations associated with the primary mylonitic shear zone of the MCC (e.g., MacCready et al., 1997; Snoke et al., 2024), these observations together suggest ductile deformation and deep flow in the infrastructure was occurring during the Oligocene. This provides a constraint on the age of structurally deep fabrics, which likely involved Late Cretaceous and Eocene-Oligocene deformation.

Subsequent cooling is tracked by 25–23 Ma biotite and muscovite $^{40}Ar/^{39}Ar$ and ZFT dates (Wright and Snoke, 1993). The mylonitic shear zone is crosscut by ca. 17 Ma undeformed, subvertical basalt dikes with chilled margins that require the shear zone to be cold and inactive by the middle Miocene (Figs. 14A,B; Snoke, 1980; Zuza et al., 2021, Zuza et al., 2022b). The same basalt dikes are cut by the detachment faults, suggesting post-17 Ma detachment-fault slip (Figs. 14C,D). The contemporaneous basin history around the REHR is discussed in the next section, but a ~ 3-km thick package of middle Miocene sedimentary and volcanic rocks consisting of ca. 15.3 Ma rhyolite lava observed in the northeast East Humboldt Range is in the hanging wall of the detachment fault, which suggests slip continued after ca. 15.3 Ma. Haines and van der Pluijm (2010) presented $^{40}Ar/^{39}Ar$ fault-gouge ages from the Ruby Mountain-East Humboldt Range detachment fault exposed on the southern flank of the East Humboldt Range, which suggest detachment slip activity at 13–11 Ma.

The most comprehensive low-temperature thermochronology traverse from the REHR comes from the central Ruby Mountains. Colgan et al. (2010) provided AFT and AHe analyses from across the Eocene Harrison Pass pluton (Fig. 9A), which yielded almost exclusively Miocene dates (Fig. 13). Most ages were ca. 16–17 Ma over the sampled paleo-pre-extensional depth range (~5-11 km paleodepths according to Colgan et al., 2010), and are interpreted as range exhumation and normal faulting initiating ca. 17 Ma in the Ruby Mountains.

4.4.5. Northern Snake Range MCC

In the Snake Range, cross-cutting deformed and undeformed rhyolite dikes bracket mylonitic shearing between ca. 37.8 and 22.5 Ma (Lee et al., 2017). This history is consistent with mostly ca. 25 Ma biotite and muscovite $^{40}Ar/^{39}Ar$ ages (Lee and Sutter, 1991; Gébelin et al., 2011, 2015). No igneous rocks cut the detachment fault, but Miocene sedimentary and volcanic rocks in the hanging wall have maximum depositional ages (MDAs) younger than ca. 20 Ma, which implies detachment slip after ca. 20 Ma.

Miller et al. (1999) provided AFT dates from across the northern and southern Snake Range. Most AFT dates are Miocene, and the overwhelming majority of ages were ca. 17 Ma, which was interpreted to suggest exhumation of the MCC edifice and Basin and Range normal faulting initiated at this time (Fig. 13). The small group of older Eocene-Oligocene AFT ages were obtained from structurally shallower positions and were thus interpreted to reflect the exhumation of a partial annealing zone (Miller et al., 1999).

4.4.6. Colorado River Extensional Corridor

South of Las Vegas in the Eldorado Mountains, there is a northward younging trend of magmatism and extension from ca. 17 Ma to 15 Ma tracked by tilt-fanned volcanic rocks, paleomagnetic data, tilted dikes, and thermochronology (Gans and Bohrson, 1998; Faulds et al., 2001, 2002; Zuza et al., 2019; Zuza et al., 2022a). Zuza et al. (2022a) presented three ZHe traverses across Miocene plutons, which yielded middle Miocene ages (ca. 12 to 16 Ma), consistent with rapid exhumation at ca. 16 Ma, shortly after plutonism (Zuza et al., 2019). Just to the southwest, Mahan et al. (2009) provided AHe dates from the southern McCullough Range that shows mostly middle Miocene ages, with structurally highest samples yielding early-middle Cenozoic dates (Fig. 15). A prominent break-in-slope on age versus paleo-depth plots suggests the initiation of tectonic exhumation at ca. 16 Ma (Fig. 15).

To the south, in the Chemehuevi Mountains, much of the lower plate

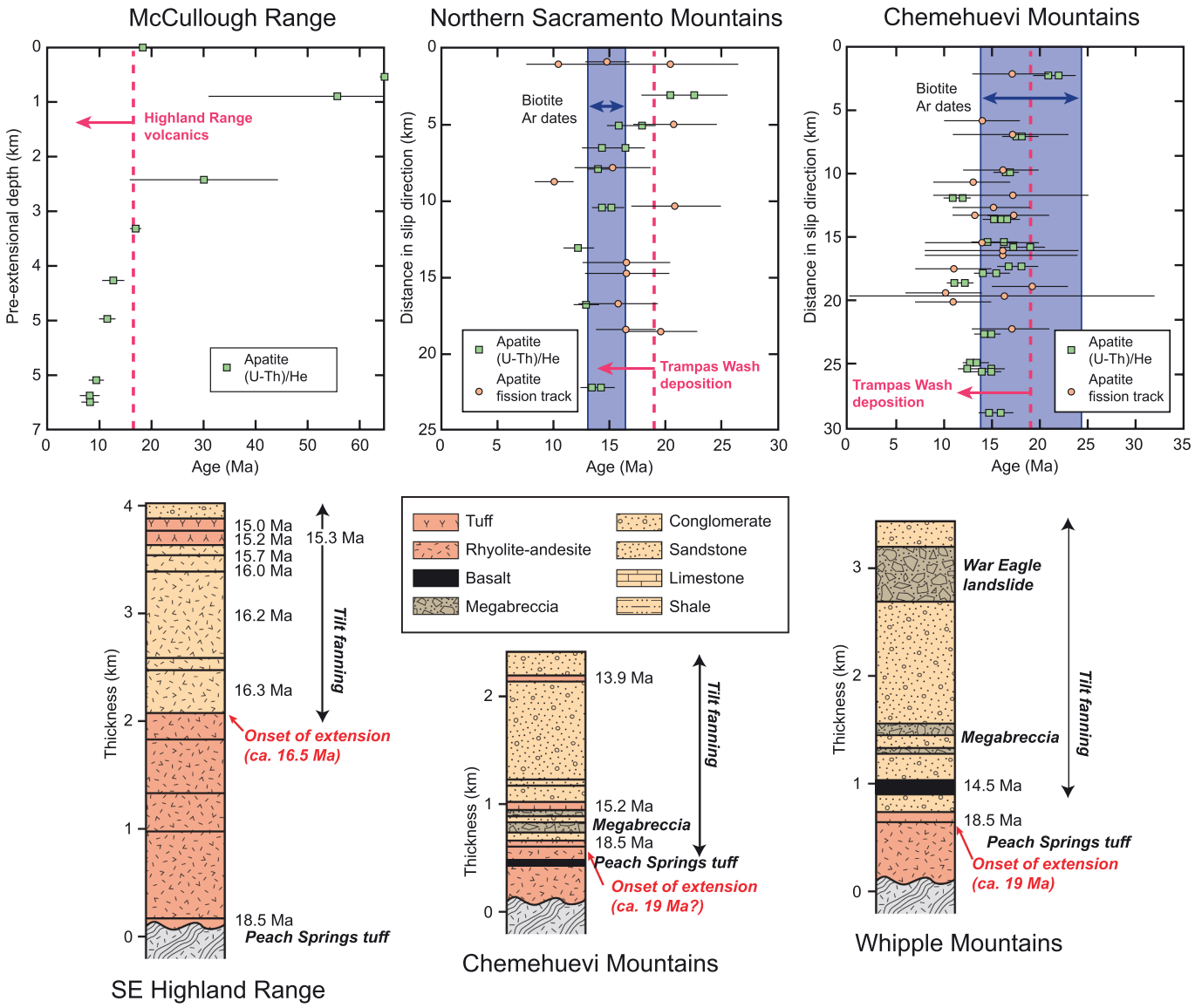

Fig. 15. Compilation of low-temperature thermochronology traverses across select south foreland metamorphic core complexes and stratigraphic columns of Oligocene-Miocene stratigraphy. Marked in red on each stratigraphic column is the stratigraphic position and approximate age of the initiation of extension, which is drafted as a dashed orange line of the related thermochronology transects. Thermochronology sources: Mahan et al. (2009) (McCullough Range); Pease et al. (1999) and Carter et al. (2006) (Northern Sacramento Mountains and Chemehuevi Mountains); Singleton et al. (2014) (Buckskin-Rawhide); Prior et al. (2016) (Harquahala); Jepson et al. (2022) (Catalina). Stratigraphy sources: Faulds et al. (2002) (Southeast Highland Range); Miller and John, 1999 (Chemehuevi Mountains); Yin and Dunn (1992) and Dorsey and Becker (1995) (Whipple Mountains); Prior et al. (2018) (Buckskin-Rawhide); Spencer et al. (2018) (Plomosa Mountains); Spencer et al. (2021) (Catalina). (For interpretation of the references to colour in this figure legend, the reader is referred to the web version of this article.)

has been interpreted to consist of Late Cretaceous-Paleogene shear fabrics (John and Mukasa, 1990) that were reactivated by local Miocene detachment faults and associated shear fabrics. Recent U-Pb dating of deformed apatite suggests the presence of discrete Late Cretaceous-Paleogene and Miocene shear zones (Lee et al., 2024; Sihpol et al., 2024), but more systematic petrochronology is required. Biotite $^{40}Ar/^{39}Ar$ dates from the Chemhuevi MCC display ages spanning ca. 22 to 17 Ma, with a younging trend toward the northeast (Foster et al., 1990; John and Foster, 1993; Foster and John, 1999). AHe and AFT results from the Chemehuevi Mountains and adjacent Northern Sacramento Mountains yield a swath of 20–15 Ma ages across a range of structural positions, which broadly overlap the biotite $^{40}Ar/^{39}Ar$ dates (Fig. 15) (Pease et al., 1999; Carter et al., 2006). These results suggest rapid exhumation at this time accommodated via detachment-fault slip. The detachment faults were crosscut by undeformed 11.6 Ma dikes (John, 1987).

In the Whipple Mountains, Gans and Gentry (2016) conducted U-Pb and $^{40}Ar/^{39}Ar$ dating to bracket the timing of mylonitic shear versus brittle fault slip. Specifically, a mylonitized dacite dike with a ca. 20 Ma U-Pb zircon age and undeformed ca. 18.8 Ma dikes bracket shearing to have commenced before or by ca. 20 Ma and ceased by ca. 19 Ma. These absolute cross-cutting constraints are consistent with ca. 20–18 Ma biotite $^{40}Ar/^{39}Ar$ dates from the footwall rocks (Foster and John, 1999). Tilt fanning of 19.0–18.5 Ma volcanic and interlayered sedimentary rocks suggests rapid rotation and fault slip at this time (Gans and Gentry, 2016). Coupled ZHe and AHe analyses from the Whipple Mountains show a pronounced initiation of rapid cooling at ca. 21.5 Ma (Stockli et al., 2006). This timing overlaps with the widespread intrusion of the Chambers Well dike swarm (Gans and Gentry, 2016).

The coupled Buckskin-Rawhide and Harquahalah MCCs yield a range

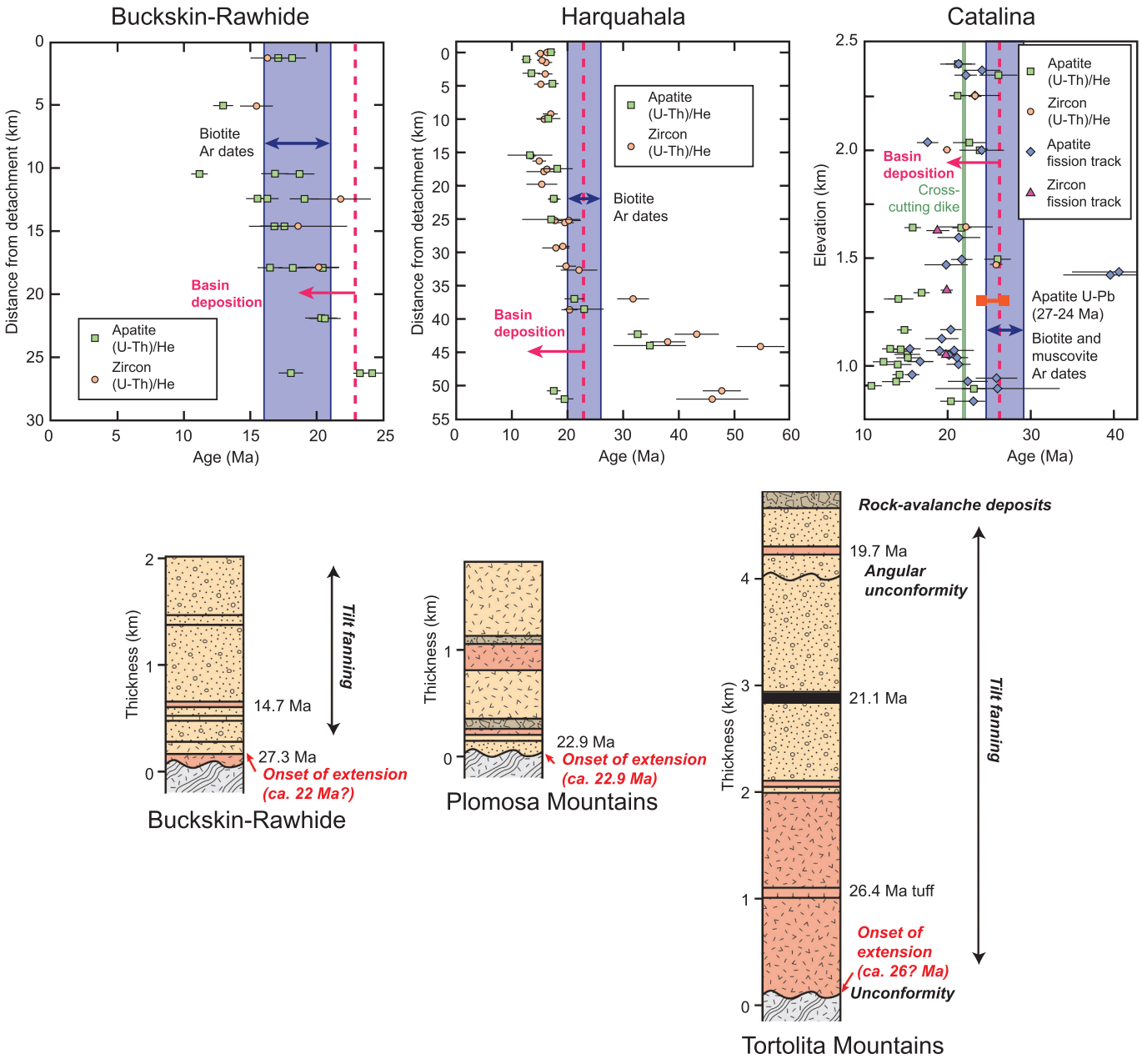

Fig. 15. (*continued*).

of biotite $^{40}Ar/^{39}Ar$ ages spanning 26–16 Ma (Richard et al., 1990; Scott et al., 1998). In the Buckskin-Rawhide MCC, the ca. 22–21 Ma Swansea Plutonic Suite is ductilely deformed, thus requiring deformation after its emplacement (Bryant and Wooden, 2008; Singleton and Mosher, 2012). Singleton et al. (2014) provided an AHe and ZHe traverse across the footwall rocks of the Buckskin-Rawhide system. Almost all dates were early-middle Miocene, except several of the structurally highest samples that yielded Late Cretaceous and early Cenozoic ages. These data are interpreted to suggest that detachment faulting and associated exhumation initiated in the early Miocene (ca. 20.5 Ma) (Singleton et al., 2014) (Fig. 15). A nearby traverse across the Harquala MCC footwall yielded similar results (Prior et al., 2016). Most ZHe and AHe dates were early-middle Miocene, except the structurally highest samples that yielded early-middle Cenozoic ages (Fig. 15). An interpreted break-in-slope in plots of age versus structural position is interpreted to reflect the initiation of detachment slip and exhumation at ca. 21 Ma.

4.4.7. *Catalina MCC*

The Catalina MCC preserves extensive peraluminous melts with igneous and metamorphic zircon U-Pb ages ranging from 57 to 45 Ma (Terrien, 2012; Fornash et al., 2013). There are distinct structural fabrics that are interpreted to have formed in the late Cretaceous-early Cenozoic during Laramide-age (ca. 70–50 Ma) deformation or forceful pluton emplacement (e.g., Bykerk-Kauffman and Janecke, 1987; Ducea et al., 2020). Some east-trending, east-directed shear fabrics along the eastern flank of the Catalina and Rincon mountains may represent Late Cretaceous-Early Paleogene deformation during the Laramide (e.g., Drewes, 1974; Thorman and Drewes, 1981; Bykerk-Kauffman and Janecke, 1987). An example of this older fabric is observed in Happy Valley, east of the Rincon Mountains, where deformed rocks, including severely flattened conglomerate clasts, with an E-NE-trending lineation are intruded by the undeformed ca. 28–27 Ma Happy Valley Granodiorite (Fig. 11D) (e.g., Spencer et al., 2011).

Muscovite-plagioclase Rb-Sr isochron ages of ca. 34 Ma from

peraluminous granite samples in the Catalina MCC record cooling through 450–400 °C based on estimates for the closure-temperature of the Rb-Sr system in muscovite (e.g., Ducea et al., 2020; Ribeiro et al., 2023). Apatite U-Pb ages from within the Catalina MCC mylonite zone yield ages of 27 to 24 Ma (Jepson et al., 2021; Davis et al., 2023), and biotite and muscovite $^{40}Ar/^{39}Ar$ dates record extensive cooling to temperatures below 300 °C between 28 and 23 Ma (Terrien, 2012; Davis et al., 2023). Cooling covaries spatially with position along the mylonite and cessation of mylonitization is interpreted at ca. 22 Ma evidenced by a cross-cutting, undeformed basaltic dike (Davis et al., 2023). Jepson et al. (2022) conducted ZFT, AFT, ZHe, and AHe analyses from across the footwall of the Catalina MCC, and multi-sample thermal inversion of the data suggests that upper crustal exhumation initiated ca. 25 Ma. The Catalina MCC later transitioned to a phase of high-angle normal fault associated with the regional Basin and Range extension (e.g., Dickinson, 1991). High-angle normal faults dissect the mylonitic carapace and cause extensive exhumation with possible renewed slip along the detachment (Fayon et al., 2000; Scoggin et al., 2021).

4.4.8. Summary of thermochronology data

The above compilation of medium- and low-temperature thermochronology can be used to interpret different parts of the MCC evolution. The $^{40}Ar/^{39}Ar$ dates track mid-crust exhumation and conditions of mylonitic shearing. A caveat is that mid-crust magmatism could potentially reset or complicate such ages. However, where applicable, $^{40}Ar/^{39}Ar$ dates overlap other cross-cutting relationship, providing confidence in their ability to track MCC exhumation (Fig. 5). The compilation reveals distinct trends in the $^{40}Ar/^{39}Ar$ ages that could be interpreted in two ways. The first interpretation is that there may be three distinct latitudinal domains of exhumation: (1) the MCCs north of the Snake River plain cooled in the Eocene (ca. 40–45 Ma), (2) the northern hinterland MCCs south of the Snake River plain cooled in the late Oligocene (ca. 25 Ma), and (3) the southern foreland MCCs cooled in early Miocene (ca. 20 Ma) (Fig. 5). Alternatively, the $^{40}Ar/^{39}Ar$ ages may reflect distinct monotonic trends: (1) the northern hinterland MCCs show a younging trend broadly from north to south at a rate of ~19 km/Myr and (2) the southern foreland MCCs show a younging trend to the northwest at a rate of ~24 km/Myr (Figs. 5 and 16).

The compiled low-temperature thermochronology from the northernmost hinterland MCCs (e.g., the Bitterroot, Anaconda, and Pioneer MCCs) shows broad Eocene cooling, a pulse of Oligocene cooling, and a late ca. 11–8 Ma pulse of cooling. The rest of the hinterland MCCs south of the Snake River Plain show middle Miocene cooling, with the rapid cooling at ca. 13.5 Ma starting in the ARG (Egger et al., 2003) and ca. 17 Ma cooling initiation in the REHR (Colgan et al., 2010) and Snake Range (Miller et al., 1999). In the southern foreland MCCs, low-temperature thermochronology tracks cooling from the late Oligocene-early Miocene (ca. 25–20 Ma) around the Catalina MCC (Fayon et al., 2000; Jepson et al., 2022) to the middle Miocene (ca. 16 Ma) near the McCullough Range just south of Las Vegas, Nevada (Mahan et al., 2009; Zuza et al., 2022a). Therefore, these age trends reveal a monotonic signal of northward younging ages, from ca. 27 Ma at the Catalina MCC to ca. 13.5–10 Ma at the ARG and Pioneer MCCs in the north (Fig. 16).

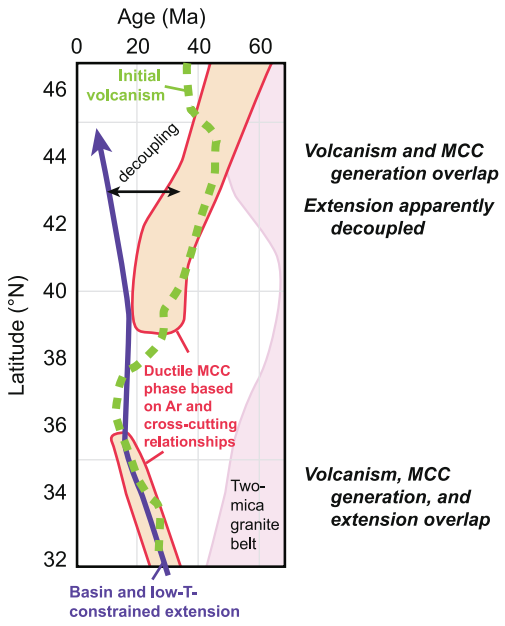

Fig. 16. Summary of timing constraints for the MCCs in the North American Cordillera as discussed in this synthesis.

4.4.9. Thermal history modeling

To quantitively investigate the thermal histories within a given MCC system, we constructed thermal history models for some of the individual MCCs. Thermal history modeling was performed utilizing published ZHe, AHe and AFT single-grain ages, and associated mean-track length distributions, with D_{par} (e.g., Donelick et al., 2005) used as kinetic parameters. Here, we used the QTQt software (version 5.8.6) to model the thermal history of the samples (Gallagher, 2012). The QTQt software applies a Bayesian trans-dimensional approach to Markov Chain Monte Carlo statistics (Gallagher, 2012) to produce a cooling evolution of the sample that predicts the measured data by applying the AFT annealing model after Ketcham et al. (2007), the AHe diffusion model after Flowers et al. (2009), and the ZHe diffusion model after Guenthner et al. (2013). Models were further refined using published zircon U-Pb data for starting points and Rb-Sr and $^{40}Ar/^{39}Ar$ data as *T-t* constraints. There is limited *T-t* data between the high- and medium-temperature thermochronometers, and thus we urge caution in interpreting the paths of the higher temperature cooling histories (700–500 °C). Detailed modeling metadata are available in Supplementary Table 1 and Supplementary Figure 1.

Black boxes in the thermal history models (Fig. 17) show the input constraints (detailed in Supplemental Table 1). In comparing MCCs, we investigated when a given system cools below conditions for mylonitic shearing (e.g., ~550 to 300 °C; green shading in Fig. 17) and when a system cools to surface conditions (e.g., <60 °C). Thermal history models were based on spatial proximity to the detachment fault coupled with the density of thermochronometers applied to a given sample (e.g., single sample, multi-method thermochronology). Where necessary additional cooling constraints were added from proximal samples, sample selection and summary data are available in Supplementary Table 1.

The Anaconda MCC shows a broad range of monotonic cooling from ~500 °C to surface conditions in the Eocene-Oligocene (ca. 50 Ma to 40–30 Ma) (Fig. 17A). The ARG MCC shows cooling through mylonite-generating conditions ca. 30–20 Ma, with a pronounced phase of rapid cooling to surface conditions ca. 13 Ma (Fig. 17B). For the REHR, we plotted two separate *T-t* paths because there were ample data from: (1) within the mylonitic shear zone with synkinematic Oligocene plutons in the East Humboldt Range and (2) the ca. 36 Harrison Pass pluton (Barnes et al., 2001) in the Ruby Mountains that was not mylonitically sheared and occupied a position above the MCC mylonites (Fig. 9A). In their structural reconstruction, Colgan et al. (2010) suggest that analyzed Harrison Pass samples originated from a depth of 6–10 km in the Eocene. The mylonite *T-t* path shows thermal holding at mylonitic conditions through the Oligocene, followed by rapid cooling below ~200 °C starting ca. 24–22 Ma (Fig. 17C). The ca. 36 Ma Harrison Pass pluton *T-t* path shows continuous slow cooling after intrusion to ~200 °C by ca. 15 Ma, after which there was enhanced cooling to surface conditions in the middle-late Miocene (Fig. 17C). The Harrison Pass *T-t* path could reflect simple conductive cooling after the emplacement of the Harrison Pass pluton to background temperatures given the samples originated from ~200 °C, or ~8 km depth assuming a 25 °C/km

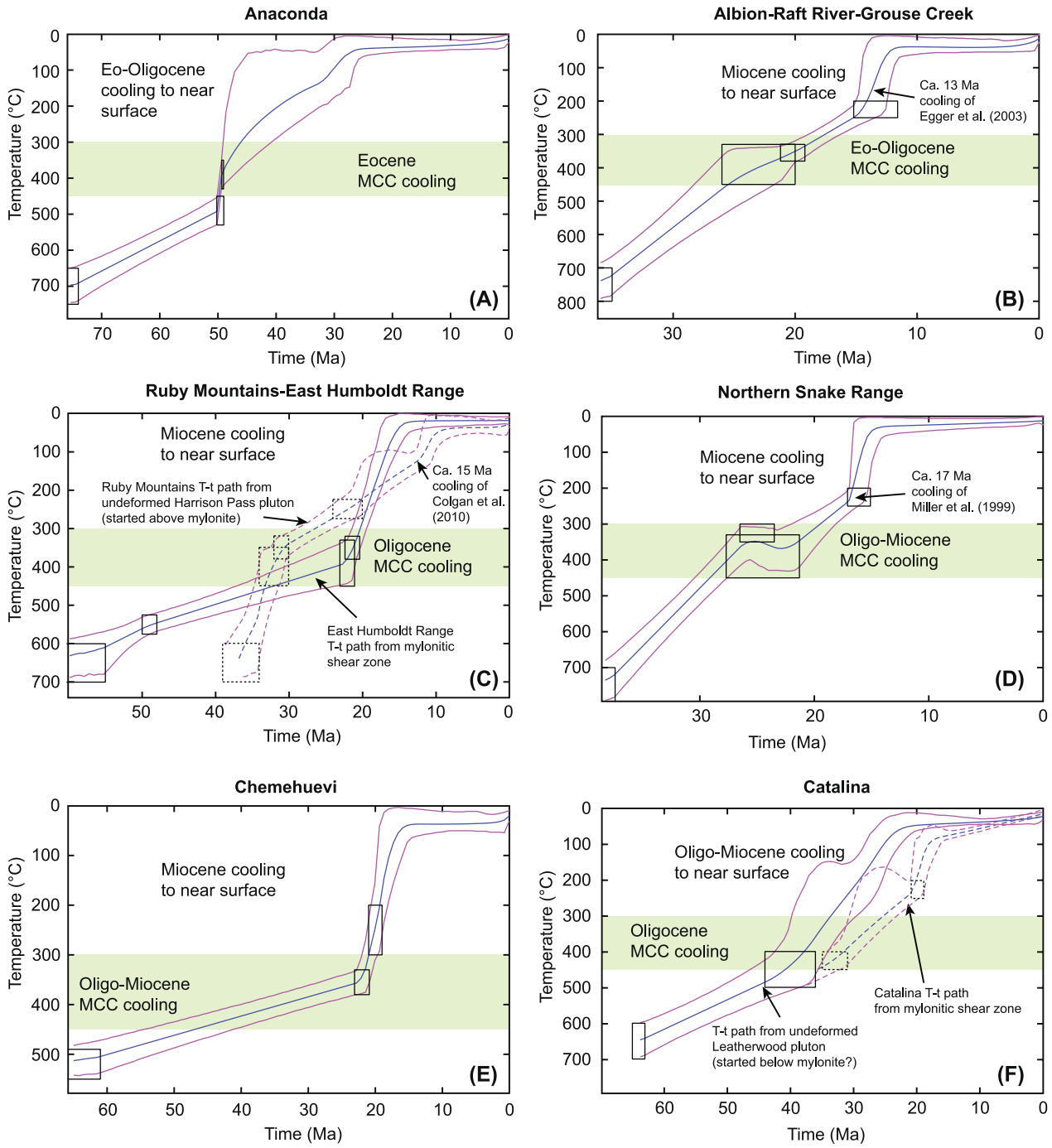

Fig. 17. Representative inverse thermal history models (QTQt; Gallagher, 2012) of several MCCs, arraged from north to south. Solid blue like is the maximum likelihood model and the pink envelope represented a 95% confidence interval. Model fits and underlying data can be found in Supplementary Table 1 and Supplementary Figure 1. See text for discussion.

geotherm. Samples were subsequently exhumed to the surface during mid-Miocene extension (Colgan et al., 2010) (Fig. 17C).

In the northern Snake Range, samples cool monotonically to 550–300 °C at ca. 35–20 Ma followed by a mid-Miocene pulse of cooling to surface conditions at ca. 17 Ma (Fig. 17D). In the south, Chemehuevi samples remain isothermal and/or slowly cool in the Eocene-Oligocene with a pulse of rapid cooling to surface conditions at ca. 25 Ma (Fig. 17E). However, the resolution on the Chemehuevi system is poorer relative to other MCCs due to limited high- to mid-temperature geo−/thermochronometric data.

For the Catalina samples, we plotted two separate *T-t* paths because there were ample data from: (1) within the mylonitic shear zone and (2) the undeformed-to-moderately foliated Late Cretaceous Leatherwood granodiorite that was structurally beneath the mylonitic shear zones (Fornash et al., 2013; Ducea et al., 2020). Both samples cooled to 450–300 °C by ca. 40–35 Ma (Fig. 17F). The Late Cretaceous Leatherwood granite cooled below 300 °C at ca. 35–30 Ma followed by cooling to surface conditions by ca. 25 Ma (Fig. 17F). Conversely, the mylonitic shear zone departed from the Leatherwood *T-t* path at ca. 30 Ma, showing later, delayed cooling to surface conditions ca. 20 Ma (Fig. 17F).

With the exception of the Anaconda MCC, all systems show a

polyphase cooling history, with cooling to mid-crust temperature conditions, a variable phase of isothermal holding, followed by later cooling to surface conditions (Fig. 17). This observation is similar to the qualitative evaluation of the $^{40}Ar/^{39}Ar$ ages versus low-temperature thermochronology datasets that suggests decoupled two-phase cooling (Fig. 16).

In the REHR and Catalina MCC systems, separate QTQt *T-t* paths were constructed for the mylonitic shear zones and rocks above (i.e., REHR) and below (i.e., Catalina) the mylonitic shear zone that reveal complex thermal histories (Fig. 17). In the simplest model of detachment-slip related exhumation of the lower plate rocks, the structurally higher samples would be expected to cool earlier than the structurally deeper samples. However, the opposite is observed for both the REHR and Catalina MCCs, with the mylonitic rocks in the REHR cooling after Harrison Pass pluton and the Leatherwood granite in the Catalina MCC cooling before the mylonitic rocks (Fig. 17). The continuous cooling path of the Harrison Path pluton (Fig. 17C) may reflect conductive cooling after its Eocene intrusion to ambient crustal temperatures before rapid mid-Miocene exhumation. The structurally deeper REHR mylonites remained at >300 °C until ca. 22 Ma. The decoupled and delayed cooling of the of the Catalina mylonites relative to the structurally deeper Leatherwood granite suggests a possible disconnect between mylonitic shearing and lower-plate exhumation.

4.5. Syn-kinematic basin sedimentation

Following the removal of hanging wall rocks during regional extension, the generated space may be filled in with syn-kinematic sediments as part of a supradetachment basin system (e.g., Forshee and Yin, 1994; Friedmann and Burbank, 1995) (Fig. 1). The syn-kinematic basin record for each MCC system is described below.

4.5.1. Bitterroot, Anaconda, and Pioneer MCCs

The northern Bitterroot, Anaconda, and Pioneer MCCs are not associated with major syn-kinematic basin deposits. Eocene to Miocene deposits of the Renova Formation are distributed across southwest Montana and eastern Idaho. Although interpretations for these deposits vary, there is a general consensus that they were deposited in a broad relatively quiescent setting, either adjacent to broad rift uplifts or as intermontane basins (e.g., Stroup et al., 2008; Rothfuss et al., 2012; Schwartz and Graham, 2017; Thoresen et al., 2024). Around the Anaconda MCC, discontinuous and thin Cenozoic deposits, interbedded with Eocene volcanic rocks (e.g., Dudas et al., 2010), reach a maximum reported thickness of ~200 m (O'Neill et al., 2004; O'Neill and Tysdal, 2005). These Cenozoic deposits are thinner and less deformed (e.g., tilted) than those adjacent to MCCs in the south.

4.5.2. Albion-Raft River-Grouse Creek MCC

In the ARG, the Miocene Salt Lake Formation of the Cenozoic Raft River Basin is exposed along the east side of the Albion Mountains and north side of the Raft River Mountains (Compton, 1972, 1975; Williams et al., 1974, 1982; Smith, 1982; Covington and Miller, 1983; Pierce et al., 1983; Wells, 2009). Konstantinou et al. (2012) provided an updated synthesis and dates from the Salt Lake Formation. The lowest strata consist of breccias, fanglomerates, and pebble conglomerates were deposited unconformably over Pennsylvanian-Permian sedimentary rocks (Fig. 13). The section fines upward with sandstone, conglomerate, and interlayered tuffs. Metamorphic and plutonic rocks are observed >700 m from the base of the section. U-Pb zircon ages from the base of the section, including a dated tuff and MDAs from detrital analysis tightly constrain the basal age to ca. 13.5 Ma (Konstantinou et al., 2012). Progressively younger volcanic rocks occur upsection, including an ca. 8.2 Ma rhyolite lava (Fig. 13). This section middle-late Miocene sedimentary package is >3 km thick.

4.5.3. Ruby Mountains-East Humboldt Range MCC

Cenozoic deposits in northeast Nevada around the REHR region include the Eocene Elko and Copper, Oligocene(?)-Miocene Clover Creek, and Miocene Humboldt basins (Henry, 2008; Henry et al., 2012; McGrew and Snoke, 2015; Smith et al., 2017; Canada et al., 2021; Zuza et al., 2021). The Eocene basins are generally interpreted as hinterland lakes or infilled paleovalleys (e.g., Lund Snee et al., 2016; Smith et al., 2017; Henry, 2018), and the relatively thin nature of the deposits precludes major extension/faulting at this time (Dubiel et al., 1996; Henry, 2018). The main phase of mylonitic shearing in the REHR occurred in the late Oligocene (29–22 Ma), and therefore there has been great attention to documenting a contemporaneous syn-kinematic basin. The Clover Creek sediments exposed along the northeastern flank of the East Humboldt Range are the best possible candidate for such syn-kinematic sediments. The Clover Creeks sequence was deposited over, and parallel to, Eocene and Oligocene tuffs, and below, and parallel to, the base of the Miocene Humboldt Formation and interbedded ca. 15.5 Ma rhyolite (Sharp, 1939; Colgan et al., 2010; Zuza et al., 2021) (Fig. 13). The Clover Creek sequence consists of conglomerate, sandstones, shales, and a pronounced megabreccia deposit near its based consist of unmetamorphosed Devonian limestones that are interpreted as rock-avalanche deposits that formed during initial range exhumation caused by extension and normal faulting (McGrew and Snoke, 2015). The ages of these deposits are bracketed between 28.9 Ma—the age of the underlying Tuff of Campbell Creek—and 15.6 Ma—the age of an overlying tephra (Zuza et al., 2021). With these constraints, there is a ~ 700-m thick section that could possibly be late Oligocene or may simply be middle Miocene. Recent detrital zircon and sanidine analyses constrain these deposits to younger than 20.1 Ma (Henry et al., 2023). Henry et al. (2023) suggests that volcanism of the southwest sweeping Eocene-Miocene ignimbrite flareup was distal to the Clover Creek Basin between 20 Ma and 16 Ma. Renewed volcanism did not initiate until the ca. 15.5 Ma Jarbidge rhyolites were erupted associated with the Yellowstone hotspot (Brueseke et al., 2014), which would have limited the availability of detrital zircons or sanidine in 20–16 Ma timeframe. Therefore, we interpret that the Clover Creek sequence represents the ca. 17 Ma basal middle Miocene Humboldt Formation based on the parallel, conformable nature of the sequence (Fig. 13); however, we acknowledge it may be as old as ca. 20 Ma.

4.5.4. Northern Snake Range MCC

In the northern Snake Range, the Oligocene-Miocene Sacramento Pass Basin consists of a basal ca. 30.8 Ma rhyolite tuff, upon which lacustrine limestone rocks were deposited with interfingering rock-avalanche deposits (Grier, 1983; Martinez, 1999; Gébelin et al., 2012; Ruksznis, 2015). These rock-avalanche deposits are interpreted to record the initiation of significant range exhumation and relief generation, thus possibly signifying the onset of locale extension. Rhyolite tuffs within the limestone unit yielded biotite $^{40}Ar/^{39}Ar$ dates of ca. 20 Ma (Martinez, 1999). This part of the stratigraphy is overlain by >2 km thick alluvial fan conglomerate that is interpreted to be a syn-kinematic extensional basin (Fig. 13). Therefore, major regional extension and fault-related range growth is interpreted to have occurred after ca. 20 Ma.

4.5.5. Colorado River Extensional Corridor

Syn-kinematic basins in the southern MCCs are well developed and well dated, which is part due to the overlapping timescales of voluminous volcanism, extension, and MCC development. In the CREC, just south of Las Vegas, there is a >4-km-thick exposure of tilt-fanned Miocene volcanic rocks that show significant variations in dip (Fig. 15) (e.g., Faulds et al., 2002). The ca. 18.5 Ma Peach Springs tuff underlying the tilt-fanned stratigraphy appears to be pre-kinematic, and a pronounced change in dips starts at ca. 16.5 Ma, which is interpreted as the age of extension here. Gans and Bohrson (1998) similarly interpreted an imitation of tilt fanning at ca. 15 Ma in the Eldorado

Mountains.

To the south in the Chemehuevi and Whipple Mountains, tilt-fanned terrestrial deposits with rock-avalanche megabreccia record initial extension at ca. 19 Ma, just before the deposition of the ca. 18.5 Ma Peach Springs tuff (Miller and John, 1999; Yin and Dunn, 1992; Dorsey and Becker, 1995). To the southeast in the Buckskin-Rawhide and Plomosa Mountains, tilted terrestrial deposits up to ~2-km thick with megabreccia horizons suggest extension initiation ca. 22 Ma (Prior et al., 2018; Spencer et al., 2018) (Fig. 15).

4.5.6. Catalina MCC

One of the thickest non-marine basin sections in the southern MCCs is observed in the Tortolita Mountains, just west of the Catalina MCC (Spencer et al., 2021). This >4-km-thick section was deposited unconformably on Proterozoic schist, and shows changing dips and tilting fanning from ca. 27 Ma to ca. 20 Ma (Fig. 15) (Peters et al., 2003). The entire section is in detachment fault contact with the mylonitic shear zones in the Tortolita Mountains (Spencer et al., 2021).

4.5.7. Basin sedimentation summary

In summary, the MCC regions south of the Snake River Plain show pronounced syn-kinematic terrestrial basin deposition. These deposits broadly young northward from Oligocene (ca. 27 Ma) in the Catalina MCC to middle Miocene (ca. 13.5 Ma) in the ARG. All of these syn-kinematic deposits exhibit relationships consistent with deposition in an extensional setting, including tilt-fanning of the deposits, rock-avalanche deposits in the lower parts of the section suggesting large relief adjacent to active normal faults, and lacustrine layers suggestive of deposition in a closed fault-bounded basin. Taken alone, the basin history synthesis suggests that basin-development associated with regional extension younged northward from Oligocene initiation at Arizona latitudes to mid-Miocene initiation in the ARG. This younging pattern is rapid, propagating northward at a rate of ~81 km/Myr (Fig. 5).

The Cenozoic basin history north of the Snake River Plain is less straightforward to interpret. The Eocene-Oligocene deposits are thin, minimally tilted, and interpreted to have been deposited in a broad relatively quiescent setting, either adjacent to broad rift uplifts or as intermontane basins. Based on comparison with the syn-kinematic basins located adjacent to MCCs to the south of the Snake River plain, we interpret that these northern basins do not uniquely reflect an extensional history and were instead deposited in a highland associated with the Mesozoic-early Cenozoic subduction history. This is because the northward migration of the Mendocino triple junction and associated extension has not impacted the northernmost MCCs, consistent with the spatially varying cooling recorded in the low-temperature thermochronology data discussed above.

4.6. Interpretations of age constraints

Integration of our timing datasets reveals important insights for MCC development in the Cordillera. The medium-temperature thermochronology datasets track the timing of ductile shearing, as the closure temperatures of mica $^{40}Ar/^{39}Ar$ thermochronology (300–400 °C) overlaps the deformation temperatures in many of these shear zones (e.g., 300–500 °C; Behr and Platt, 2011; Gottardi et al., 2020; Levy et al., 2023). The $^{40}Ar/^{39}Ar$ thermochronometer is sensitive to thermal perturbations, such that disentangling deformation-related exhumation versus conductive cooling is not always straightforward. However, we suggest these $^{40}Ar/^{39}Ar$ date trends provide useful constraints on MCC shear-zone evolution because they bracket the minimum age of ductile shearing, define broad age trends that suggest minimal mixed-age signals due to local magmatism, and are consistent with direct cross-cutting relationships (Fig. 5). Our synthesis reveals broad a broad pattern of ductile shearing younging in the Eocene to early Miocene toward central latitudes (~37°N) with migration rates of ~20 km/Myr (Figs. 5 and 16). The low-temperature thermochronology and basin sedimentation datasets from the MCCs can be interpreted to reflect surface-breaking brittle normal faulting activity. These ages show an overall trend that youngs very rapidly northward (~81 km/Myr) (Figs. 5 and 16). The ages of ductile shearing and brittle extension overlap for the southern foreland MCCs but are divergent for the central hinterland MCCs (Fig. 16). There is no correlation between the Late Cretaceous-Paleogene peraluminous pluton age trends and the MCC thermochronology ages. Instead, mid-crust ductile shearing associated with medium-temperature thermochronology (~300 °C) overlap with post-Farallon slab rollback volcanism (Fig. 16). Taken together, the correlation between migrating volcanism and MCC formation across the study area may imply a causal relationship. Conversely, although upper-plate extension and MCC formation overlap in the south, the discordance between these features in the north suggests they may not be uniquely related (Fig. 16).

Our new thermal history models for several of the MCCs hint at complex cooling histories for the MCCs (Fig. 17). Most of these models show thermal holding at brittle-ductile transition depths, rather than continuous cooling. Only the Anaconda MCC thermal models show continuous fast cooling below temperatures below 300–200 °C in the Eocene (Fig. 17). The Anaconda MCC is also the only system of our thermal history models that did not experience renewed Miocene Basin and Range extension, consistent with Eocene cooling to near surface conditions with little subsequent cooling. The other thermal history models that show isothermal holding at brittle-ductile transition depths hint at some decoupled phases of mid-crust and upper-crust exhumation histories, which is consistent with our synthesis of cross-cutting relationships, medium-temperature thermochronology, low-temperature thermochronology, and basin sedimentation records (Figs. 5 and 16).

5. Working hypothesis for metamorphic core complex formation

5.1. Tests of MCC models

Since the 1980s, the long-held working model for the generation of MCCs in the North American Cordillera (Fig. 5) is that they accommodate large-magnitude crustal extension, either as a coupled system of brittle normal faults that kinematically link down-dip with ductile shear zones or via brittle normal faults capturing a kinematically similar system of mid-crust shear zones (e.g., Crittenden et al., 1980; Davis, 1988; Lister and Davis, 1989; Cooper et al., 2017) (Fig. 3A). These prevailing models predict that regional extension, ductile shearing, brittle normal faulting, and syn-kinematic basin deposition should be active synchronously.

In the southern foreland MCC belt, available evidence supports such kinematic linkages on overlapping spatial and temporal scales (Fig. 16). Within a given MCC system, mylonitic shearing bracketed by cross-cutting relationships and $^{40}Ar/^{39}Ar$ thermochronology occurred at the same time as brittle faulting, upper crustal cooling, and syn-kinematic basin formation (Fig. 16). Several of these MCCs expose a mylonitic front, which supports a model where brittle detachment faulting captures a mid-crust ductile shear zone (e.g., Davis, 1988; Singleton and Mosher, 2012). In most of these MCCs, coeval basin deposits demonstrate hanging wall removal created an open space above the footwall that could have resulted in significant isostatic rebound of the footwall rocks (Wernicke and Axen, 1988).

However, attempts to use this generic model to explain the northern hinterland MCCs are less successful. Our compilation of the geology and geochronology relationships from the hinterland MCCs reveals a pronounced decoupling from earlier Paleogene ductile shear fabrics and later Miocene detachment and high-angle normal faults (Fig. 16). Importantly, there are no syn-kinematic basins or signals of upper-crustal exhumation that are coeval with Eocene-Oligocene ductile shearing, which means that there is no record of major surface-breaking normal faults and accompanying hanging wall removal to drive isostatic footwall uplift. The lack of Eocene-Oligocene syn-kinematic basins could

reflect rapid isostatic rebound or slow erosion-deposition rates that suppress basin formation and preservation. These basins could have similarly been uplifted and eroded, leaving no geologic record. However, we do not think these situations apply. Records of large Eocene lake basins are preserved, such as the Elko basin in northeast Nevada (e.g., Haynes, 2003; Smith et al., 2017) or the newly recognized Fallout Hills basin in southern Nevada (Lundstern et al., 2024). These lacustrine deposits do not show evidence for significant Eocene or Oligocene deformation, and thick Miocene syn-kinematic terrestrial deposits that are exposed across much of northeast Nevada are subparallel to the thin Eocene-Oligocene deposits (e.g., Lund Snee et al., 2016; Zuza et al., 2021). The Miocene deposits are cut and tilted by the normal faults as part of the middle Miocene initiation of Basin and Range extension, and these deposits temporally overlap with lower-plate exhumation (Fig. 13). Unusual and unique processes would have had to have occurred in the Eocene-Oligocene for rapid brittle faulting to leave no record of syn-kinematic basin or upper-crustal cooling and exhumation.

One could interpret that the $^{40}Ar/^{39}Ar$ thermochronology data from the hinterland MCCs track Eocene-Oligocene footwall cooling and tectonic exhumation related to regional extension, and nearly continuous deformation caused the footwall rocks to cool through the upper crust (< 250 °C) later in the Miocene. That is, these thermochronometers could be tracking continuous, protracted extension. If this is true, this implies that protracted extension was occurring for over 20–30 Myr, depending on the particular MCC and interpreted onset of mylonitic shearing, at relatively slow strain rates (e.g., Wells, 2001; Wang et al., 2011; Evans et al., 2015; Long et al., 2023). We argue against this interpretation for three primary reasons: (1) kinematic models of this process imply substantial structural relief and accommodation space (e.g., Wells et al., 2000; Wells, 2001; Long et al., 2022, Long et al., 2024) that should have resulted in syn-kinematic basin deposition synchronous with ductile shearing, which is not observed despite a well-preserved record of thin pre-kinematic Eocene deposits and thick syn-kinematic Miocene deposits; (2) protracted extension and normal-fault slip would be expected to yield a more continuous record of thermochronology ages due to different slip and variable exhumation, yet we observe a clear dichotomy of ages across all of the hinterland MCCs (Fig. 16); and (3) protracted shear-zone activity from the Eocene-Oligocene to middle Miocene implies fairly slow slip or strain rates, at odds with calculated exhumation rates from thermochronology studies (e.g., Wells et al., 2000; Miller et al., 1999; Colgan et al., 2010) or interpreted strain rates from microstructure-based studies (e.g., Hacker et al., 1990; Gottardi and Teyssier, 2013; Zuza et al., 2022b; Levy et al., 2023). The inverse thermal history models for most of the MCCs suggest a period of isothermal holding, or reduced cooling rates, at mid-crustal brittle-ductile transition temperatures (Fig. 17).

All the MCCs synthesized in this work show structural relationships consistent with the brittle normal fault soling into the primary mylonitic shear zone (Fig. 7). Such a relationship suggests either the direct kinematic linkage between brittle and ductile structures or the preferential brittle reactivation of mylonitic zones as mechanically weak décollement surfaces during normal faulting. Across the Cordillera, there are no primary mylonitic shear zones duplicated by normal faults, except the Buckskin-Rawhide MCC (e.g., Singleton et al., 2014; Fig. 7G), which confirms that MCCs are not primarily formed via a series of high-angle normal faults that rotate as dominos or bookshelf fault systems (cf. Proffett Jr, 1977; Favorito and Seedorff, 2021). The detachment faults are not always uniquely associated with the mylonitic shear zones, such as the Ruby Mountains (Fig. 9A) or the mylonitic front examples in the southern MCCs (Davis, 1988; Singleton and Mosher, 2012) (Figs. 9B and 6E). This is evidence that the mylonitic shear zones are weak décollements that get exploited and reactivated via brittle normal faulting.

Some of the MCCs display rather complex structural patterns within their footwalls. The ARG (Figs. 6B and 7C), REHR (Fig. 9), and northern Snake Range (Fig. 6C and 7D) expose structural levels both above and below the mylonitic shear zone (Fig. 4F) (e.g., Konstantinou et al., 2012, 2013; Colgan et al., 2010; Cooper et al., 2010, 2017). Several MCCs display shear zones with opposing shear sense (Fig. 4), such as in the ARG (i.e., hinterland MCC) with the top-west Middle Mountain versus top-east Raft River shear zones (Fig. 6B) and in the Catalina MCC (i.e., foreland MCC) with the top-northeast Molino Basin shear zone versus the top-southwest shear zones exposed on the southwestern flank of the Catalina-Rincon Mountains (Figs. 6F and 7H). There are rare top-east fabrics observed in the eastern part of the REHR, compared to the dominantly top-west shear fabrics (McGrew and Casey, 1998). Available timing constraints allow these opposite shear zones to have been active synchronously, although some studies argue for differing ages (e.g., Wells et al., 2000). These examples appear to be similar to scenario j in Fig. 4. However, these shear zones with opposing senses of shear have been explained away as conjugate-shear or flow structures that accommodated footwall exhumation (e.g., Reynolds and Lister, 1990; Spencer et al., 2022), simple opposite-vergence extensional shear zones (Wells, 2001), or sub-LDT distributed shear zones (Cooper et al., 2010).

Based on the above logic, the southern foreland MCCs can potentially be interpreted to have formed via regional extension, but the northern hinterland MCCs are not readily explained by this process. MCCs farther north of those considered in this synthesis, such as the Shuswap in British Columbia, also show lower-plate exhumation and decompression significantly before the onset of regional extension (Norlander et al., 2002). Given the broad similarities between the MCCs across the entire Cordillera and the regional Mesozoic-Cenozoic geologic history (Fig. 2B) (e.g., Coney, 1980), we favor interpretations that invoke a common formational mechanism for all of the MCCs across the Cordillera.

5.2. Decoupled ductile shearing vs brittle faulting

The MCC ductile-shear zone age trends (e.g., $^{49}Ar/^{39}Ar$ and cross-cutting relationships) reveal a broad younging pattern toward central latitudes (~37°N) with migration rates of ~20 km/Myr, which are similar to the trends of migrating volcanism at rates of 10–20 km/Myr (Figs. 5 and 16). Conversely, estimates of regional extension show a rapid northward younging trend (~81 km/Myr), parallel to the northward of the Mendocino triple junction (Figs. 5 and 16). The similar migration direction and rates between volcanism and MCC generation supports a potential linkage, whereas regional extension trends are discordant in direction and rate. These observations suggest that Late Oligocene-Miocene normal faults that rapidly migrated northward from Arizona since ca. 30 Ma captured earlier ductile shear fabrics.

Recent studies have emphasized the spatial and temporal link between Cenozoic magmatism and MCC deformation. In both the ARG and REHR, Eocene-Oligocene intrusions transition from a more juvenile source in the Eocene to more evolved granites due to crustal melting in the Oligocene (Strickland et al., 2011; Konstantinou et al., 2012; Snoke et al., 2024). The younger Oligocene granites correlate with domains of mylonitic shearing (e.g., Strickland et al., 2011; Zuza et al., 2022b). Additionally, Chapman et al. (2024) recently demonstrated the northwestward migration of magmatism and MCC exhumation across the southern MCC belt. Slab rollback after the Laramide flat-slab event led to trends of volcanism across the Cordillera (Fig. 12) (e.g., Copeland et al., 2017). The increased mantle heatflux beneath the thickened crust of the Nevadaplano orogenic plateau would have been conducive to widespread partial melting of the crust (e.g., Houseman et al., 1981; Thompson and Connolly, 1995; Vanderhaeghe, 2009; Kaare-Rasmussen et al., 2024).

5.3. New working hypotheses for MCC development

Based on the above discussion and synthesis, and our critical evaluation of possible tectonic models, we develop two new working hypotheses for MCC development that emphasize the correlation between magmatism and MCC activity, the decoupled phase of ductile and brittle

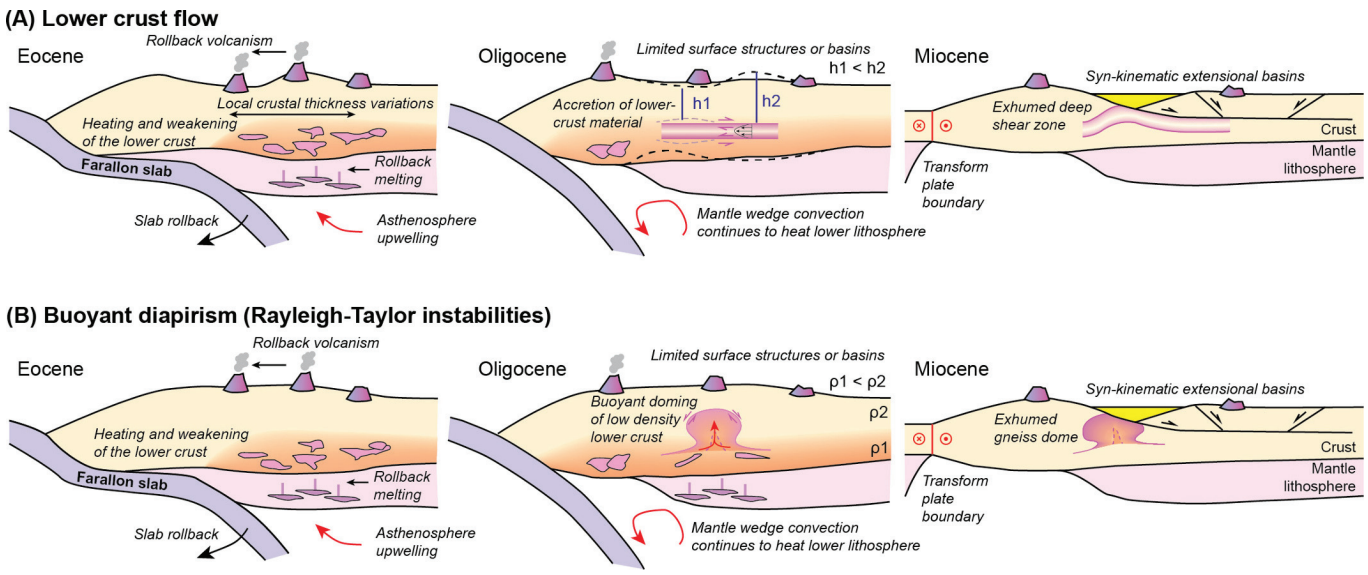

Fig. 18. Two working hypotheses for metamorphic core complex formation within the North American Cordillera that are consistent with observations synthesized in this study, including pre−/syn-kinematic magmatism, ductile deformation that preceded surface deformation and basin formation, and later brittle faulting. (A) The mylonitic shear zones exposed in the metamorphic core complexes may record middle-to-lower crust channel flow due to lateral pressure gradients caused by crustal thickness variations (h_1 vs h_2). Crustal flow may have initiated after significant crustal heating and thermal weakening following Farallon slab rollback magmatism. Later extension captured such middle-to-lower crust shear zones. (B) The mylonitic shear zones exposed in the metamorphic core complexes may be part of buoyant domes that rose as Rayleigh-Taylor instabilities when the lower crust was heated and experienced partial melting after Farallon slab rollback magmatism. Later extension focused along the flanks for these domes to asymmetrically exhume them. See text for more discussion. (For interpretation of the references to colour in this figure legend, the reader is referred to the web version of this article.)

deformation, and our knowledge of evolution of North American Cordillera plate-boundary conditions. The MCCs may represented (1) exposed remnants of a mobile, ductile mid-crust or (2) exhumed buoyant diapiric domes that were subsequently exhumed by brittle normal faults (Fig. 18). These models leverage previous interpretations of crustal mobility around and beneath the MCCs, such as required to explain the flat Moho beneath them (e.g., Gans, 1987; McCarthy et al., 1991; Buck, 1991; Say and Zuza, 2021).

For the first model, the Cenozoic ductile shear zones within the MCCs may represent mid-crust shear zones that accommodate a low-viscosity lower crust that flows to smooth out lateral crustal thickness gradients (e.g., Kruse et al., 1991; McQuarrie and Chase, 2000) following magmatic-induced thermal weakening (e.g., Vanderhaeghe and Teyssier, 2001) (Fig. 18A). The Cordilleran crust was thickened following phases of Sevier and Laramide deformation and crustal thickening. After hydrating and priming the mantle lithosphere during flat-slab subduction (Humphreys et al., 2003), Farallon slab rollback or foundering led to an influx of hot asthenosphere against the fertile mantle lithosphere that caused widespread magmatism to sweep across the western United States, following slab rollback. This magmatism would have greatly heated and weakened the lower crust, potentially over 10s of Myr timescales (e.g., Kaare-Rasmussen et al., 2024). Such thermal weakening may have enabled lower-crustal flow in response to lateral pressure gradients based on local crustal thickness heterogeneities (e.g., Vanderhaeghe, 2012). In this case, phases of crustal flow and associated mylonitic shear zones would track rollback magmatism. A mobile lower crust would minimally impact the upper crust, which can explain the lack of surface-breaking normal faults or major syn-kinematic basins during mylonite development. Specifically, popular channel flow models in a contractional orogen predict a lack of upper-crust structures (Royden et al., 1997; Vanderhaeghe and Teyssier, 2001; Hubbard and Shaw, 2009; Zuza et al., 2016), a prediction that may be applicable to the North American Cordillera as it transitioned to an extensional state.

In this model, Eocene-Oligocene mylonitic shearing was followed by Oligocene-Miocene upper-crustal extension and syn-kinematic basin development. These brittle structures would have preferentially reactivated the preexisting mylonite zones to thus result in broadly similar kinematics (e.g., Davis, 2013). The Oligocene-Miocene detachment normal faults would have captured and exhumed older mylonitic shear zones as the primary décollement layer (Davis, 1988; Singleton and Mosher, 2012; Cooper et al., 2017). Brittle normal faults would have to root beneath the mylonitic shear zones to expose rocks structurally deeper than the shear zones, as observed in several of the MCCs (Fig. 4). The overall spacing and geometry of the MCCs would have resulted from unique exhumation in late Oligocene-Miocene detachment fault systems, rather than initial variations in the Eocene-Oligocene shear zones. This model does not offer a unique explanation for the spacing dichotomy between the northern and southern MCCs (cf. Zuza and Cao, 2023). One speculative possibility is that the northern MCCs were developed in thick passive margin stratigraphy, so extensional detachment faulting may have resulted in wider spaced structures compared to the southern MCCs developed in orthogneiss with more closely spaced faults. One weakness of this crustal flow model is that it does not readily explain variable shear sense for the Paleogene mylonites. For example, the REHR involved top-west mylonites and the northern Snake Range involved top-east mylonites. If these formed due to lower crust mobility and lateral pressure gradients, there is not a satisfying explanation for why the lower crust would flow east at REHR latitudes and west at northern Snake Range latitudes. However, variable vergence could reflect local structural inheritance or GPE variations.

The second alternative model is a buoyant upwelling model for MCC generation, where heating and melting of the middle-to-lower crust reduced its density and drove buoyant gneiss dome generation as a Rayleigh-Taylor (RT) instability (e.g., Konstantinou et al., 2012, 2013; Levy et al., 2023; Zuza and Cao, 2023) (Fig. 18B). This model predicts that ductile shear fabrics that accompany doming should follow magmatic sweeps, as observed in Fig. 5. Ductile doming may also be expected to severely attenuate the rocks that form the top and rising flanks of the dome (Fig. 8) (Dixon, 1975; Cruden, 1988), as observed in analogous forcefully emplaced plutonic systems (e.g., Sylvester et al., 1978; He et al., 2009; Zhao and Cong, 2014; Zuza et al., 2024). For the ARG and REHR, igneous studies show progressive melting of the mid

crust from juvenile Eocene intrusions to more evolved Oligocene melts (Strickland et al., 2011; Konstantinou et al., 2012; Snoke et al., 2024). These two MCCs have previously been interpreted as buoyant gneiss domes (Konstantinou et al., 2012, 2013; Levy et al., 2023; Snoke et al., 2024).

In this model, the spacing of the RT diapirs would have been controlled to first order by the viscosity and thickness of the diapir and diapir-hosting crust (e.g., Fletcher, 1972; Ramberg, 1981; Fletcher and Hallet, 2004; Zuza and Cao, 2023). After stalling in the middle crust, these buoyant domes were captured by later normal fault systems to be exhumed to the surface. The brittle-fault structures would have rooted into preexisting mylonitic fabric décollements that dipped outwardly along the flanks of the gneiss dome (e.g., Davis, 2013). Normal-fault slip would have back-tilted the footwall rocks to a sub-horizontal position, and variably exposure of the lower plate could result in a single unidirectional shear sense or sometimes opposing shear senses (Fig. 4). This model implies that Paleogene MCC spacing was dictated by diapir instability spacing within the crust. Later distributed Miocene normal faulting may have exhumed similar structural levels across the Cordillera, capturing stalled MCC diapirs and non-MCC crust everywhere else.

The MCCs exposed in southwestern Canada and the northwestern USA (Fig. 2B) are often interpreted as diapiric gneiss domes because of the volume of migmatite and partial melts and their more domal geometry (e.g., Kruckenberg et al., 2008; Vanderhaeghe, 1999; Vanderhaeghe et al., 2003). These interpretations for the northern MCCs provide additional support for a diapiric origin for the MCCs of the central and southern MCC belts (Fig. 2B). This model thus unifies the origin for MCCs across the Cordillera, from Canada down to Mexico.

The channel-flow and diapir interpretations stated above are not mutually exclusive. Beneath a thick orogenic plateau, gravity may drive lateral channel flow in response to crustal thickness variations and gravitational instabilities to form local diapirs or crustal convection (e.g., Vanderhaeghe et al., 2018; Louis-Napoléon et al., 2020, 2022, 2024). The relative contributions of lateral versus vertical flow may result in a range of structural configurations, as reviewed by Whitney et al. (2004).

With either the channel flow or diapir interpretation, the ductile shearing phase of MCC generation was triggered by widespread post-Laramide rollback volcanism and significant melting of the middle-to-lower crust (Fig. 18) (e.g., Strickland et al., 2011; Snoke et al., 2024). Such magmatism and local partial melting would have lowered the density and viscosity of the middle and lower crust. The link between MCC development and slab rollback has been suggested previously, and it is possible that rollback and decreased plate convergence rates could be the necessary change in boundary conditions to drive orogenic collapse and extensional MCC development (Dewey, 1988; Rey et al., 2001; Vanderhaeghe and Duchêne, 2010). For example, Vanderhaeghe et al. (2003) suggested that a decrease in plate convergence rates between the Kula-Farallon and North American plates starting at ca. 56 Ma could have been the geodynamic driver for the initiation of deformation within the Shuswap MCC in southwest Canada. However, more recent plate reconstructions and geologic syntheses do not show an Eocene-Oligocene convergence-rate deceleration that temporally correlates with MCC deformation; convergence rates appear to remain high and roughly constant until the Mendocino triple junction migrates northward in the late Oligocene-Miocene (see Schellart et al., 2010; Yonkee and Weil, 2015). Furthermore, if rollback or slowed convergence rates led to orogenic collapse and MCC development in the Eocene-Oligocene, we would expect to observe an upper-crust response to such collapse. As discussed in this work, there is no record for upper crustal Eocene-Oligocene deformation in the central MCC belt region.

The plate-boundary conditions continued to evolve with the establishment of the Mendocino Triple Junction at ca. 30 Ma (Atwater, 1970). This plate-boundary configuration was conducive to distributed extension., and as the Mendocino Triple Junction migrated northward, geologic records of extension followed a similar trend, first initiating in the south and migrating northward rapidly (Fig. 16). Lithospheric extension across the hot Cordilleran orogen (Hyndman and Currie, 2011; Vlaha et al., 2024) would predictably lead to wide, distributed deformation (Buck, 1991; Vanderhaeghe, 2012) across the Basin and Range in the late Cenozoic.

In the southern Cordillera, Farallon slab foundering, asthenosphere upwelling, and volcanism was nearly synchronous with the formation of the triple junction, so that MCC formation, as either lower crustal flow or buoyant doming, and extension temporally overlapped (Fig. 16). For the northernmost belt of MCCs, there is a similar complicated history of slab windows or tears that may have facilitated or enhanced MCC development at ca. 60–50 Ma (e.g., Breitsprecher et al., 2003; Fuston and Wu, 2021).

5.4. Strain characteristics of a diapiric gneiss dome

If the diapiric gneiss dome model is relevant to MCC generation, there are certain predictions for the strain characteristics around the diapir wallrock, which have been investigated via scaled analog and numerical experiments of salt and gneiss domes (e.g. Dixon, 1975; Cruden, 1988; Talbot and Jackson, 1987; Jackson and Talbot, 1989) (Fig. 19). The wallrock above and around the rising diapir should be significantly strained, with the most substantial strains occurring at the top of the diapir with vertical shortening and horizontal extension (Fig. 19) (e.g. Dixon, 1975; Cruden, 1988; Talbot and Jackson, 1987; Jackson and Talbot, 1989). Rock within the rising diapir may be significantly strained if its viscosity is low relative to the diapir-hosting wallrock, or it may be minimally strained if its viscosity is similar to or greater than the diapir-hosting wallrock (Dixon, 1975). The former case with a low-diapir viscosity would result in a more extreme, mushroom head diapir geometry (Dixon, 1975). Therefore, we envision that a diapiric gneiss dome is more like the latter case with equivalent diapir-wallrock viscosities because magmatic plutons, which undoubtedly would have a larger viscosity contrast than a gneiss dome, do not result in complex mushroom-head-like geometries (Dixon, 1975).

The rising diapir neck may experience constrictional strain but the top and flanks of the diapir are predicted to experience flattening (Figs. 19C,D). The experiments of Cruden (1988) show that the tops and flanks of a rising diapirism would experience flattening to plane strain with significant rotational strain (e.g., general- to simple-shear), whereas the regions beneath the rising diapir should experience constrictional strain (Fig. 19E). The domains of constrictional strain may be overprinted by vertical shortening as the diapir rises.

With these strain characteristics in mind, we can compare deformation and structural features of the North American MCCs to predicted strain paths. A diapir will stall in the mid-upper crust, and thus require later brittle fault structures to be exhumed to the surface. Depending on erosion and exposure level, a natural buoyant diapir is most likely exposing the upper flanks of the diapir system. The North American MCCs experienced severe vertical shortening and flattening, as evidenced by the attenuated wallrock (Fig. 8) and kinematic vorticity number studies (e.g., Levy et al., 2023; Zuza et al., 2024). The simple-shear component of MCC shear zones reflects the rotational strains as predicted by the Cruden (1988) models (green field in Fig. 19E). The infrastructure of the MCCs may be mostly unexposed (i.e., the northern Snake Range), relatively undeformed (e.g., Catalina), or variably deformed and undeformed (e.g., the REHR). In the REHR, Oligocene granites are strongly sheared in the main mylonitic shear zone at structurally high levels, but at depth below the mylonite zone undeformed Oligocene granites crosscut fabrics (Fig. 20). Similarly, in Catalina, the Eocene Wilderness granite is foliated and deformed at structurally high levels in the Windy Point shear zone, but at deeper structural levels the granite is entirely undeformed (Fig. 20) (Davis et al., 2019). These strain distributions are consistent with a diapiric MCC (Figs. 19 and 20). The down-dip shear zone model (Fig. 3A.1) could also produce such a strain distribution with undeformed rocks beneath the mylonitic shear zone, but the exhumed mid-crust shear zone model

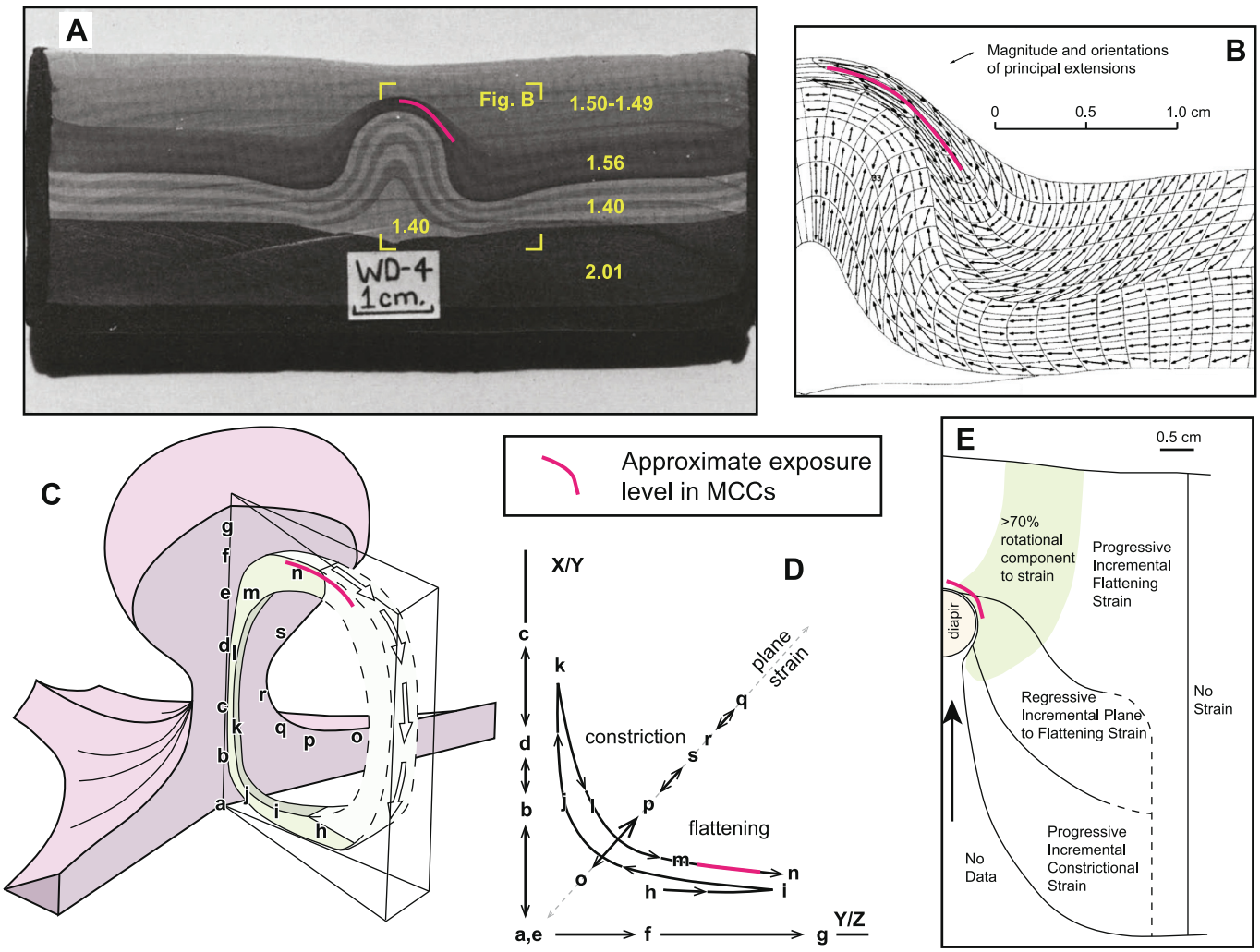

Fig. 19. Strain characteristics of a buoyant diapir. (A) Analog centrifuge experiment of a diapir from Dixon (1975). Yellow text shows density (g/cm^3) of model layers. (B) Interpreted orientations and relative magnitudes of principal extension axes from the experiment in A, from Dixon (1975). (C) Sketch of a salt diapir modified from Talbot and Jackson (1987). (D) Flinn diagram of different position within a salt diapir showing variety of strain characteristics. Letters correspond to locations in panel C. Modified from Talbot and Jackson (1987). (E) Map of strains around a diapir analog experiment. Modified from Cruden (1988). In panels A-E, the red line represents the approximate exposure level of a hypothetical gneiss-dome MCC. (For interpretation of the references to colour in this figure legend, the reader is referred to the web version of this article.)

(Fig. 3A.2) and sub-LDT distributed shear-zone model of Cooper et al. (2017) (Fig. 3A.3) suggest the presence of high-strain fabrics beneath the MCC mylonites, which is not always observed (Fig. 20).

Steep fabrics and lineations within an infrastructure, observed sub-domes, and cascading or "mushroom" folds have been used as evidence to support diapirism in the Aegean region (Kruckenberg et al., 2011) and Papua New Guinea (Little et al., 2011). Such structures are not observed within most of the central and southern North American MCCs discussed in this synthesis, but they are observed in the northern MCCs of southwest Canada-northwest USA (e.g., Kruckenberg et al., 2008). However, depending on the viscosity and melt history of a rising diapir, such intra-diapir strains are not required (e.g., Naylor, 1969) (e.g., Fig. 18). A greater volume of melt, or degree of melting, and reduced viscosity may explain why some gneiss domes experience more complex strains within the hypothesized diapir head (Dixon, 1975). However, we note that variable exposures of differing structural levels may obscure such geometry relationships.

5.5. *Different MCC relationships formed via a common mechanism*

In this review, we have emphasized our interpretation that all of the Cordilleran MCCs were generated via a common mechanism, and any differences between MCC systems reflects differential exhumation. As an example, let us consider the REHR and Snake Range MCCs, which are located ~200 km apart (Fig. 6). The REHR exposes a complex record of Mesozoic-Cenozoic plutonism, with voluminous Jurassic, Late Cretaceous, Eocene, and Oligocene igneous rocks, in combination with complex recumbent fold nappes in Ruby Mountains (Fig. 9A) (e.g., Howard, 1980). Conversely, the Snake Range exposes comparatively little igneous rocks, with the exception of local Jurassic and Cretaceous plutons. The REHR exposes rocks structurally above and below the mylonities, whereas the Snake Range exposes rocks within or above the mylonites (Fig. 5) (Wrobel et al., 2021; Long et al., 2024). Additionally, the REHR mylonites and detachment faults have top-west kinematics, whereas the Snake Range mylonites and faults show top-east kinematics.

These significant differences between adjacent MCCs can be explained by, and may provide indirect support for, buoyant doming models for MCC generation. We envision that each MCC dome may have exhumed and stalled to subtlety different vertical positions within the crust. Later detachment faulting reactivated the flanks of these emplaced buoyant domes to further exhume the footwall rocks. In the REHR, this integrated exhumation history exposed pervasively intruded lower plate

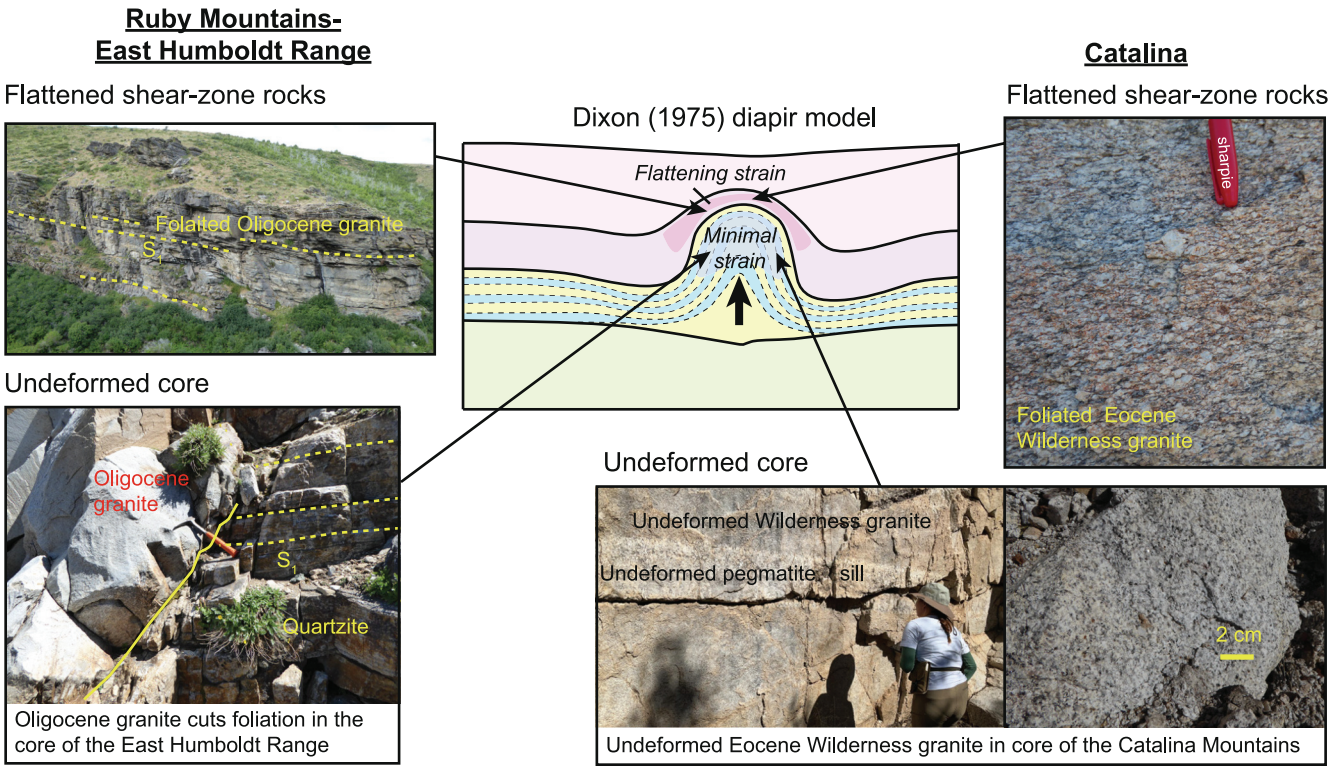

Fig. 20. Examples for how structurally higher rocks are flattened and structurally deeper rocks are undeformed within the REHR and Catalina MCCs, consistent with the Dixon (1975) strain characteristics. REHR photographs modified from Zuza et al. (2022b).

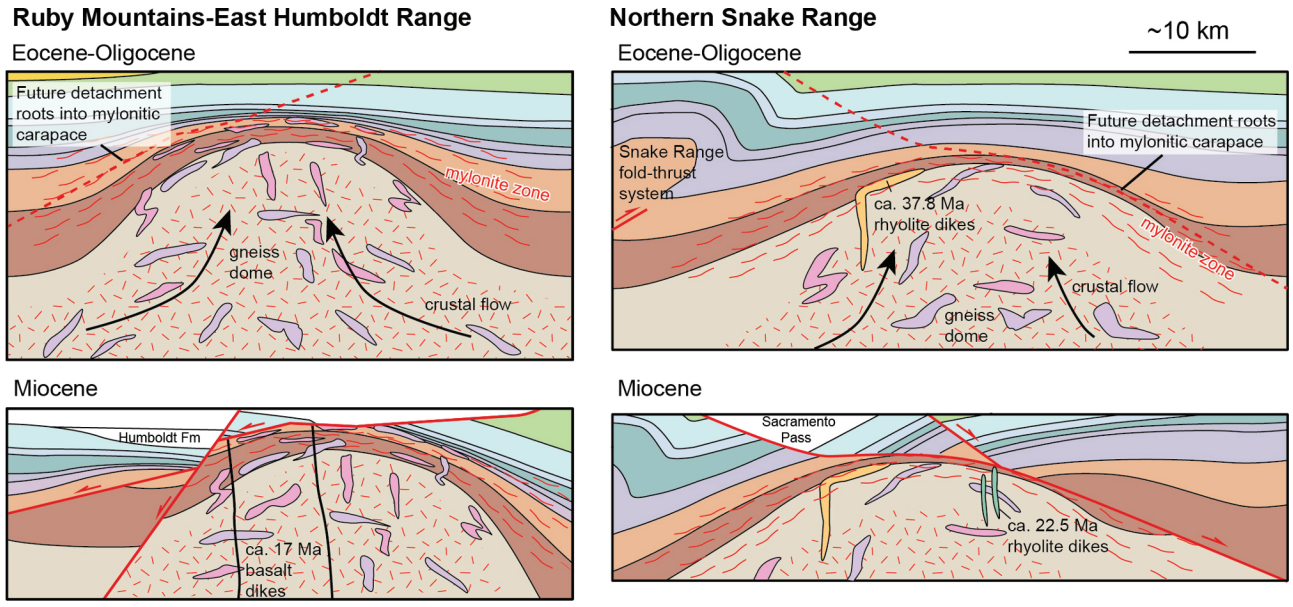

Fig. 21. Example how subtly different exhumation magnitudes and exposure levels can result in different observed geology at the surface. If the Ruby Mountains-East Humboldt Range and northern Snake Range MCC formed via similar buoyant dome processes, different exhumation during normal faulting and erosion can explain their differences in the observed geology. Namely, the Ruby Mountains-East Humboldt Range expose more plutonic and magmatic rocks, whereas the northern Snake Range does not and primarily exposes highly sheared Neoproterozoic-Cambrian paragneiss.

rocks and recumbent fold nappes (Fig. 21). Intense glacial erosion may have further exposed these lower plate rocks (Sharp, 1942; Laabs et al., 2013). In the Snake Range, slightly less integrated exhumation exposed the highly stretched carapace of the buoyant dome, without revealing structurally deeper rocks (Fig. 21). Therefore, we would hypothesize that beneath the present exposures within the northern Snake Range should be more voluminous Cenozoic intrusions and possibly recumbent fold nappes. There are some isoclinal recumbent folds observed deep within the northern Snake Range drainages, such as in Smith Creek, which hints at the possibility for more structures beneath the present-day exposure level.

The kinematic similarity between the mylonitic shear zones and primary detachment fault is compatible with Miocene fault-related exhumation of an earlier (e.g., Oligocene) domal structure. The flanks

of such a dome would have experienced dome-up, wallrock-down kinematics. Brittle faults tend to exploit and sole into preexisting mylonitic shear zones (e.g., Davis, 2013; Zuza et al., 2022b; Zuza and Dee, 2023). Thus, a major Miocene normal fault system would preferentially localize along the mylonitic flanks of a hypothesized domal upwelling (Fig. 21). The brittle normal faulting would drive hanging wall down, footwall up kinematics, which parallel the earlier dome-up, wallrock down kinematics. Therefore, the juxtaposition of these different aged structures would be expected to have similar kinematics. As normal-fault slip progresses, the footwall rocks would rotate away from the fault, as observed in most normal-fault systems, thereby exposing deeper flanks of the buoyant dome with similar kinematics as the detachment normal fault (Fig. 21). It is harder to explain the persistent kinematic similarly of brittle and ductile structures if the mylonitic shear zones simply reflect subhorizontal crustal flow that is captured by brittle faulting (e.g., Fig. 18A).

6. Analogous exhumation systems

MCCs accommodate significant exhumation of middle-to-lower crustal rocks to be placed against a relatively colder and more brittle upper crust. Therefore, refined interpretation of MCC-involved exhumation can inform us about other processes of normal-sense exhumation; that is, younger/colder rocks juxtaposed against older/hotter rocks. Similar systems include forceful emplacement of plutons (e.g., Sylvester et al., 1978) and inferred dome-and-keel events in Early Earth history where buoyant gneiss domes upwell relative to more mafic wallrock (e.g., Van Kranendonk et al., 2002, 2004; Moore and Webb, 2013). Both of these processes involve buoyant gravitational instabilities, similar to our preferred interpretations of Cordillera MCCs.

Kinematic analysis of stretched wallrock around forcefully emplaced plutons shows significant attenuation (>75 % vertically attenuated) and general shear (i.e., a mix of pure- and simple-shear) kinematics (Sylvester et al., 1978; He et al., 2009; Zhao and Cong, 2014; Zuza et al., 2024), which is remarkably similar to some Cordilleran (Zuza et al., 2022b, 2024; Levy et al., 2023) and east Asian (Zhang et al., 2023) MCCs. Comparative analysis between MCCs and emplaced plutons suggests that hot, buoyant upwelling may drive general-shear attenuation of the flanking wallrocks. We are not aware of similar analysis from dome-and-keel terranes, but such comparisons between MCCs, dome-and-keel-, and emplaced plutons may be particularly illuminating.

Models that emphasize diapirism are typically expected to produce radial stretching lineations around the rising buoyant dome (e.g., Hyndman, 1980; Collins et al., 1998; Yin, 2004; Betka and Klepeis, 2013). However, radial lineations are rarely observed in dome-and-keel and pluton emplacement settings (e.g., Paterson et al., 1991; Kloppenburg et al., 2001; Thébaud and Rey, 2013), and most lineations within a given MCC system are unidirectional (see Fig. 5; also Kruckenberg et al., 2008, 2011; Rey et al., 2017). The subparallel nature of stretching lineations in most of these settings is a common observation used to refute buoyant doming and support regional strain driven by plate-boundary kinematics (e.g., stretching or contraction). We speculate that these observations from very different tectonic settings demonstrate that buoyant doming should not be expected to produce radial stretching lineations. This could be because an observed stretching lineation does not uniquely represent the material flow direction in a 3D vorticity field (Tikoff and Fossen, 1993, 1995; Michels et al., 2015). This topic requires more analysis, but we argue that the lack of radial lineations is not strong evidence to discount MCC diapir models.

7. Summary and working definition

We compiled known structural, sedimentological, thermochronological, and geochronological data from MCCs across the North American Cordillera (Fig. 5) to evaluate their formation mechanisms in the context of the Mesozoic-Cenozoic tectonic evolution of North America. Traditional extensional MCC models assume regional extension forms a mylonitic lower plate that is either the downdip continuation of a brittle normal fault or a mid-crust shear that is captured and exhumed by brittle fault slip. Available evidence suggests this mechanism is possible for the southern MCCs around Arizona (Fig. 5), where ductile shearing, brittle fault slip, basin sedimentation, and footwall exhumation occur on overlapping timescales (Fig. 16). However, this process is not supported for the northern and central MCCs (Fig. 5) because there is a temporal disconnect between ages for ductile shearing, brittle faulting, and basin sedimentation (Fig. 16). Furthermore, available constraints for the propagation of regional extension suggest younger Miocene deformation in the north with earlier Eocene-Oligocene MCC generation. Given these differences, we argue that the central MCCs formed via buoyant doming or they represent exhumed mid-crust channel-flow structures (Fig. 18). This interpretation is consistent with gneiss dome models developed for the northern MCCs of southwestern Canada and the northwestern USA (Fig. 2B) (e.g., Kruckenberg et al., 2008; Vanderhaeghe et al., 2003). Such buoyant diapirs would have developed with characteristic spacings as observed in the Cordillera, and the wallrock attenuation observed in MCCs is similar to forceful pluton emplacement examples. Later late Oligocene-Miocene extension across the Cordillera exhumed the MCCs at such characteristic spacings. This interpretation explains why some Miocene normal-fault systems also exhume structurally deep rocks that are not migmatitic nor mylonitic (i.e., not MCCs); large Miocene normal-fault systems may exhume whatever rocks are at ~10–15 km depths, whether that is a stalled MCC diapir or other Cordillera crust. Taken together, we prefer a model of buoyant diapirism for MCC generation but acknowledge ambiguity in this interpretation.

In light of these observations, here we propose an updated working definition for a more general metamorphic core complex:

A metamorphic core complex is a composite, usually arched or domal, feature that consists of a brittlely deformed upper plate that has been juxtaposed via a regional detachment fault against a ductilely deformed lower plate mantled by high-strain mylonitic fabrics.

The above definition does not imply or require a specific tectonic setting, stress state, or kinematic linkage between structurally higher and lower features. A composite MCC structure *should not* be defined as resulting from regional or lithosphere-scale extension (e.g., Whitney et al., 2013). Interpreted kinematics and dynamic drivers of MCCs have evolved in the past (e.g., Armstrong and Hansen, 1966; Crittenden et al., 1980), and will undoubtedly change in the future, so our proposed definition of an MCC focuses on geometric and kinematic features. In our preferred interpretation of North American MCCs, the first phase of ductile lower plate exhumation as RT instabilities may have occurred in a neutral tectonic setting, whereas the later phase of brittle detachment faulting occurred during lithospheric extension. Therefore, a significant part of the MCC evolution does not require lithospheric extension, and accordingly this broader working definition allows for more fruitful comparison and evaluation between gneiss domes and MCCs globally. For example, exhumation of the central Himalayan gneiss domes from the middle to upper crust may have occurred similarly to MCC diapirism with partial melting (e.g., Cao et al., 2022) driving buoyant diapirism (e.g., Harrison et al., 1997; Lee et al., 2004). However, the brittle exhumation mechanism of the two systems differed, with the Himalayan gneiss domes being exhumed along a large contractional antiform with erosion (e.g., Jessup et al., 2019) and the MCC diapirs exhumed via brittle detachment faulting. As a final note, whether the North American MCCs are interpreted to have formed via the combined impacts of gneiss dome diapirism with later detachment faulting or a single phase of low-angle rolling-hinge normal faulting does not change the fact that they represent the type location for an MCC (Crittenden et al., 1980) and should always be named as metamorphic core complexes.

MCCs exhume hot and deep mid-crust rocks, which impacts crustal rheology, differentiation, and cooling. They are also associated with important economic mineralization (e.g., Yang et al., 2016; Howard, 2003). Study of MCCs in North American over the past half century has

led to incredible insights into their kinematics and dynamic drivers (e.g., Snelson, 1957; Armstrong and Hansen, 1966; Crittenden et al., 1980; Whitney et al., 2013). Advancements in analytical techniques and numerical simulations have provided a wealth of new data to test and critically evaluate proposed models for their evolution, which will inevitably help us better understand lithosphere-scale processes of mass and heat transport. Continued systematic efforts to date brittle and ductile structures will allow us to make improved interpretations of MCCs globally.

Declaration of competing interest

The authors declare the following financial interests/personal relationships which may be considered as potential competing interests:

Andrew Zuza reports financial support was provided by National Science Foundation. Wenrong Cao reports was provided by National Science Foundation. Gilby Jepson reports financial support was provided by National Science Foundation. If there are other authors, they declare that they have no known competing financial interests or personal relationships that could have appeared to influence the work reported in this paper.

Acknowledgements

We thank those who have shown us critical relationships in the field or otherwise helped work out these field observations, such as Keith Howard, Art Snoke, Al McGrew, Chris Henry, Seth Dee, Drew Levy, and Chuck Thorman. A. Zuza especially thanks An Yin for exposing him to the fascinating geology of metamorphic core complexes on fieldtrips to the Whipple Mountains. We also greatly appreciate discussions with many other individuals on metamorphic core complexes that have guided our thoughts, including Sean Long, Joe Colgan, Elizabeth Miller, Jens Lundstern, George Davis, Zach Michels, Ray Fletcher, and Jon Spencer. A. Zuza thanks faculty at Zhejiang University, who hosted him on a sabbatical visit where he had informative discussions about gneiss domes (metamorphic core complexes) in east Asia. We appreciate the editorial handling of Editor Eugenio Aragon, and critical review comments from John Platt, Olivier Vanderhaeghe, and an anonymous reviewer that improved this synthesis. A. Zuza acknowledges support from the National Science Foundation Tectonics Program (EAR 1830139) and the U.S. Geological Survey STATEMAP and EDMAP programs (G16AC00186, G17AC00212, G18AC00198, G19AC00383, G20AS00006, G21AC10873, G22AC00578, G21AS00005, and G24AS00077). G. Jepson is supported by NSF EAR 2419296 and W. Cao by NSF EAR 241929.

Appendix A. Supplementary data

Supplementary data to this article can be found online at https://doi.org/10.1016/j.earscirev.2024.104987.

Data availability

Data will be made available on request.

References

Anderson, R.E., Longwell, C.R., Armstrong, R.L., Marvin, R.F., 1972. Significance of K-Ar ages of Tertiary rocks from the Lake Mead region, Nevada-Arizona. Geol. Soc. Am. Bull. 83 (2), 273–288.
Armstrong, R.L., 1968. Sevier orogenic belt in Nevada and Utah. Geol. Soc. Am. Bull. 79 (4), 429–458.
Armstrong, R.L., 1982. Cordilleran Metamorphic Core Complexes – From Arizona to Southern Canada. Annu. Rev. Earth Planet. Sci. 10, 129–154.
Armstrong, R.L., Hansen, E., 1966. Cordilleran infrastructure in the eastern Great Basin. Am. J. Sci. 264 (2), 112–127.
Armstrong, R., Ward, P., 1991. Evolving geographic patterns of Cenozoic magmatism in the North American Cordillera: the temporal and spatial association of magmatism and metamorphic core complexes. J. Geophys. Res. Solid Earth 96 (B8), 13201–13224.
Atwater, T., 1970. Implications of plate tectonics for the Cenozoic tectonic evolution of western North America. Geol. Soc. Am. Bull. 81 (12), 3513–3536.
Bachl, C.A., Miller, C.F., Miller, J.S., Faulds, J.E., 2001. Construction of a pluton: evidence from an exposed cross section of the Searchlight pluton, Eldorado Mountains, Nevada. Geol. Soc. Am. Bull. 113 (9), 1213–1228.
Barnes, C.G., Burton, B.R., Burling, T.C., Wright, J.E., Karlsson, H.R., 2001. Petrology and geochemistry of the late Eocene Harrison Pass pluton, Ruby Mountains core complex, northeastern Nevada. J. Petrol. 42 (5), 901–929.
Beaumont, C., Jamieson, R.A., Nguyen, M.H., Lee, B., 2001. Himalayan tectonics explained by extrusion of a low-viscosity crustal channel coupled to focused surface denudation. Nature 414 (6865), 738–742.
Behr, W.M., Platt, J.P., 2011. A naturally constrained stress profile through the middle crust in an extensional terrane. Earth Planet. Sci. Lett. 303 (3–4), 181–192.
Bernet, M., Garver, J.I., 2005. Fission-track analysis of detrital zircon. Rev. Mineral. Geochem. 58 (1), 205–237.
Betka, P.M., Klepeis, K.A., 2013. Three-stage evolution of lower crustal gneiss domes at Breaksea Entrance, Fiordland, New Zealand. Tectonics 32 (5), 1084–1106.
Bird, P., 1988. Formation of the Rocky Mountains, western United States: a continuum computer model. Science 239 (4847), 1501–1507.
Blackford, N.R., Long, S.P., Stout, A., Rodgers, D.W., Cooper, C.M., Kramer, K., Di Fiori, Soignard, E., 2022. Late Cretaceous upper-crustal thermal structure of the Sevier hinterland: Implications for the geodynamics of the Nevadaplano. Geosphere 18 (1), 183–210.
Brandon, M.T., Roden-Tice, M.K., Garver, J.I., 1998. Late Cenozoic exhumation of the Cascadia accretionary wedge in the Olympic Mountains, Northwest Washington State. Geol. Soc. Am. Bull. 110 (8), 985–1009.
Breitsprecher, K., Thorkelson, D.J., Groome, W.G., Dostal, J., 2003. Geochemical confirmation of the Kula-Farallon slab window beneath the Pacific Northwest in Eocene time. Geology 31 (4), 351–354.
Brown, R.L., Journeay, J.M., Lane, L.S., Murphy, D.C., Rees, C.J., 1986. Obduction, backfolding and piggyback thrusting in the metamorphic hinterland of the southeastern Canadian Cordillera. J. Struct. Geol. 8, 255–268.
Brueseke, M.E., Callicoat, J.S., Hames, W., Larson, P.B., 2014. Mid-Miocene rhyolite volcanism in northeastern Nevada: the Jarbidge Rhyolite and its relationship to the Cenozoic evolution of the northern Great Basin (USA). GSA Bull. 126 (7–8), 1047–1067.
Bryant, B., Wooden, J.L., 2008. Geology of the Northern Part of the Harcuvar Complex, West-Central Arizona. US Geological Survey.
Buck, W.R., 1988. Flexural rotation of normal faults. Tectonics 7 (5), 959–973.
Buck, W.R., 1991. Modes of continental lithospheric extension. J. Geophys. Res. Solid Earth 96 (B12), 20161–20178.
Burov, E., Jaupart, C., Guillou-Frottier, L., 2003. Ascent and emplacement of buoyant magma bodies in brittle-ductile upper crust. J. Geophys. Res. Solid Earth 108 (B4).
Bykerk-Kauffman, A., Janecke, S.U., 1987. Late Cretaceous to early Tertiary ductile deformation: Catalina-Rincon metamorphic core complex, southeastern Arizona. Geology 15 (5), 462–465.
Canada, A.S., Cassel, E.J., Smith, M.E., 2021. Geochemical Evolution of Eocene Lakes in the Nevada Hinterland of the North American Cordillera. Geochem. Geophys. Geosyst. 22 (10), e2021GC009863.
Cao, H.W., Pei, Q.M., Santosh, M., Li, G.M., Zhang, L.K., Zhang, X.F., et al., 2022. Himalayan leucogranites: a review of geochemical and isotopic characteristics, timing of formation, genesis, and rare metal mineralization. Earth Sci. Rev. 104229.
Carter, T.J., Kohn, B.P., Foster, D.A., Gleadow, A.J., Woodhead, J.D., 2006. Late-stage evolution of the Chemehuevi and Sacramento detachment faults from apatite (U-Th)/He thermochronometry—evidence for mid-Miocene accelerated slip. Geol. Soc. Am. Bull. 118 (5–6), 689–709.
Cassel, E.J., Smith, M.E., Jicha, B.R., 2018. The impact of slab rollback on Earth's surface: Uplift and extension in the hinterland of the North American Cordillera. Geophys. Res. Lett. 45 (20), 10–996.
Chapman, J.B., Ducea, M.N., DeCelles, P.G., Profeta, L., 2015. Tracking changes in crustal thickness during orogenic evolution with Sr/Y: an example from the North American Cordillera. Geology 43 (10), 919–922.
Chapman, J.B., Runyon, S.E., Shields, J.E., Lawler, B.L., Pridmore, C.J., Scoggin, S.H., et al., 2021. The North American cordilleran anatectic belt. Earth Sci. Rev. 215, 103576.
Chapman, J.B., Pridmore, C., Chamberlain, K., Haxel, G., Ducea, M., 2023. Himalayan-like crustal melting and differentiation in the southern North American Cordilleran anatectic belt during the Laramide orogeny: Coyote Mountains, Arizona. J. Petrol. 64 (10), egad075.
Chapman, J.B., Scoggin, S.H., Jepson, G., Ricketts, J.W., Schaen, A.J., Trzinski, A.E., 2024. Oligocene-Miocene exhumation of the Pinaleño metamorphic core complex, southeastern Arizona: support for magmatism and plate margin reorganization as controls on regional exhumation trends. Tectonics 43 (4), e2023TC008032.
Cheng, F., Zuza, A.V., Jolivet, M., Mulch, A., Meijer, N., Guo, Z., 2023. Linking source and sink: the timing of deposition of Paleogene syntectonic strata in Central Asia. Geology 51 (11), 1083–1088.
Colgan, J.P., Henry, C.D., 2009. Rapid middle Miocene collapse of the Mesozoic orogenic plateau in north-Central Nevada. Int. Geol. Rev. 51 (9–11), 920–961.
Colgan, J.P., Howard, K.A., Fleck, R.J., Wooden, J.L., 2010. Rapid middle Miocene extension and unroofing of the southern Ruby Mountains, Nevada. Tectonics 29 (6).
Collins, W.J., Van Kranendonk, A.M., Teyssier, C., 1998. Partial convective overturn of Archaean crust in the east Pilbara Craton, Western Australia: driving mechanisms and tectonic implications. J. Struct. Geol. 20 (9–10), 1405–1424.

Compton, R.R., 1972. Geologic Map of the Yost Quadrangle, Box Elder County, Utah, and Cassia County, Idaho, Miscellaneous Geologic Investigations, vols. map I-672. U.S. Geol. Surv, Washington, D. C.
Compton, R.R., 1975. Geologic Map of the Park Valley Quadrangle, Box Elder County, Utah and Cassia County, Idaho, Miscellaneous Investigations Series, vols. map I-873. U.S. Geol. Surv, Reston, Va.
Compton, R.R., Todd, V.R., Zartman, R.E., Naeser, C.W., 1977. Oligocene and Miocene metamorphism, folding, and low-angle faulting in northwestern Utah. Geol. Soc. Am. Bull. 88 (9), 1237–1250.
Coney, P.J., 1974. Structural analysis of the Snake Range 'Décollement,' east-central Nevada. Geol. Soc. Am. Bull. 85 (6), 973–978.
Coney, P.J., 1980. Cordilleran metamorphic core complexes: an overview. In: Crittenden Jr., M.D., Coney, P.J., Davis, G.H. (Eds.), Cordilleran Metamorphic Core Complexes: Geological Society of America Memoir, vol. 153. https://doi.org/10.1130/MEM153-p7.
Coney, P.J., Reynolds, S.J., 1977. Cordilleran benioff zones. Nature 270 (5636), 403–406.
Cooper, F.J., Platt, J.P., Anczkiewicz, R., Whitehouse, M.J., 2010. Footwall dip of a core complex detachment fault: Thermobarometric constraints from the northern Snake Range (Basin and Range, USA). J. Metamorph. Geol. 28 (9), 997–1020.
Cooper, F.J., Platt, J.P., Behr, W.M., 2017. Rheological transitions in the middle crust: insights from Cordilleran metamorphic core complexes. Solid Earth 8 (1), 199–215.
Copeland, P., Currie, C.A., Lawton, T.F., Murphy, M.A., 2017. Location, location, location: the variable lifespan of the Laramide orogeny. Geology 45 (3), 223–226.
Covington, H.R., Miller, D.M., 1983. Structural evolution of the Raft River basin, Idaho. In: Tectonic and Stratigraphic Studies in the Eastern Great Basin: Geological Society of America Memoir, 157, pp. 229–237.
Cowan, D.S., Brandon, M.T., Garver, J.I., 1997. Geological tests of hypotheses for large coastwise displacements; a critique illustrated by the Baja British Columbia controversy. Am. J. Sci. 297 (2), 117–173.
Crittenden, M.D., Coney, P.J., Davis, G.H., Davis, G.H. (Eds.), 1980. Cordilleran Metamorphic Core Complexes, vol. 153. Geological Society of America.
Crowley, J.L., Brown, R.L., Parrish, R.R., 2001. Diachronous deformation and a strain gradient beneath the Selkirk allochthon, northern Monashee complex, southeastern Canadian Cordillera. J. Struct. Geol. 23, 1103–1121.
Cruden, A.R., 1988. Deformation around a rising diapir modeled by creeping flow past a sphere. Tectonics 7 (5), 1091–1101.
Davis, G.H., 1983. Shear-zone model for the origin of metamorphic core complexes. Geology 11 (6), 342–347.
Davis, G.H., 1987. A shear-zone model for the structural evolution of metamorphic core complexes in southeastern Arizona. Geol. Soc. Lond. Spec. Publ. 28 (1), 247–266.
Davis, G.A., 1988. Rapid upward transport of mid-crustal mylonitic gneisses in the footwall of a Miocene detachment fault, Whipple Mountains, southeastern California. Geol. Rundsch. 77, 191–209.
Davis, G.H., 2013. Localization control for chlorite breccia deformation beneath Catalina detachment fault, Rincon Mountains, Tucson, Arizona. J. Struct. Geol. 50, 237–253.
Davis, G.A., Anderson, J.L., 1991. Low-angle normal faulting and rapid uplift of mid-crustal rocks in the Whipple Mountains metamorphic core complex, southeastern California; discussion and field guide. In: Geological Excursions in Southern California and Mexico(Guidebook 1991 GSA Annual Meeting). Department of Geological Sciences, San Diego State Univ, San Diego, Calif, pp. 417–446.
Davis, G.H., Coney, P.J., 1979. Geologic development of the Cordilleran metamorphic core complexes. Geology 7 (3), 120–124.
Davis, G.A., Lister, G.S., 1988. Detachment Faulting in Continental Extension; Perspectives from the Southwestern US Cordillera.
Davis, G.A., Anderson, J.L., Frost, E.G., Shackelford, T.J., 1980. Mylonitization and detachment faulting in the Whipple-Buckskin-Rawhide Mountains terrane, southeastern California and western Arizona. Geol. Soc. Am. Mem. 153, 79–130.
Davis, G.A., Anderson, J.L., Marin, D.L., Krummenacher, D., Frost, E.G., Armstrong, R.L., 1982. Geologic and geochronologic relations in the lower plate of the Whipple detachment fault, Whipple Mountains, southeastern California: A progress report. In: Mesozoic-Cenozoic Tectonic Evolution of the Colorado River Region, California, Arizona, and Nevada, April 1982, pp. 409–412.
Davis, G.A., Lister, G.S., Reynolds, S.J., 1986. Structural evolution of the Whipple and South Mountains shear zones, southwestern United States. Geology 14 (1), 7–10.
Davis, G.H., Spencer, J.E., Gehrels, G.E., 2019. Field-trip guide to the Catalina-Rincon metamorphic core complex, Tucson, Arizona. In: Pearthree, P.A. (Ed.), GSA 2019 Phoenix Field Guides: Geological Society of America Field Guide 55, pp. 1–39. https://doi.org/10.1130/2019.0055(01).
Davis, G.H., Orent, E.B., Clinkscales, C., Ferroni, F.R., Gehrels, G.E., George, S.W., Guns, K.A., Hanagan, C.E., Hughes, A., Iriondo, A., Jepson, G., Kelty, C., Krantz, R. W., Levenstein, B.M., Lingrey, S.H., Miggins, D.P., Moore, T., Portnoy, S.E., Reeher, L.J., Wang, J.W., 2023. Structural Analysis and Chronologic Constraints on Progressive Deformation within the Rincon Mountains, Arizona: Implications for Development of Metamorphic Core Complexes, vol. 222. Geological Society of America.
DeCelles, P.G., 2004. Late Jurassic to Eocene evolution of the Cordilleran thrust belt and foreland basin system, western USA. Am. J. Sci. 304 (2), 105–168.
Defant, M.J., Drummond, M.S., 1990. Derivation of some modern arc magmas by melting of young subducted lithosphere. Nature 347 (6294), 662–665.
Deng, H., Ren, J., Pang, X., Rey, P.F., McClay, K.R., Watkinson, I.M., et al., 2020. South China Sea documents the transition from wide continental rift to continental break up. Nat. Commun. 11 (1), 4583.
Dewey, J.F., 1988. Extensional collapse of orogens. Tectonics 7 (6), 1123–1139.
Dickinson, W.R., 1991. Tectonic Setting of Faulted Tertiary Strata Associated with the Catalina Core Complex in Southern Arizona.
Dickinson, W.R., 2004. Evolution of the North American Cordillera. Annu. Rev. Earth Planet. Sci. 32, 13–45.
Dickinson, W.R., Hirschberg, D.M., Pitts, G.S., Bolm, K.S., 2002. Spatial Digital Database of the Geologic Map of Catalina Core Complex and San Pedro Trough, Pima, Pinal, Gila, Graham, and Cochise Counties, Arizona (No. 2002–365). US Geological Survey.
Dixon, J.M., 1975. Finite strain and progressive deformation in models of diapiric structures. Tectonophysics 28 (1–2), 89–124.
Donelick, R.A., O'Sullivan, P.B., Ketcham, R.A., 2005. Apatite fission-track analysis. Rev. Mineral. Geochem. 58 (1), 49–94.
Dorsey, R.J., Becker, U.L.F., 1995. Evolution of a large Miocene growth structure in the upper plate of the Whipple detachment fault, northeastern Whipple Mountains, California. Basin Res. 7 (2), 151–163.
Doughty, P.T., Sheriff, S.D., 1992. Paleomagnetic evidence for en echelon crustal extension and crustal rotations in western Montana and Idaho. Tectonics 11 (3), 663–671.
Dover, J.H., 1981. Geology of the Boulder-Pioneer wilderness study area, Blaine and Custer counties, Idaho. U.S. Geol. Surv. Bull. 1497, 15–75.
Dover, J.H., 1983. Geologic Map and Sections of the Central Pioneer Mountains, Blaine and Custer Counties, central Idaho (No. 1319).s.
Drewes, H., 1974. Geologic Map and Sections of the Happy Valley Quadrangle, Cochise County, Arizona (No. 832).
Dubiel, R.F., Potter, C.J., Good, S.C., Snee, L.W., 1996. Reconstructing an Eocene extensional basin: The White Sage Formation, eastern Great Basin. In: Beratan, K.K. (Ed.), Reconstructing the History of Basin and Range Extension using Sedimentology and Stratigraphy: Geological Society of America Special Paper, 303, pp. 1–14.
Ducea, M.N., Triantafyllou, A., Krcmaric, J., 2020. New timing and depth constraints for the Catalina metamorphic core complex, Southeast Arizona. Tectonics 39 (8), e2020TC006383.
Dudas, F.O., Ispoatov, V.O., Harlan, S.S., Snee, L.W., 2010. 40Ar/39Ar geochronology and geochemical reconnaissance of the Eocene Lowland Creek volcanic fi eld, west-Central Montana. J. Geol. 118, 295–304. https://doi.org/10.1086/651523.
Egger, A.E., Dumitru, T.A., Miller, E.L., Savage, C.F., Wooden, J.L., 2003. Timing and nature of Tertiary plutonism and extension in the Grouse Creek Mountains, Utah. Int. Geol. Rev. 45 (6), 497–532.
Eskola, P.E., 1948. The problem of mantled gneiss domes. Q. J. Geol. Soc. 104 (1–4), 461–476.
Evans, S.L., Styron, R.H., van Soest, M.C., Hodges, K.V., Hanson, A.D., 2015. Zircon and apatite (U-Th)/He evidence for Paleogene and Neogene extension in the southern Snake Range, Nevada, USA. Tectonics 34 (10), 2142–2164.
Farley, K.A., 2000. Helium diffusion from apatite: General behavior as illustrated by Durango fluorapatite. J. Geophys. Res. Solid Earth 105 (B2), 2903–2914.
Faulds, J.E., Feuerbach, D.L., Miller, C.F., Smith, E.I., 2001. Cenozoic Evolution of the Northern Colorado River Extensional Corridor, Southern Nevada and Northwest Arizona.
Faulds, J.E., Olson, E.L., Harlan, S.S., McIntosh, W.C., 2002. Miocene extension and fault-related folding in the Highland Range, southern Nevada: a three-dimensional perspective. J. Struct. Geol. 24 (4), 861–886.
Favorito, D.A., Seedorff, E., 2021. Cenozoic structural evolution of the Catalina metamorphic core complex and reassembly of Laramide reverse faults, southeastern Arizona, USA. Geosphere 17 (6), 1928–1971.
Fayon, A.K., Peacock, S.M., Stump, E., Reynolds, S.J., 2000. Fission track analysis of the footwall of the Catalina detachment fault, Arizona: Tectonic denudation, magmatism, and erosion. J. Geophys. Res. Solid Earth 105 (B5), 11047–11062.
Fayon, A.K., Tikoff, B., Kahn, M., Gaschnig, R.M., 2017. Cooling and exhumation of the southern Idaho batholith. Lithosphere 9 (2), 299–314.
Fletcher, R.C., 1972. Application of a mathematical model to the emplacement of mantled gneiss domes. Am. J. Sci. 272 (3), 197–216.
Flowers, R.M., Farley, K.A., Ketcham, R.A., 2015. A reporting protocol for thermochronologic modeling illustrated with data from the Grand Canyon. Earth. Planet. Sci. Lett. 432, 425–435.
Flowers, R.M., Ketcham, R.A., Shuster, D.L., Farley, K.A., 2009. Apatite (U–Th)/He thermochronometry using a radiation damage accumulation and annealing model. Geochim. Cosmochim. Acta 73 (8), 2347–2365.
Fornash, K.F., Patchett, P.J., Gehrels, G.E., Spencer, J.E., 2013. Evolution of granitoids in the Catalina metamorphic core complex, southeastern Arizona: U–Pb, Nd, and Hf isotopic constraints. Contrib. Mineral. Petrol. 165, 1295–1310.
Forshee, E.J., Yin, A., 1994. Evolution of monolithological breccia deposits in supradetachment basins, Whipple Mountains, California. Basin Res. 7 (2), 181–197.
Fossen, H., Cavalcante, G.C.G., 2017. Shear zones–a review. Earth Sci. Rev. 171, 434–455.
Foster, D.A., John, B.E., 1999. Quantifying tectonic exhumation in an extensional orogen with thermochronology: examples from the southern Basin and Range Province. Geol. Soc. Lond. Spec. Publ. 154 (1), 343–364.
Foster, D.A., Mark Fanning, C., 1997. Geochronology of the northern Idaho batholith and the Bitterroot metamorphic core complex: Magmatism preceding and contemporaneous with extension. Geol. Soc. Am. Bull. 109 (4), 379–394.
Foster, D.A., Raza, A., 2002. Low-temperature thermochronological record of exhumation of the Bitterroot metamorphic core complex, northern Cordilleran Orogen. Tectonophysics 349 (1–4), 23–36.
Foster, D.A., Schafer, C., Fanning, C.M., Hyndman, D.W., 2001. Relationships between crustal partial melting, plutonism, orogeny, and exhumation: Idaho–Bitterroot batholith. Tectonophysics 342 (3–4), 313–350.
Foster, D.A., Harrison, T.M., Miller, C.F., Howard, K.A., 1990. The 40Ar/39Ar thermochronology of the eastern Mojave Desert, California, and adjacent western Arizona with implications for the evolution of metamorphic core complexes. Journal of Geophysical Research: Solid Earth 95 (B12), 20005–20024.

Foster, D.A., Doughty, P.T., Kalakay, T.J., Fanning, C.M., Coyner, S., Grice, W.C., Vogl, J., 2007. Kinematics and Timing of Exhumation of Metamorphic Core Complexes along the Lewis and Clark Fault Zone, Northern Rocky Mountains, USA.
Foster, D.A., Grice Jr., W.C., Kalakay, T.J., 2010. Extension of the Anaconda metamorphic core complex: 40Ar/39Ar thermochronology and implications for Eocene tectonics of the northern Rocky Mountains and the Boulder batholith. Lithosphere 2 (4), 232–246.
Friedmann, S.J., Burbank, D.W., 1995. Rift basins and supradetachment basins: Intracontinental extensional end-members. Basin Res. 7 (2), 109–127.
Fuston, S., Wu, J., 2021. Raising the Resurrection plate from an unfolded-slab plate tectonic reconstruction of northwestern North America since early Cenozoic time. GSA Bull. 133 (5–6), 1128–1140.
Gallagher, K., 2012. Transdimensional inverse thermal history modeling for quantitative thermochronology. J. Geophys. Res. Solid Earth 117 (B2).
Gans, P.B., 1987. An open-system, two-layer crustal stretching model for the eastern Great Basin. Tectonics 6 (1), 1–12.
Gans, P.B., Bohrson, W.A., 1998. Suppression of volcanism during rapid extension in the Basin and Range Province, United States. Science 279 (5347), 66–68.
Gans, P.B., Gentry, B.J., 2016. Dike emplacement, footwall rotation, and the transition from magmatic to tectonic extension in the Whipple Mountains metamorphic core complex, southeastern California. Tectonics 35 (11), 2564–2608.
Gans, P.B., Mahood, G.A., Schermer, E., 1989. Synextensional Magmatism in the Basin and Range Province: A Case Study from the Eastern Great Basin, vol. 233. Geological Society of America, p. 53.
Garmezy, L., 1983. Geology and Geochronology of the Southeast Border of the Bitterroot Dome: Implications for the Structural Evolution of the Mylonite Carapace. PhD dissertation,. Pennsylvania State University, University Park, Pennsylvania.
Gaschnig, R.M., Vervoort, J.D., Lewis, R.S., McClelland, W.C., 2010. Migrating magmatism in the northern US Cordillera: in situ U–Pb geochronology of the Idaho batholith. Contrib. Mineral. Petrol. 159, 863–883.
Gaschnig, R.M., Vervoort, J.D., Lewis, R.S., Tikoff, B., 2011. Isotopic evolution of the Idaho batholith and Challis intrusive province, northern US Cordillera. J. Petrol. 52 (12), 2397–2429.
Gébelin, A., Mulch, A., Teyssier, C., Heizler, M., Vennemann, T., Seaton, N.C., 2011. Oligo-Miocene extensional tectonics and fluid flow across the Northern Snake Range detachment system, Nevada. Tectonics 30 (5).
Gébelin, A., Mulch, A., Teyssier, C., Chamberlain, C.P., Heizler, M., 2012. Coupled basin-detachment systems as paleoaltimetry archives of the western North American Cordillera. Earth Planet. Sci. Lett. 335, 36–47.
Gébelin, A., Teyssier, C., Heizler, M.T., Mulch, A., 2015. Meteoric water circulation in a rolling-hinge detachment system (northern Snake Range core complex, Nevada). Bulletin 127 (1–2), 149–161.
Gordon, S.M., Whitney, D.L., Teyssier, C., Grove, M., Dunlap, W.J., 2008. Timescales of migmatization, melt crystallization, and cooling in a Cordilleran gneiss dome: Valhalla complex, southeastern British Columbia. Tectonics 27 (4).
Gottardi, R., Teyssier, C., 2013. Thermomechanics of an extensional shear zone, Raft River metamorphic core complex, NW Utah. J. Struct. Geol. 53, 54–69.
Gottardi, R., McAleer, R., Casale, G., Borel, M., Iriondo, A., Jepson, G., 2020. Exhumation of the Coyote Mountains metamorphic core complex (Arizona): Implications for orogenic collapse of the southern North American Cordillera. Tectonics 39 (8), e2019TC006050.
Gottardi, R., Teyssier, C., Mulch, A., Valley, J.W., Spicuzza, M.J., Vennemann, T.W., Quilichini, A., Heizler, M., 2015. Strain and permeability gradients traced by stable isotope exchange in the Raft River detachment shear zone, Utah. J. Struct. Geol. 71, 41–57.
Grice Jr., W.C., 2006. Exhumation and Cooling History of the Middle Eocene Anaconda Metamorphic Core Complex, Western Montana [M.Sc. thesis]. University of Florida, Gainesville, 261 p.
Grier, S., 1983. Tertiary stratigraphy and geologic history of the Sacramento Pass Area, Nevada. In: Geol. Soc. Am., Rocky Mountain and Cordilleran Sections Meeting, Utah Geol. And Mineral Survey Spec. Studies, 59, pp. 139–144.
Guenthner, W.R., Reiners, P.W., Ketcham, R.A., Nasdala, L., Giester, G., 2013. Helium diffusion in natural zircon: Radiation damage, anisotropy, and the interpretation of zircon (U-Th)/He thermochronology. Am. J. Sci. 313, 145–198.
Hacker, B.R., Yin, A., Christie, J.M., Snoke, A.W., 1990. Differential stress, strain rate, and temperatures of mylonitization in the Ruby Mountains, Nevada: implications for the rate and duration of uplift. J. Geophys. Res. Solid Earth 95 (B6), 8569–8580.
Haines, S.H., van der Pluijm, B.A., 2010. Dating the detachment fault system of the Ruby Mountains, Nevada: significance for the kinematics of low-angle normal faults. Tectonics 29 (4).
Hallett, B.W., Spear, F.S., 2014. The P–T history of anatectic pelites of the Northern East Humboldt Range, Nevada: Evidence for tectonic loading, decompression, and anatexis. J. Petrol. 55 (1), 3–36.
Hallett, B.W., Spear, F.S., 2015. Monazite, zircon, and garnet growth in migmatitic pelites as a record of metamorphism and partial melting in the East Humboldt Range, Nevada. Am. Mineral. 100 (4), 951–972.
Haney, E., 2008. Pressure-Temperature Evolution of Metapelites within the Anaconda Metamorphic Core Complex, Southwestern Montana.
Harrison, T.M., Duncan, I.A.N., Mcdougall, I.A.N., 1985. Diffusion of ^{40}Ar in biotite: temperature, pressure and compositional effects. Geochim. Cosmochim. Acta 49 (11), 2461–2468.
Harrison, T.M., Lovera, O.M., Grove, M., 1997. New insights into the origin of two contrasting Himalayan granite belts. Geology 25 (10), 899–902.
Harrison, T.M., Célérier, J., Aikman, A.B., Hermann, J., Heizler, M.T., 2009. Diffusion of ^{40}Ar in muscovite. Geochim. Cosmochim. Acta 73 (4), 1039–1051.
Haynes, S.R., 2003. Development of the Eocene Elko Basin, Northeastern Nevada: Implications for Paleogeography and Regional Tectonism. Doctoral dissertation. University of British Columbia.
He, B., Xu, Y.G., Paterson, S., 2009. Magmatic diapirism of the Fangshan pluton, southwest of Beijing, China. J. Struct. Geol. 31 (6), 615–626.
Henry, C.D., 2008. Ash-flow tuffs and paleovalleys in northeastern Nevada: Implications for Eocene paleogeography and extension in the Sevier hinterland, northern Great Basin. Geosphere 4 (1), 1–35.
Henry, C., 2018. The Eocene Elko Basin and Elko Formation, NE Nevada: Paleotopographic controls on area, thickness, facies distribution, and petroleum potential. In: AAPG ACE 2018.
Henry, C.D., Hinz, N.H., Faulds, J.E., Colgan, J.P., John, D.A., Brooks, E.R., et al., 2012. Eocene–Early Miocene paleotopography of the Sierra Nevada–Great Basin–Nevadaplano based on widespread ash-flow tuffs and paleovalleys. Geosphere 8 (1), 1–27.
Henry, C., Heizler, M.T., Zuza, A.V., Dee, S., Levy, D., 2023. Detrital sanidine populations indicate probable Middle Miocene extension, uplift, and exposure of the Ruby Mountains-East Humboldt metamorphic core complex, Northeast Nevada, USA. Geol. Soc. Am. Abstr. Programs 55 (6).
Hodges, K.V., Snoke, A.W., Hurlow, H.A., 1992. Thermal evolution of a portion of the Sevier hinterland: the northern Ruby Mountains-East Humboldt range and Wood Hills, northeastern Nevada. Tectonics 11 (1), 154–164.
Hoiland, C., Hourigan, J., Miller, E., 2022. Evidence for large departures from lithostatic pressure during Late Cretaceous metamorphism in the northern Snake Range metamorphic core complex, Nevada. In: Craddock, J.P., Malone, D.H., Foreman, B. Z., Konstantinou, A. (Eds.), Tectonic Evolution of the Sevier-Laramide Hinterland, Thrust Belt, and Foreland, and Postorogenic Slab Rollback (180–20 Ma). Geological Society of America Special Paper 555.
House, M.A., Hodges, K.V., 1994. Limits on the tectonic significance of rapid cooling events in extensional settings: Insights from the Bitterroot metamorphic core complex, Idaho-Montana. Geology 22 (11), 1007–1010.
Houseman, G.A., McKenzie, D.P., Molnar, P., 1981. Convective instability of a thickened boundary layer and its relevance for the thermal evolution of continental convergent belts. J. Geophys. Res. Solid Earth 86 (B7), 6115–6132.
Howard, K.A., 1980. Metamorphic infrastructure in the northern Ruby Mountains, Nevada. Geol. Soc. America Memoirs 153, 335–348.
Howard, K.A., 2003. Crustal structure in the Elko-Carlin region, Nevada, during Eocene gold mineralization: Ruby-East Humboldt metamorphic core complex as a guide to the deep crust. Econ. Geol. 98 (2), 249–268.
Howard, K.A., John, B.E., 1987. Crustal extension along a rooted system of imbricate low-angle faults: Colorado River extensional corridor, California and Arizona. Geol. Soc. Lond. Spec. Publ. 28 (1), 299–311.
Howard, K.A., Kistler, R.W., Snoke, A.W., Willden, R., 1979. Geologic map of the Ruby Mountains, Nevada. U.S. Geol. Surv. Misc. Invest. Ser. Map I-1136 (scale 1:125,000).
Howard, K.A., Wooden, J.L., Barnes, C.G., Premo, W.R., Snoke, A.W., Lee, S.Y., 2011. Episodic growth of a Late Cretaceous and Paleogene intrusive complex of pegmatitic leucogranite, Ruby Mountains core complex, Nevada, USA. Geosphere 7 (5), 1220–1248.
Howlett, C.J., Reynolds, A.N., Laskowski, A.K., 2021. Magmatism and extension in the Anaconda metamorphic core complex of western Montana and relation to regional tectonics. Tectonics 40 (9), e2020TC006431.
Hubbard, J., Shaw, J.H., 2009. Uplift of the Longmen Shan and Tibetan plateau, and the 2008 Wenchuan (M= 7.9) earthquake. Nature 458 (7235), 194–197.
Humphreys, E.D., 1995. Post-Laramide removal of the Farallon slab, western United States. Geology 23 (11), 987–990.
Humphreys, E., Hessler, E., Dueker, K., Farmer, G.L., Erslev, E., Atwater, T., 2003. How Laramide-age hydration of North American lithosphere by the Farallon slab controlled subsequent activity in the western United States. Int. Geol. Rev. 45 (7), 575–595.
Hurford, A.J., 1986. Cooling and uplift patterns in the Lepontine Alps South Central Switzerland and an age of vertical movement on the Insubric fault line. Contrib. Mineral. Petrol. 92 (4), 413–427.
Hurlow, H.A., 1987. Structural Geometry, Fabric, and Chronology of a Tertiary Extensional Shear Zone-Detachment System, Southwestern East Humboldt Range, Elko County, Nevada. University of Wyoming.
Hurlow, H.A., Snoke, A.W., Hodges, K.V., 1991. Temperature and pressure of mylonitization in a Tertiary extensional shear zone, Ruby Mountains-East Humboldt Range, Nevada: Tectonic implications. Geology 19 (1), 82–86.
Hyndman, D.W., 1980. Bitterroot dome-Sapphire tectonic block, an example of a plutonic-core gneiss-dome complex with its detached suprastructure. In: Cordilleran Metamorphic Core Complexes: Geological Society of America Memoir, 153, pp. 427–443.
Hyndman, R.D., Currie, C.A., 2011. Why is the North America Cordillera high? Hot backarcs, thermal isostasy, and mountain belts. Geology 39 (8), 783–786.
Hyndman, D.W., Myers, S.A., 1988. The transition from amphibolite-facies mylonite to chloritic breccia and role of the mylonite in formation of Eocene epizonal plutons, Bitterroot dome, Montana. Geol. Rundsch. 77, 211–226.
Ingersoll, R.V., 1982. Triple-junction instability as cause for late Cenozoic extension and fragmentation of the western United States. Geology 10 (12), 621–624.
Irving, E., Woodsworth, G.J., Wynne, P.J., Morrison, A., 1985. Paleomagnetic evidence for displacement from the south of the Coast Plutonic complex, British Columbia. Can. J. Earth Sci. 22 (4), 584–598.
Issler, D., McQueen, H., Beaumont, C., 1989. Thermal and isostatic consequences of simple shear extension of the continental lithosphere. Earth Planet. Sci. Lett. 91 (3–4), 341–358.

Jackson, M.P.A., Talbot, C.J., 1989. Anatomy of mushroom-shaped diapirs. J. Struct. Geol. 11 (1–2), 211–230.
Jaramillo, V., Catlos, E., Bell, E., Stockli, D.F., Schmitt, A.K., Chin, E.J., Yin, A., 2022. Superposition of 80–55 Ma high *P-T* (0.7 GPa/750 °C) metamorphism by mid-Tertiary detachment faulting in the Whipple Mountains, SE California. Geol. Soc. Am. Abstr. Programs 54 (5). https://doi.org/10.1130/abs/2022AM-378171.
Jepson, G., Carrapa, B., George, S.W., Triantafyllou, A., Egan, S.M., Constenius, K.N., et al., 2021. Resolving mid-to upper-crustal exhumation through apatite petrochronology and thermochronology. Chem. Geol. 565, 120071.
Jepson, G., Carrapa, B., George, S.W., Reeher, L.J., Kapp, P.A., Davis, G.H., et al., 2022. Where did the Arizona-Plano go? Protracted thinning via upper-to lower-crustal processes. J. Geophys. Res. Solid Earth 127 (4), e2021JB023850.
Jessup, M.J., Langille, J.M., Diedesch, T.F., Cottle, J.M., 2019. Gneiss dome formation in the Himalaya and southern Tibet. Geol. Soc. Lond. Spec. Publ. 483 (1), 401–422.
Ji, W., Faure, M., Lin, W., Chen, Y., Chu, Y., Xue, Z., 2018. Multiple emplacement and exhumation history of the Late Mesozoic Dayunshan–Mufushan batholith in southeast China and its tectonic significance: 1. Structural analysis and geochronological constraints. J. Geophys. Res. Solid Earth 123 (1), 689–710.
Jödicke, H., Jording, A., Ferrari, L., Arzate, J., Mezger, K., Rüpke, L., 2006. Fluid release from the subducted Cocos plate and partial melting of the crust deduced from magnetotelluric studies in southern Mexico: Implications for the generation of volcanism and subduction dynamics. J. Geophys. Res. Solid Earth 111 (B8).
John, B.E., 1982. Geologic framework of the Chemehuevi Mountains, southeastern California. In: Mesozoic-Cenozoic Tectonic Evolution of the Colorado River region, California, Arizona, and Nevada. Cordilleran Publishers, San Diego, California, pp. 317–325.
John, B.E., 1987. Geometry and evolution of a mid-crustal extensional fault system: Chemehuevi Mountains, southeastern California. Geol. Soc. Lond. Spec. Publ. 28 (1), 313–335.
John, B.E., Foster, D.A., 1993. Structural and thermal constraints on the initiation angle of detachment faulting in the southern Basin and Range: the Chemehuevi Mountains case study. Geol. Soc. Am. Bull. 105 (8), 1091–1108.
John, B.E., Mukasa, S.B., 1990. Footwall rocks to the Mid-Tertiary Chemehuevi Detachment Fault: a window into the middle crust in the Southern Cordillera. J. Geophys. Res. Solid Earth 95 (B1), 463–485.
Jolivet, L., Brun, J.P., 2010. Cenozoic geodynamic evolution of the Aegean. Int. J. Earth Sci. 99, 109–138.
Jolivet, L., Faccenna, C., Huet, B., Labrousse, L., Le Pourhiet, L., Lacombe, O., et al., 2013. Aegean tectonics: Strain localisation, slab tearing and trench retreat. Tectonophysics 597, 1–33.
Jolivet, L., Sautter, V., Moretti, I., Vettor, T., Papadopoulou, Z., Augier, R., et al., 2021. Anatomy and evolution of a migmatite-cored extensional metamorphic dome and interaction with syn-kinematic intrusions, the Mykonos-Delos-Rheneia MCC. J. Geodyn. 144, 101824.
Jones, C.H., Sonder, L.J., Unruh, J.R., 1998. Lithospheric gravitational potential energy and past orogenesis: Implications for conditions of initial Basin and Range and Laramide deformation. Geology 26 (7), 639–642.
Kaare-Rasmussen, J., Horton, F., Holder, R., Kylander-Clark, A., Bouvier, A., Müntener, O., Rakotondrazafy, M., 2024. Protracted mantle heat conduction after lithospheric foundering beneath the Malagasy orogen. Geology.
Kalakay, T.J., Foster, D.A., Lonn, J.D., 2014. Polyphase Collapse of the Cordilleran Hinterland: The Anaconda Metamorphic Core Complex of Western Montana—The Snoke Symposium Field Trip.
Kapp, J.D.A., Miller, C.F., Miller, J.S., 2002. Ireteba pluton, Eldorado Mountains, Nevada: late, deep-source, peraluminous magmatism in the Cordilleran Interior. J. Geol. 110 (6), 649–669.
Kapp, P., Jepson, G., Carrapa, B., Schaen, A.J., He, J.J., Wang, J.W., 2023. Laramide bulldozing of lithosphere beneath the Arizona transition zone, southwestern United States. Geology 51 (10), 952–956.
Keith, S.B., Reynolds, S.J., Damon, P.E., Shafiqullah, M., Livingston, D.E., Pushkar, P.D., 1980. Evidence for multiple intrusion and deformation within the Santa Catalina-Rincon-Tortolita crystalline complex, southeastern Arizona. Geol. Soc. Am. Mem. 153, 217–267.
Kelly, E.D., Hoisch, T.D., Wells, M.L., Vervoort, J.D., Beyene, M.A., 2015. An early cretaceous garnet pressure–temperature path recording synconvergent burial and exhumation from the hinterland of the Sevier orogenic belt, Albion Mountains, Idaho. Contrib. Mineral. Petrol. 170, 1–22.
Ketcham, R.A., Carter, A., Donelick, R.A., Barbarand, J., Hurford, A.J., 2007. Improved modeling of fission-track annealing in apatite. Am. Mineral. 92 (5–6), 799–810.
Kloppenburg, A., White, S.H., Zegers, T.E., 2001. Structural evolution of the Warrawoona Greenstone Belt and adjoining granitoid complexes, Pilbara Craton, Australia: implications for Archaean tectonic processes. Precambrian Res. 112 (1–2), 107–147.
Konstantinou, A., Strickland, A., Miller, E.L., Wooden, J.P., 2012. Multistage Cenozoic extension of the Albion–Raft River–Grouse Creek metamorphic core complex: Geochronologic and stratigraphic constraints. Geosphere 8 (6), 1429–1466.
Konstantinou, A., Strickland, A., Miller, E., Vervoort, J., Fisher, C.M., Wooden, J., Valley, J., 2013. Synextensional magmatism leading to crustal flow in the Albion–Raft River–Grouse Creek metamorphic core complex, northeastern Basin and Range. Tectonics 32 (5), 1384–1403.
Krijgsman, W., Tauxe, L., 2006. E/I corrected paleolatitudes for the sedimentary rocks of the Baja British Columbia hypothesis. Earth Planet. Sci. Lett. 242 (1–2), 205–216.
Kruckenberg, S.C., Whitney, D.L., Teyssier, C., Fanning, C.M., Dunlap, W.J., 2008. Paleocene-Eocene migmatite crystallization, extension, and exhumation in the hinterland of the northern Cordillera: Okanogan dome, Washington, USA. Geol. Soc. Am. Bull. 120 (7–8), 912–929.
Kruckenberg, S.C., Vanderhaeghe, O., Ferré, E.C., Teyssier, C., Whitney, D.L., 2011. Flow of partially molten crust and the internal dynamics of a migmatite dome, Naxos, Greece. Tectonics 30 (3).
Kruse, S., McNutt, M., Phipps-Morgan, J., Royden, L., Wernicke, B., 1991. Lithospheric extension near Lake Mead, Nevada: a model for ductile flow in the lower crust. J. Geophys. Res. Solid Earth 96 (B3), 4435–4456.
Laabs, B.J., Munroe, J.S., Best, L.C., Caffee, M.W., 2013. Timing of the last glaciation and subsequent deglaciation in the Ruby Mountains, Great Basin, USA. Earth Planet. Sci. Lett. 361, 16–25.
LaForge, J.S., John, B.E., Grimes, C.B., 2017. Synextensional dike emplacement across the footwall of a continental core complex, Chemehuevi Mountains, southeastern California. Geosphere 13 (6), 1867–1886.
LaTour, T.E., Barnett, R.L., 1987. Mineralogical changes accompanying mylonitization in the Bitterroot dome of the Idaho batholith: Implications for timing of deformation. Geol. Soc. Am. Bull. 98 (3), 356–363.
Lee, J., Sutter, J.F., 1991. Incremental 40Ar/39Ar thermochronology of mylonitic rocks from the northern Snake Range, Nevada. Tectonics 10 (1), 77–100.
Lee, J., Miller, E.L., Sutter, J.F., 1987. Ductile strain and metamorphism in an extensional tectonic setting: a case study from the northern Snake Range, Nevada, USA. Geol. Soc. Lond. Spec. Publ. 28 (1), 267–298.
Lee, S.Y., Barnes, C.G., Snoke, A.W., Howard, K.A., Frost, C.D., 2003. Petrogenesis of Mesozoic, peraluminous granites in the Lamoille Canyon area, Ruby Mountains, Nevada, USA. J. Petrol. 44 (4), 713–732.
Lee, J., Hacker, B., Wang, Y., 2004. Evolution of North Himalayan gneiss domes: structural and metamorphic studies in Mabja Dome, southern Tibet. J. Struct. Geol. 26 (12), 2297–2316.
Lee, J., Blackburn, T., Johnston, S., 2017. Timing of mid-crustal ductile extension in the northern Snake Range metamorphic core complex, Nevada: evidence from U/Pb zircon ages. Geosphere 13 (2), 439–459.
Lee, T., Sihpol, T., Zuza, A.V., Odlum, M., 2024. Investigating the deformation timing and kinematics of the mylonitic shear zone in the North American Cordilleran metamorphic core complexes. In: GSA Connects Fall Meeting.
Lenardic, A., Moresi, L., Mühlhaus, H., 2000. The role of mobile belts for the longevity of deep cratonic lithosphere: the crumple zone model. Geophys. Res. Lett. 27 (8), 1235–1238.
Levy, D.A., Zuza, A.V., Michels, Z.D., DesOrmeau, J.W., 2023. Buoyant doming generates metamorphic core complexes in the North American Cordillera. Geology 51 (3), 290–294.
Lewis, C.J., Wernicke, B.P., Selverstone, J., Bartley, J.M., 1999. Deep burial of the footwall of the northern Snake Range decollement, Nevada. Geol. Soc. Am. Bull. 111 (1), 39–51.
Li, Z.X., 2015. Paleogeographic record of Eocene Farallon slab rollback beneath western North America: COMMENT. Geology 43 (4), e362.
Li, Z.X., Li, X.H., 2007. Formation of the 1300-km-wide intracontinental orogen and postorogenic magmatic province in Mesozoic South China: a flat-slab subduction model. Geology 35 (2), 179–182.
Link, P.K., Durk, K.M., Fanning, C.M., 2007, October. SHRIMP U-Pb ages from Archean orthogneiss, Mesoproterozoic paragneiss and Eocene Boulder Creek Pluton, Pioneer Mountains, south-central Idaho, part of the 2600 Ma Grouse Creek block. In: Geological Society of America, Abstracts with Programs, vol. 39, p. 613.
Link, P.K., Cameron, A., Autenrieth-Durk, K., 2010, October. Tectonostratigraphy of the Wildhorse gneiss complex, Pioneer Mountains: Neoarchean orthogneiss and overlying Mesoproterozoic Lemhi Group overlie Albion Range Proterozoic quartzite. In: Geological Society of America, Abstracts with Programs, vol. 42, p. 415. No. 5.
Lister, G.S., Davis, G.A., 1989. The origin of metamorphic core complexes and detachment faults formed during Tertiary continental extension in the northern Colorado River region, USA. J. Struct. Geol. 11 (1–2), 65–94.
Lister, G.S., Snoke, A.W., 1984. SC mylonites. J. Struct. Geol. 6 (6), 617–638.
Little, T.A., Hacker, B.R., Gordon, S.M., Baldwin, S.L., Fitzgerald, P.G., Ellis, S., Korchinski, M., 2011. Diapiric exhumation of Earth's youngest (UHP) eclogites in the gneiss domes of the D'Entrecasteaux Islands, Papua New Guinea. Tectonophysics 510 (1–2), 39–68.
Liu, S., Currie, C.A., 2016. Farallon plate dynamics prior to the Laramide orogeny: Numerical models of flat subduction. Tectonophysics 666, 33–47.
Long, S.P., Lee, J., Blackford, N.R., 2023. Extreme ductile thinning of Cambrian marbles in the Northern Snake Range metamorphic core complex, Nevada, USA: Implications for extension magnitude and structural evolution. J. Struct. Geol. 173, 104912.
Long, S.P., Walker, J.P., 2015. Geometry and kinematics of the Grant Range brittle detachment system, eastern Nevada, USA: an end-member style of upper crustal extension. Tectonics 34 (9), 1837–1862.
Long, S.P., Lee, J., Blackford, N.R., 2022. The low-angle breakaway system for the Northern Snake Range décollement in the Schell Creek and Duck Creek Ranges, eastern Nevada, USA: Implications for displacement magnitude. Geosphere 18 (4), 1194–1222.
Long, S.P., Blackford, N.R., Lee, J., Soignard, E., 2024. Crustal thermal architecture, structural reconstructions, field relationships, and geophysical data rule out deep structural burial of the footwall of the Northern Snake Range metamorphic core complex (Nevada, USA). Tectonics 43 (10), e2024TC008368.
Louis-Napoléon, A., Gerbault, M., Bonometti, T., Thieulot, C., Martin, R., Vanderhaeghe, O., 2020. 3-D numerical modelling of crustal polydiapirs with volume-of-fluid methods. Geophys. J. Int. 222 (1), 474–506.
Louis-Napoléon, A., Bonometti, T., Gerbault, M., Martin, R., Vanderhaeghe, O., 2022. Models of convection and segregation in heterogeneous partially molten crustal roots with a VOF method–I: flow regimes. Geophys. J. Int. 229 (3), 2047–2080.

Louis-Napoléon, A., Vanderhaeghe, O., Gerbault, M., Martin, R., Bonometti, T., 2024. Formation of the Naxos nested domes and crustal differentiationby convection and diapirism. BSGF-Earth Sci. Bull. 192, 21.
Luffi, P., Ducea, M.N., 2022. Chemical mohometry: Assessing crustal thickness of ancient orogens using geochemical and isotopic data. Rev. Geophys. 60 (2), e2021RG000753.
Lund Snee, J.E., Miller, E.L., Grove, M., Hourigan, J.K., Konstantinou, A., 2016. Cenozoic paleogeographic evolution of the Elko Basin and surrounding region, Northeast Nevada. Geosphere 12 (2), 464–500.
Lundstern, J.E., Schwartz, T.M., Mercer, C.M., Colgan, J., Workman, J.B., Morgan, L.E., 2024. Paleogene sedimentary basin development in southern Nevada, USA. Lithosphere 1, 1–34.
Łuszczak, K., Persano, C., Braun, J., Stuart, F.M., 2017. How local crustal thermal properties influence the amount of denudation derived from low-temperature thermochronometry. Geology 45 (9), 779–782.
MacCready, T., Snoke, A.W., Wright, J.E., Howard, K.A., 1997. Mid-crustal flow during Tertiary extension in the Ruby Mountains core complex, Nevada. Geol. Soc. Am. Bull. 109 (12), 1576–1594.
Madsen, J.K., Thorkelson, D.J., Friedman, R.M., Marshall, D.D., 2006. Cenozoic to recent plate configurations in the Pacific Basin: Ridge subduction and slab window magmatism in western North America. Geosphere 2 (1), 11–34.
Mahan, K.H., Guest, B., Wernicke, B., Niemi, N.A., 2009. Low-temperature thermochronologic constraints on the kinematic history and spatial extent of the Eastern California shear zone. Geosphere 5 (6), 483–495.
Manley, C.R., Glazner, A.F., Farmer, G.L., 2000. Timing of volcanism in the Sierra Nevada of California: evidence for Pliocene delamination of the batholithic root? Geology 28 (9), 811–814.
Martinez, C.M., 1999. Tertiary sedimentation in the Sacramento Pass Basin, eastcentral Nevada; implications for the evolution of extensional detachment faults in the Basin and Range. Bull. Am. Assoc. Pet. Geol. 83, 1891.
McCarthy, J., Larkin, S.P., Fuis, G.S., Simpson, R.W., Howard, K.A., 1991. Anatomy of a metamorphic core complex: Seismic refraction/wide-angle reflection profiling in southeastern California and western Arizona. J. Geophys. Res. Solid Earth 96 (B7), 12259–12291.
McFadden, R.R., Mulch, A., Teyssier, C., Heizler, M., 2015. Eocene extension and meteoric fluid flow in the Wildhorse detachment, Pioneer metamorphic core complex, Idaho. Lithosphere 7 (4), 355–366.
McGrew, A., 2018. Geologic map of the Humboldt Peak quadrangle, Elko County, Nevada. In: Nevada Bureau of Mines and Geology Map 186 scale 1:24,000, 23 p.
McGrew, A.J., Casey, M., 1998. Quartzite fabric transition in a Cordilleran metamorphic core complex. In: Snoke, A.W., Tullis, J.A., Todd, V.R. (Eds.), Fault-Related Rocks—A Photographic Atlas. Princeton University Press, Princeton, New Jersey, pp. 484–489. https://doi.org/10.1515/9781400864935.484.
McGrew, A.J., Snee, L.W., 1994. 40Ar/39Ar thermochronologic constraints on the tectonothermal evolution of the northern East Humboldt Range metamorphic core complex, Nevada. Tectonophysics 238 (1–4), 425–450.
McGrew, A.J., Snoke, A.W., 2015. Geologic map of the Welcome quadrangle and an adjacent part of the Wells quadrangle, Elko County, Nevada. In: Nevada Bureau of Mines and Geology Map, p. 184.
McGrew, A.J., Peters, M.T., Wright, J.E., 2000. Thermobarometric constraints on the tectonothermal evolution of the East Humboldt Range metamorphic core complex, Nevada. Geol. Soc. Am. Bull. 112 (1), 45–60.
McQuarrie, N., Chase, C.G., 2000. Raising the Colorado plateau. Geology 28 (1), 91–94.
Michels, Z.D., Kruckenberg, S.C., Davis, J.R., Tikoff, B., 2015. Determining vorticity axes from grain-scale dispersion of crystallographic orientations. Geology 43 (9), 803–806.
Miller, C.F., Bradfish, L.J., 1980. An inner Cordilleran belt of muscovite-bearing plutons. Geology 8 (9), 412–416.
Miller, E.L., Gans, P.B., 1989. Cretaceous crustal structure and metamorphism in the hinterland of the Sevier thrust belt, western US Cordillera. Geology 17 (1), 59–62.
Miller, E.L., Gans, P.B., 1999. Geologic map of the Cove Quadrangle. In: Nevada: Nevada Bureau of Mines and Geology Field Studies Map, p. 22.
Miller, J.M., John, B.E., 1988. Detached strata in a Tertiary low-angle normal fault terrane, southeastern California: a sedimentary record of unroofing, breaching, and continued slip. Geology 16 (7), 645–648.
Miller, J.M., John, B.E., 1999. Sedimentation patterns support seismogenic low-angle normal faulting, southeastern California and western Arizona. Geol. Soc. Am. Bull. 111 (9), 1350–1370.
Miller, E.L., Gans, P.B., Garing, J., 1983. The Snake Range decollement: an exhumed mid-Tertiary ductile-brittle transition. Tectonics 2 (3), 239–263.
Miller, D.M., Hillhouse, W.C., Zartman, R.E., Lanphere, M.A., 1987. Geochronology of intrusive and metamorphic rocks in the Pilot Range, Utah and Nevada, and comparison with regional patterns. Geol. Soc. Am. Bull. 99 (6), 866–879.
Miller, E.L., Dumitru, T.A., Brown, R.W., Gans, P.B., 1999. Rapid Miocene slip on the Snake Range–Deep Creek range fault system, east-central Nevada. Geol. Soc. Am. Bull. 111 (6), 886–905.
Moore, W.B., Webb, A.A.G., 2013. Heat-pipe earth. Nature 501 (7468), 501–505.
Moyen, J.F., 2009. High Sr/Y and La/Yb ratios: the meaning of the "adakitic signature". Lithos 112 (3–4), 556–574.
Naylor, R.S., 1969. Age and origin of the Oliverian domes, Central-Western New Hampshire. Geol. Soc. Am. Bull. 80 (3), 405–428.
Norlander, B.H., Whitney, D.L., Teyssier, C., Vanderhaeghe, O., 2002. Partial melting and decompression of the Thor-Odin dome, Shuswap metamorphic core complex, Canadian Cordillera. Lithos 61 (3–4), 103–125.
O'Neill, J.M., Tysdal, R.G., 2005. Stratigraphic Studies in Southwestern Montana and Adjacent Idaho–lower Tertiary Anaconda Conglomerate and Mesoproterozoic Gunsight Formation (No. 1700). US Geological Survey.
O'Neill, J.M., Lonn, J.D., Lageson, D.R., Kunk, M.J., 2004. Early Tertiary Anaconda metamorphic core complex, southwestern Montana. Can. J. Earth Sci. 41 (1), 63–72.
Paterson, S.R., Fowler, T.K., 1993. Re-examining pluton emplacement processes. J. Struct. Geol. 15, 191–206.
Paterson, S.R., Brudos, T., Fowler, K., Carlson, C., Bishop, K., Vernon, R.H., 1991. Papoose Flat pluton: Forceful expansion or postemplacement deformation? Geology 19 (4), 324–327.
Pease, V., Foster, D., Wooden, J., O'Sullivan, P., Argent, J., Fanning, C., 1999. The Northern Sacramento Mountains, Southwest United States. Part II: Exhumation history and detachment faulting. Geol. Soc. Lond. Spec. Publ. 164 (1), 199–238.
Perkins, M.E., Nash, W.P., Brown, F.H., Fleck, R.J., 1995. Fallout tuffs of Trapper Creek, Idaho—a record of Miocene explosive volcanism in the Snake River Plain volcanic province. Geol. Soc. Am. Bull. 107 (12), 1484–1506.
Peters, L., Ferguson, C.A., Spencer, J.E., Orr, T.R., Dickinson, W.R., 2003. Sixteen 40Ar/39Ar geochronology analyses from southeastern Arizona. Ariz. Geol. Surv. Open File Rep. 03-02, 47 p.
Petford, N., Cruden, A.R., McCaffrey, K.J.W., Vigneresse, J.L., 2000. Granite magma formation, transport and emplacement in the Earth's crust. Nature 408 (6813), 669–673.
Pierce, W.G., 1957. Heart Mountain and south Fork detachment thrusts of Wyoming. AAPG Bull. 41 (4), 591–626.
Pierce, W.G., 1975. Principal features of the Heart Mountain fault and the mechanism problem. In: Geology and Mineral Resources of the Bighorn Basin; 27th Annual Field Conference Guidebook, pp. 139–148.
Pierce, K.L., Covington, H.R., Williams, P.L., McIntyre, D.H., 1983. Geologic Map of the Cotterel Mountains and the Northern Raft River Valley, Cassia County, Idaho (No. 1450).
Platt, J.P., Behr, W.M., Cooper, F.J., 2015. Metamorphic core complexes: Windows into the mechanics and rheology of the crust. J. Geol. Soc. Lond. 172 (1), 9–27.
Price, R.A., 1981. The Cordilleran foreland thrust and fold belt in the southern Canadian Rocky Mountains. Geol. Soc. Lond. Spec. Publ. 9, 427–448.
Prior, M.G., Stockli, D.F., Singleton, J.S., 2016. Miocene slip history of the Eagle Eye detachment fault, Harquahala Mountains metamorphic core complex, west-Central Arizona. Tectonics 35 (8), 1913–1934.
Prior, M.G., Singleton, J.S., Stockli, D.F., 2018. Late-stage slip history of the Buckskin-Rawhide detachment fault and temporal evolution of the Lincoln Ranch supradetachment basin: New constraints from the middle Miocene Sandtrap Conglomerate. GSA Bull. 130 (9–10), 1747–1760.
Profeta, L., Ducea, M.N., Chapman, J.B., Paterson, S.R., Gonzales, S.M.H., Kirsch, M., et al., 2015. Quantifying crustal thickness over time in magmatic arcs. Sci. Rep. 5 (1), 1–7.
Proffett Jr., J.M., 1977. Cenozoic geology of the Yerington district, Nevada, and implications for the nature and origin of Basin and Range faulting. Geol. Soc. Am. Bull. 88 (2), 247–266.
Quilichini, A., Siebenaller, L., Teyssier, C., Vennemann, T.W., 2016. Magmatic and meteoric fluid flow in the Bitterroot extensional detachment shear zone (MT, USA) from ductile to brittle conditions. J. Geodyn. 101, 109–128.
Rabillard, A., Jolivet, L., Arbaret, L., Bessière, E., Laurent, V., Menant, A., et al., 2018. Synextensional granitoids and detachment systems within Cycladic metamorphic core complexes (Aegean Sea, Greece): toward a regional tectonomagmatic model. Tectonics 37 (8), 2328–2362.
Ramberg, H., 1981. The role of gravity in orogenic belts. Geol. Soc. Lond. Spec. Publ. 9 (1), 125–140.
Reiners, P.W., Farley, K.A., Hickes, H.J., 2002. He diffusion and (U–Th)/He thermochronometry of zircon: initial results from fish Canyon Tuff and Gold Butte. Tectonophysics 349 (1–4), 297–308.
Reiners, P.W., Spell, T.L., Nicolescu, S., Zanetti, K.A., 2004. Zircon (U-Th)/He thermochronometry: He diffusion and comparisons with 40Ar/39Ar dating. Geochim. Cosmochim. Acta 68 (8), 1857–1887.
Rey, P., Vanderhaeghe, O., Teyssier, C., 2001. Gravitational collapse of the continental crust: definition, regimes and modes. Tectonophysics 342 (3–4), 435–449.
Rey, P.F., Teyssier, C., Whitney, D.L., 2009a. Extension rates, crustal melting, and core complex dynamics. Geology 37 (5), 391–394.
Rey, P.F., Teyssier, C., Whitney, D.L., 2009b. The role of partial melting and extensional strain rates in the development of metamorphic core complexes. Tectonophysics 477 (3–4), 135–144.
Rey, P.F., Mondy, L., Duclaux, G., Teyssier, C., Whitney, D.L., Bocher, M., Prigent, C., 2017. The origin of contractional structures in extensional gneiss domes. Geology 45 (3), 263–266.
Reynolds, S.J., Lister, G.S., 1990. Folding of mylonitic zones in Cordilleran metamorphic core complexes: evidence from near the mylonitic front. Geology 18 (3), 216–219.
Ribeiro, B.V., Kirkland, C.L., Kelsey, D.E., Reddy, S.M., Hartnady, M.I., Faleiros, F.M., et al., 2023. Time-strain evolution of shear zones from petrographically constrained Rb–Sr muscovite analysis. Earth Planet. Sci. Lett. 602, 117969.
Richard, S.M., Fryxell, J.E., Sutter, J.F., 1990. Tertiary structure and thermal history of the Harquahala and Buckskin Mountains, west Central Arizona: Implications for denudation by a major detachment fault system. J. Geophys. Res. Solid Earth 95 (B12), 19973–19987.
Rothfuss, J.L., Lielke, K., Weislogel, A.L., 2012. Application of Detrital Zircon Provenance in Paleogeographic Reconstruction of an Intermontane Basin System, Paleogene Renova Formation, Southwest Montana.

Royden, L.H., Burchfiel, B.C., King, R.W., Wang, E., Chen, Z., Shen, F., Liu, Y., 1997. Surface deformation and lower crustal flow in eastern Tibet. science 276 (5313), 788–790.
Rubin, A.E., Cooper, K.M., Till, C.B., Kent, A.J., Costa, F., Bose, M., et al., 2017. Rapid cooling and cold storage in a silicic magma reservoir recorded in individual crystals. Science 356 (6343), 1154–1156.
Rudnick, R.L., Fountain, D.M., 1995. Nature and composition of the continental crust: a lower crustal perspective. Rev. Geophys. 33 (3), 267–309.
Ruksznis, A., 2015. Geology and Geochronology of Cenozoic Sedimentary Basins, East-Central Nevada. Doctoral dissertation. Stanford University.
Rusmore, M.E., Bogue, S.W., Woodsworth, G.J., 2013. Paleogeography of the Insular and Intermontane terranes reconsidered: evidence from the southern Coast Mountains batholith, British Columbia. Lithosphere 5 (5), 521–536.
Saltzer, S.D., Hodges, K.V., 1988. The Middle Mountain shear zone, southern Idaho: Kinematic analysis of an early Tertiary high-temperature detachment. Geol. Soc. Am. Bull. 100 (1), 96–103.
Satarugsa, P., Johnson, R.A., 2000. Constraints on crustal composition beneath a metamorphic core complex: results from 3-component wide-angle seismic data along the eastern flank of the Ruby Mountains, Nevada. Tectonophysics 329 (1–4), 223–250.
Say, M.C., Zuza, A.V., 2021. Heterogenous late Miocene extension in the northern Walker Lane (California-Nevada, USA) demonstrates vertically decoupled crustal extension. Geosphere 17 (6), 1762–1785.
Schellart, W.P., Stegman, D.R., Farrington, R.J., Freeman, J., Moresi, L., 2010. Cenozoic tectonics of western North America controlled by evolving width of Farallon slab. Science 329 (5989), 316–319.
Schmandt, B., Humphreys, E., 2011. Seismically imaged relict slab from the 55 Ma Siletzia accretion to the Northwest United States. Geology 39 (2), 175–178.
Schwartz, T.M., Graham, S.A., 2017. Depositional history and provenance of Paleogene strata in the Sage Creek basin, southwestern Montana. Geosphere 13 (4), 1285–1309.
Scoggin, S.H., Reiners, P.W., Shuster, D.L., Davis, G.H., Ward, L.A., Worthington, J.R., Nickerson, P.A., Evenson, N.S., 2021. (U-Th)/He and 4He/3He thermochronology of secondary oxides in faults and fractures: a regional perspective from Southeastern Arizona. Geochem. Geophys. Geosyst. 22 (12), e2021GC009905.
Scott, R.J., Foster, D.A., Lister, G.S., 1998. Tectonic implications of rapid cooling of lower plate rocks from the Buckskin-Rawhide metamorphic core complex, west-Central Arizona. Geol. Soc. Am. Bull. 110 (5), 588–614.
Segee-Wright, G., Barnes, J.D., Lassiter, J.C., Holmes, D.J., Beaudoin, G.M., Chatterjee, R., et al., 2023. Halogen enrichment in the North American lithospheric mantle from the dehydration of the Farallon plate. Geochim. Cosmochim. Acta 348, 187–205.
Sharp, R.P., 1939. The Miocene Humboldt Formation in northeastern Nevada. J. Geol. 47 (2), 133–160.
Sharp, R.P., 1942. Stratigraphy and structure of the southern Ruby Mountains, Nevada. Bull. Geol. Soc. Am. 53 (5), 647–690.
Sibson, R.H., 1977. Fault rocks and fault mechanisms. J. Geol. Soc. Lond. 133 (3), 191–213.
Sihpol, T., Lee, T., Odlum, M., Zuza, A.V., 2024. Reconciling North American metamorphic core complex formation models with coupled microstructural analysis and apatite U-Pb petrochronology in the Chemehuevi Mountains, CA, USA. In: GSA Connects Fall Meeting.
Silverberg, D.S., 1990. The Tectonic Evolution of the Pioneer Metamorphic Core Complex, South-Central Idaho. Doctoral dissertation. Massachusetts Institute of Technology.
Singleton, J.S., Mosher, S., 2012. Mylonitization in the lower plate of the Buckskin-Rawhide detachment fault, west-Central Arizona: Implications for the geometric evolution of metamorphic core complexes. J. Struct. Geol. 39, 180–198.
Singleton, J.S., Stockli, D.F., Gans, P.B., Prior, M.G., 2014. Timing, rate, and magnitude of slip on the Buckskin-Rawhide detachment fault, west Central Arizona. Tectonics 33 (8), 1596–1615.
Singleton, J.S., Seymour, N.M., & Strickland, E.D., 2022. The Buckskin-Rawhide and northern Plomosa Mountains metamorphic core complexes, west-central Arizona, USA, Field Excursions from Las Vegas, Nevada: Guides to the 2022 GSA Cordilleran and Rocky Mountain Joint Section Meeting.
Smith Jr., J.F., 1982. Geologic Map of the Strevell 15-Minute Quadrangle. U.S. Geological Survey Miscellaneous Investigation I-1403, Cassia County, Idaho.
Smith, M.E., Cassel, E.J., Jicha, B.R., Singer, B.S., Canada, A.S., 2017. Hinterland drainage closure and lake formation in response to middle Eocene Farallon slab removal, Nevada, USA. Earth Planet. Sci. Lett. 479, 156–169.
Snelson, S., 1957. The Geology of the Northern Ruby Mountains and the East Humboldt Range, Elko County, Northeastern Nevada (PhD thesis). University of Washington, Seattle, Washington.
Snoke, A.W., McGrew, A.J., Valasek, P.A., Smithson, S.B., 1990. A crustal cross-section for a terrain of superimposed shortening and extension: Ruby Mountains-East Humboldt Range metamorphic core complex, Nevada. In: Exposed Cross-sections of the Continental Crust, pp. 103–135.
Snoke, A.W., 1980. Transition from infrastructure to suprastructure in the northern Ruby Mountains, Nevada. In: Crittenden, M.D., Coney, P.J., Davis, G.H. (Eds.), Cordilleran Metamorphic Core Complexes. Geological Society of America Memoir, 153, pp. 287–333.
Snoke, A.W., Barnes, C.G., Howard, K.A., Romanoski, A., Premo, W.R., Hetherington, C. J., Strike, A.T., Frost, C.D., Copeland, P., Lee, S., 2024. Paleogene mid-crustal intrusions in the Ruby Mountains–East Humboldt Range metamorphic core complex, northeastern Nevada, USA. Geosphere, 20 (2), 577–620.
Sonder, L.J., Jones, C.H., 1999. Western United States extension: how the west was widened. Annu. Rev. Earth Planet. Sci. 27 (1), 417–462.
Spencer, J.E., Constenius, K.N., 2020. Reconnaissance Study of Mylonitic Fabrics in the Bellota Ranch Area, Eastern Santa Catalina Mountains, Arizona.
Spencer, J.E., Reynolds, S.J., 1989. Middle Tertiary tectonics of Arizona and adjacent areas. Geologic evolution of Arizona. Arizona Geol. Soc. Digest 17, 539–574.
Spencer, J.E., Reynolds, S.J., 1991. Tectonics of mid-Tertiary extension along a transect through west Central Arizona. Tectonics 10 (6), 1204–1221.
Spencer, J.E., Lingrey, S.H., Johnson, B.J., Cook, J.P., Richard, S.M., 2011. Geologic map of the Happy Valley 7.5′ Quadrangle, Cochise and Pima Counties, Arizona: Arizona Geological Survey Digital Geologic Map DGM-89 version 1.0, map scale 1:24,000, 7 p. and 1 map plate.
Spencer, J.E., Singleton, J.S., Strickland, E., Reynolds, S.J., Love, D., Foster, D.A., Johnson, R., 2018. Geodynamics of Cenozoic extension along a transect across the Colorado River extensional corridor, southwestern USA. Lithosphere 10 (6), 743–759.
Spencer, J.E., Richard, S.M., Lingrey, S.H., Johnson, B.J., Johnson, R.A., Gehrels, G.E., 2019. Reconstruction of mid-Cenozoic extension in the Rincon Mountains area, southeastern Arizona, USA, and geodynamic implications. Tectonics 38, 2338–2357. https://doi.org/10.1029/2019TC005565.
Spencer, J.E., Richard, S.M., Youberg, A., Ferguson, C.A., Orr, T.R., 2021. Geologic Map of the Chief Butte 7.5′ Quadrangle, Southeastern Pinal County, Arizona: Arizona Geological Survey Digital Geologic Map DGM-22 version 2.0, map scale 1:24,000.
Spencer, J.E., Richard, S.M., Bykerk-Kauffman, A., Constenius, K.N., Valencia, V.A., 2022. Structure, chronology, kinematics, and geodynamics of tectonic extension in the greater Catalina metamorphic core complex, southeastern Arizona, USA. Geosphere 18 (6), 1643–1678.
Stewart, J.H., 1980. Geology of Nevada. In: Nevada Bureau of Mines and Geology Special Publication, 4, p. 136.
Stipp, M., Stuenitz, H., Heilbronner, R., Schmid, S.M., 2002. The eastern Tonale fault zone: a 'natural laboratory' for crystal plastic deformation of quartz over a temperature range from 250 to 700 °C. J. Struct. Geol. 24 (12), 1861–1884.
Stockli, D.F., Brichau, S., Dewane, T.J., Hager, C., Schroeder, J., 2006. Dynamics of largemagnitude extension in the Whipple Mountains metamorphic core complex. Geochim. Cosmochim. Acta 70, A616.
Strickland, A., Miller, E.L., Wooden, J.L., 2011. The timing of Tertiary metamorphism and deformation in the Albion–Raft River–Grouse Creek metamorphic core complex, Utah and Idaho. J. Geol. 119 (2), 185–206.
Strickland, E.D., Singleton, J.S., Haxel, G.B., 2018. Orocopia Schist in the northern Plomosa Mountains, west-Central Arizona: a Laramide subduction complex exhumed in a Miocene metamorphic core complex. Lithosphere 10 (6), 723–742.
Stroup, C.N., Link, P.K., Janecke, S.U., Fanning, C.M., Yaxley, G.M., Beranek, L.P., et al., 2008. Eocene to Oligocene provenance and drainage in extensional basins of Southwest Montana and east-Central Idaho: evidence from detrital zircon populations in the Renova Formation and equivalent strata. In: Ores and Orogenesis: Circum-Pacific Tectonics, Geologic Evolution, and Ore Deposits: Arizona Geological Society Digest, 22, pp. 529–546.
Sundell, K.E., Laskowski, A.K., Kapp, P.A., Ducea, M.N., Chapman, J.B., 2021. Jurassic to Neogene quantitative crustal thickness estimates in southern Tibet. GSA Today 31 (6), 4–10.
Sylvester, A.G., Ortel, G., Nelson, C.A., Christie, J.M., 1978. Papoose flat pluton: a granitic blister in the Inyo Mountains, California. Geol. Soc. Am. Bull. 89 (8), 1205–1219.
Talbot, C.J., Jackson, M.P.A., 1987. Internal kinematics of salt diapirs. AAPG Bull. 71 (9), 1068–1093.
Terrien, J.J., 2012. The Role of Magmatism in the Catalina Metamorphic Core Complex, Arizona: Insights from Integrated Thermochronology, Gravity and Aeromagnetic Data. Doctoral dissertation,. Syracuse University.
Teyssier, C., Whitney, D.L., 2002. Gneiss domes and orogeny. Geology 30 (12), 1139–1142.
Thébaud, N., Rey, P.F., 2013. Archean gravity-driven tectonics on hot and flooded continents: controls on long-lived mineralised hydrothermal systems away from continental margins. Precambrian Res. 229, 93–104.
Thompson, A.B., Connolly, J.A., 1995. Melting of the continental crust: some thermal and petrological constraints on anatexis in continental collision zones and other tectonic settings. J. Geophys. Res. Solid Earth 100 (B8), 15565–15579.
Thoresen, H.E., Cassel, E.J., Smith, M.E., Stockli, D.F., Jicha, B.R., 2024. Stratigraphic and geochronologic investigation of the Muddy Creek Basin: Implications for the Eocene tectonic evolution of southwest Montana, USA. Geol. Soc. Am. Bull., 136 (9–10), 3619–3633.
Thorkelson, D.J., Taylor, R.P., 1989. Cordilleran slab windows. Geology 17 (9), 833–836.
Thorman, C.H., Drewes, H., 1981. Geology of the Rincon wilderness study area, Pima County, Arizona. In: Mineral Resources of the Rincon Wilderness Study Area, Pima County, Arizona: US Geological Survey Bulletin, 1500, pp. 5–37.
Tikoff, B., Fossen, H., 1993. Simultaneous pure and simple shear: the unifying deformation matrix. Tectonophysics 217 (3–4), 267–283.
Tikoff, B., Fossen, H., 1995. The limitations of three-dimensional kinematic vorticity analysis. J. Struct. Geol. 17 (12), 1771–1784.
Tikoff, B., Housen, B.A., Maxson, J.A., Nelson, E.M., Trevino, S., Shipley, T.F., 2023. Hit-and-Run Model for Cretaceous–Paleogene Tectonism along the Western Margin of Laurentia.
Todd, V.R., 1980. Structure and petrology of a Tertiary gneiss complex in northwestern Utah. In: Crittenden, M.D., Coney, P.J., Davis, G.H. (Eds.), Cordilleran Metamorphic Core Complexes. Geological Society of America Memoir, vol. 153, pp. 349–383.

Van Kranendonk, M.J., Hickman, A.H., Smithies, R.H., Nelson, D.R., Pike, G., 2002. Geology and tectonic evolution of the archean North Pilbara terrain, Pilbara Craton, Western Australia. Econ. Geol. 97 (4), 695–732.
Van Kranendonk, M.J., Collins, W.J., Hickman, A., Pawley, M.J., 2004. Critical tests of vertical vs. horizontal tectonic models for the Archaean East Pilbara granite–greenstone terrane, Pilbara craton, western Australia. Precambrian Res. 131 (3–4), 173–211.
Vanderhaeghe, O., 1999. Pervasive melt migration from migmatites to leucogranite in the Shuswap metamorphic core complex, Canada: control of regional deformation. Tectonophysics 312 (1), 35–55.
Vanderhaeghe, O., 2009. Migmatites, granites and orogeny: Flow modes of partially-molten rocks and magmas associated with melt/solid segregation in orogenic belts. Tectonophysics 477 (3–4), 119–134.
Vanderhaeghe, O., 2012. The thermal–mechanical evolution of crustal orogenic belts at convergent plate boundaries: a reappraisal of the orogenic cycle. J. Geodyn. 56, 124–145.
Vanderhaeghe, O., Duchêne, S., 2010. Crustal-scale mass transfer, geotherm and topography at convergent plate boundaries. Terra Nova 22 (5), 315–323.
Vanderhaeghe, O., Teyssier, C., 2001. Partial melting and flow of orogens. Tectonophysics 342 (3–4), 451–472.
Vanderhaeghe, O., Teyssier, C., McDougall, I., Dunlap, W.J., 2003. Cooling and exhumation of the Shuswap Metamorphic Core complex constrained by 40Ar/39Ar thermochronology. Geol. Soc. Am. Bull. 115 (2), 200–216.
Vanderhaeghe, O., Kruckenberg, S.C., Gerbault, M., Martin, L., Duchêne, S., Deloule, E., 2018. Crustal-scale convection and diapiric upwelling of a partially molten orogenic root (Naxos dome, Greece). Tectonophysics 746, 459–469.
Vlaha, D.R., Zuza, A.V., Chen, L., Harlaux, M., 2024. Hot Cordilleran hinterland promoted lower crust mobility and decoupling of Laramide deformation. Nat. Commun. 15 (1), 3750.
Vogl, J.J., Foster, D.A., Fanning, C.M., Kent, K.A., Rodgers, D.W., Diedesch, T., 2012. Timing of extension in the Pioneer metamorphic core complex with implications for the spatial-temporal pattern of Cenozoic extension and exhumation in the northern US Cordillera. Tectonics 31 (1).
Vogl, J.J., Min, K., Carmenate, A., Foster, D.A., Marsellos, A., 2014. Miocene regional hotspot-related uplift, exhumation, and extension north of the Snake River Plain: evidence from apatite (U-Th)/He thermochronology. Lithosphere 6 (2), 108–123.
Wang, T., Zheng, Y., Zhang, J., Zeng, L., Donskaya, T., Guo, L., Li, J., 2011. Pattern and kinematic polarity of late Mesozoic extension in continental NE Asia: Perspectives from metamorphic core complexes. Tectonics 30 (6).
Wells, M.L., 1991. Kinematics and Timing of Mesozoic and Cenozoic Deformations in the Raft River and Black Pine Mountains, Northwestern Utah and Southern Idaho. PhD dissertation. Cornell University, Ithaca, New York.
Wells, M.L., 1997. Alternating contraction and extension in the hinterlands of orogenic belts: an example from the Raft River Mountains, Utah. Geol. Soc. Am. Bull. 109 (1), 107–126.
Wells, M.L., 2001. Rheological control on the initial geometry of the Raft River detachment fault and shear zone, western United States. Tectonics 20 (4), 435–457.
Wells, M.L., 2009. Geologic Map of the Kelton Pass Quadrangle, Box Elder County, Utah, and Cassia County, Idaho, Miscellaneous Publication 09–3, Utah Geol. Surv (ISBN 1-55791-807-4.).
Wells, M.L., Hoiseh, T.D., Hanson, L.M., Wolff, E.D., Struthers, J.R., 1997. Part 3: Large-magnitude crustal thickening and repeated extensional exhumation in the Raft River, Grouse Creek and Albion Mountains. Brigham Young Univ. Geol. Stud. 42, 325–340.
Wells, M.L., Hoisch, T.D., Peters, M.T., Miller, D.M., Wolff, E.D., Hanson, L.M., 1998. The Mahogany Peaks fault, a late Cretaceous-Paleocene (?) normal fault in the hinterland of the Sevier orogen. J. Geol. 106 (5), 623–634.
Wells, M.L., Snee, L.W., Blythe, A.E., 2000. Dating of major normal fault systems using thermochronology: an example from the Raft River detachment, Basin and Range, western United States. J. Geophys. Res. 105 (B7), 16,303–16,327. https://doi.org/10.1029/2000JB900094.
Wells, M.L., Spell, T.L., Hoisch, T.D., Arriola, T., Zanetti, K.A., 2008. Laser-probe 40Ar/39Ar dating of strain fringes: Mid-cretaceous synconvergent orogen-parallel extension in the interior of the Sevier orogen. Tectonics 27 (3).
Wells, M.L., Hoisch, T.D., Cruz-Uribe, A.M., Vervoort, J.D., 2012. Geodynamics of synconvergent extension and tectonic mode switching: Constraints from the Sevier-Laramide orogen. Tectonics 31, TC1002. https://doi.org/10.1029/2011TC002913.
Wernicke, B., 1981. Low-angle normal faults in the Basin and Range Province: nappe tectonics in an extending orogen. Nature 291, 645–648.
Wernicke, B., Axen, G.J., 1988. On the role of isostasy in the evolution of normal fault systems. Geology 16 (9), 848–851.
Wernicke, B., Walker, J.D., Beaufait, M.S., 1985. Structural discordance between Neogene detachments and frontal Sevier thrusts, central Mormon Mountains, southern Nevada. Tectonics 4 (2), 213–246.
Wheeler, J.O., 1966. Eastern tectonic belt of western Cordillera in British Columbia. In: Tectonic History and Mineral Deposits of the Western Cordillera: Canadian Institute of Mining and Metallurgy Special, 8, pp. 27–45.
Whitney, D.L., Teyssier, C., Vanderhaeghe, 2004. Gneiss domes and crustal flow. In: Gneiss Domes in Orogeny: Geological Society of America Special Paper 380.
Whitney, D.L., Teyssier, C., Rey, P., Buck, W.R., 2013. Continental and oceanic core complexes. Bulletin 125 (3–4), 273–298.
Williams, P.L., Pierce, K.L., McIntyre, D.H., Schmidt, P.W., 1974. Preliminary Geologic Map of the Southern Raft River area, Cassia County, Idaho. U.S. Geological Survey Open-File Report 74–1126, scale 1:24,000.
Williams, P.L., Covington, H.R., Pierce, K.L., 1982. Cenozoic stratigraphy and tectonic evolution of the Raft River Basin, Idaho; Cenozoic geology of Idaho. Idaho Bureau Mines Geol. Bull. 26, 491–504.
Wolf, R.A., Farley, K.A., Silver, L.T., 1996. Helium diffusion and low-temperature thermochronometry of apatite. Geochim. Cosmochim. Acta 60 (21), 4231–4240.
Wolfe, M.R., Stockli, D.F., 2010. Zircon (U–Th)/He thermochronometry in the KTB drill hole, Germany, and its implications for bulk He diffusion kinetics in zircon. Earth Planet. Sci. Lett. 295 (1–2), 69–82.
Wong, M.S., Singleton, J.S., Seymour, N.M., Gans, P.B., Wrobel, A.J., 2023. Late Cretaceous-early Paleogene Extensional Ancestry of the Harcuvar and Buckskin-Rawhide Metamorphic Core Complexes, Western Arizona. Tectonics 42 (2), e2022TC007656.
Wright, J.E., Snoke, A.W., 1993. Tertiary magmatism and mylonitization in the Ruby-East Humboldt metamorphic core complex, northeastern Nevada: U-Pb geochronology and Sr, Nd, and Pb isotope geochemistry. Geol. Soc. Am. Bull. 105 (7), 935–952.
Wright, J.E., Anderson, J.L., Davis, G.A., 1986. Timing of plutonism, mylonitization, and decompression in a metamorphic core complex. Geol. Soc. Am. Abstr. Programs 18, 201 (Whipple Mountains, Calif).
Wrobel, A.J., Gans, P.B., Womer, J.B., 2021. Late cretaceous Crustal Shortening in the Northern Snake Range Metamorphic Core complex: Constraints on the Structural Geometry and Magnitude of Pre-Extensional Footwall Burial. Tectonics 40 (8), e2020TC006460.
Wu, F.Y., Yang, J.H., Xu, Y.G., Wilde, S.A., Walker, R.J., 2019. Destruction of the North China craton in the Mesozoic. Annu. Rev. Earth Planet. Sci. 47, 173–195.
Wu, J.T.J., Wu, J., Okamoto, K., 2022. Intra-oceanic arc accretion along Northeast Asia during early cretaceous provides a plate tectonic context for North China craton destruction. Earth Sci. Rev. 226, 103952.
Wust, S.L., 1986. Regional correlation of extension directions in Cordilleran metamorphic core complexes. Geology 14 (10), 828–830.
Xu, X., Zuza, A.V., Chen, L., Zhu, W., Yin, A., Fu, X., et al., 2021. Late cretaceous to early Cenozoic extension in the lower Yangtze region (East China) driven by Izanagi-Pacific plate subduction. Earth Sci. Rev. 221, 103790.
Yang, L.Q., Deng, J., Wang, Z.L., Zhang, L., Goldfarb, R.J., Yuan, W.M., et al., 2016. Thermochronologic constraints on evolution of the Linglong Metamorphic Core complex and implications for gold mineralization: a case study from the Xiadian gold deposit, Jiaodong Peninsula, eastern China. Ore Geol. Rev. 72, 165–178.
Yin, A., 2004. Gneiss domes and gneiss dome systems. In: Gneiss Domes in Orogeny: Geological Society of America Special Paper, 380, pp. 1–14.
Yin, A., Dunn, J.F., 1992. Structural and stratigraphic development of the Whipple-Chemehuevi detachment fault system, southeastern California: Implications for the geometrical evolution of domal and basinal low-angle normal faults. Geol. Soc. Am. Bull. 104 (6), 659–674.
Yonkee, W.A., Weil, A.B., 2015. Tectonic evolution of the Sevier and Laramide belts within the North American Cordillera orogenic system. Earth Sci. Rev. 150, 531–593.
Zaun, P.E., Wagner, G.A., 1985. Fission-track stability in zircons under geological conditions. Nucl. Tracks Radiat. Meas. (1982) 10 (3), 303–307.
Zhang, Y., Dong, S., Shi, W., 2023. Hot thermal upwelling-extensional structure: Recognition of "metamorphic core complexes" in North China. Chin. Sci. Bull. https://doi.org/10.1360/TB-2023-0402.
Zhao, N., Cong, F., 2014. Microstructural characteristics and deformation mechanism of the Shear Zone of Fangshan Pluton, North China. In: AGU Fall Meeting Abstracts, vol. 2014 pp. T31A-4558.
Zuza, A., Cao, W., 2023. Metamorphic Core complex Dichotomy in the North American Cordillera Explained by Buoyant Upwelling in Variably Thick Crust. GSA Today, 33 (3–4), 4–11.
Zuza, A.V., Dee, S., 2023. Decoupled Oligocene mylonitic shearing and Miocene detachment faulting in the East Humboldt Range metamorphic core complex, northeast Nevada, USA. Geosphere 19 (5), 1318–1347.
Zuza, A.V., Cheng, X., Yin, A., 2016. Testing models of Tibetan Plateau formation with Cenozoic shortening estimates across the Qilian Shan–Nan Shan thrust belt. Geosphere 12 (2), 501–532.
Zuza, A.V., Cao, W., Hinz, N.H., DesOrmeau, J.W., Odlum, M.L., Stockli, D.F., 2019. Footwall rotation in a regional detachment fault system: evidence for horizontal-axis rotational flow in the Miocene Searchlight pluton, NV. Tectonics 38 (7), 2506–2539.
Zuza, A.V., Thorman, C.H., Henry, C.D., Levy, D.A., Dee, S., Long, S.P., et al., 2020. Pulsed Mesozoic deformation in the Cordilleran hinterland and evolution of the Nevadaplano: Insights from the Pequop Mountains, NE Nevada. Lithosphere 2020 (1).
Zuza, A.V., Henry, C.D., Dee, S., Thorman, C.H., Heizler, M.T., 2021. Jurassic–Cenozoic tectonics of the Pequop Mountains, NE Nevada, in the North American Cordillera hinterland. Geosphere 17 (6), 2078–2122.
Zuza, A.V., Cao, W., Rodriguez-Arriaga, A., DesOrmeau, J.W., Odlum, M.L., 2022a. Strain localization at brittle-ductile transition depths during Miocene magmatism and exhumation in the southern Basin and Range. J. Struct. Geol. 163, 104709.
Zuza, A.V., Levy, D.A., Dee, S., DesOrmeau, J.W., Cheng, F., Li, X., 2022b. Structural Architecture and Attenuation of the Ductile lower Plate of the Ruby Mountain-East Humboldt Range Metamorphic Core complex, Northeast Nevada. Tectonics 41 (8), e2021TC007162.
Zuza, A.V., Levy, D.A., Mulligan, S.R., 2022c. Geologic field evidence for non-lithostatic overpressure recorded in the North American Cordillera hinterland, Northeast Nevada. Geosci. Front. 13 (2), 101099.
Zuza, A.V., Cao, W., Levy, D.A., DesOrmeau, J.W., Odlum, M.L., Siciliano, A.A., 2024. Kinematic vorticity of shear zones that accommodate vertical crustal advection:

Implications for metamorphic core complexes and pluton emplacement. Earth Planet. Sci. Lett. 646, 118964.
Howard, K.A.,1980. In: Crittenden, M.D., Coney, P.J., Davis, G.H. (Eds.), Metamorphic Core Complexes, 153. Geological Society of America Memoir, pp. 335–347.
Fletcher, R.C., Hallet, B., 2004. Initiation of gneiss domes by necking, density instability, and erosion. In: Whitney, D.L., Teyssier, C., Siddoway, C.S. (Eds.), Gneiss Domes in Orogeny, Spec. Pap. Geol. Soc. Am., pp. 79–96.